

Halide sodalites: macroscopic and microscopic properties, and deviations from the average structure

Dissertation

Zur Erlangung des Doktorgrades in den Naturwissenschaften

Dr. rer. nat.

Fachbereich 02 (Biologie/Chemie)

Universität Bremen

Vorgelegt von
M. Sc. Marius Wolpmann

Bremen 2022

Diese Arbeit wurde an der Universität Bremen in der Arbeitsgruppe "Chemische Kristallographie fester Stoffe" von Herrn Prof. Dr. Thorsten M. Gesing im Zeitraum von Oktober 2018 bis September 2022 angefertigt.

Vorgelegt am 15.09.2022

Datum des Kolloquiums: 09.11.2022

Erstgutachter: Prof. Dr. J.-Ch. Buhl, Institut für Mineralogie, Universität Hannover (1994-2021)

Zweitgutachter: Prof. Dr. R. X. Fischer, Fachbereich 05 Geowissenschaften, Kristallographie, Universität Bremen (1995-2022)

Danksagung

Ich möchte mich bei Prof. Dr. Thorsten M. Gesing für die Möglichkeit, diese Arbeit in seine Arbeitsgruppe „Chemische Kristallographie fester Stoffe“ anzufertigen, und die langjährige Unterstützung seit meiner Bachelorarbeit bedanken. Prof. Dr. Josef-Christian Buhl und Prof. Dr. Reinhard X. Fischer gilt mein Dank für die Übernahme der Gutachten zu dieser Dissertation. Ganz besonders möchte ich mich auch bei Dr. Lars Robben bedanken, da er mir immer mit wissenschaftlichem Rat zur Seite stand und durch produktive Diskussionen zur Entstehung dieser Arbeit beigetragen hat. Außerdem gebührt ihm Dank für die Durchführung der Kraftfeld Rechnungen.

Dr. Martin Etter danke ich sehr für die Messung der temperaturabhängigen *total scattering*-Daten sowie Andrea Kirsch, Mathias Gogolin und Niels Lefeld für die Messung der *total scattering*-Daten bei Umgebungstemperatur. Bei Wilke Dononelli und Filippo Balzaretto bedanke ich mich für die Durchführung der DFT- und AIMD-Rechnungen.

Ich danke auch allen aktuellen und früheren Mitgliedern der Arbeitsgruppe „Chemische Kristallographie fester Stoffe“ für die angenehme Atmosphäre während und nach der Arbeit.

Mein herzlicher Dank gilt meiner Familie und Freunden, insbesondere meiner Partnerin Julia Berten, für die bedingungslose Unterstützung, ohne welche ich diese Arbeit nicht hätte anfertigen können.

Acknowledgements

The CKfS group and I gratefully acknowledge the Deutsche Forschungsgemeinschaft (DFG) for financial support through RO5995/2-1 and within the large instrument program (INST 144/335-1 FUGG Raman spectrometer, INST 144/435-1 FUGG TD X-ray powder diffractometer and INST 144/458-1 FUGG Std. X-ray powder diffractometer). I also acknowledge DESY (Hamburg, Germany), a member of the Helmholtz Association HGF, for the provision of experimental facilities. Parts of this research were carried out at PETRA III beamlines P02.1 and P21.1. I would like to thank Dr. Soham Banerjee for assistance in using beamline P21.1. Beamtime was allocated for proposals I-20200180 and I-20200535.

Versicherung an Eides Statt

Ich, Marius Wolpmann,

versichere an Eides Statt durch meine Unterschrift, dass ich die vorstehende Arbeit selbständig und ohne fremde Hilfe angefertigt und alle Stellen, die ich wörtlich dem Sinne nach aus Veröffentlichungen entnommen habe, als solche kenntlich gemacht habe, mich auch keiner anderen als der angegebenen Literatur oder sonstiger Hilfsmittel bedient habe.

Ich versichere an Eides Statt, dass ich die vorgenannten Angaben nach bestem Wissen und Gewissen gemacht habe und dass die Angaben der Wahrheit entsprechen und ich nichts verschwiegen habe.

Die Strafbarkeit einer falschen eidesstattlichen Versicherung ist mir bekannt, namentlich die Strafanndrohung gemäß § 156 StGB bis zu drei Jahren Freiheitsstrafe oder Geldstrafe bei vorsätzlicher Begehung der Tat bzw. gemäß § 161 Abs. 1 StGB bis zu einem Jahr Freiheitsstrafe oder Geldstrafe bei fahrlässiger Begehung.

Ort, Datum

Unterschrift

Abstract

Sodalites of the general formula $[\text{Na}_8\text{X}_2][\text{T}^1\text{T}^2\text{O}_4]_6$ with $\text{X} = \text{Cl}^-, \text{Br}^-, \text{I}^-$ have been synthesized for Al-Si, Ga-Si, Al-Ge and Ga-Ge as $\text{T}^1\text{-T}^2$ frameworks and were examined by various methods to clarify the interactions of the atoms, especially of the Na^+ and X^- ions within the sodalite cages, and the relation of these interactions to the stability and thermal behavior of the compounds. The sodalites average structure between 18 K and its decomposition has been refined using temperature-dependent X-ray diffraction experiments. No other phase transitions besides the known $P\bar{4}3n \leftrightarrow Pm\bar{3}n$ transition of $[\text{Na}_8\text{Br}_2][\text{AlSiO}_4]_6$ and $[\text{Na}_8\text{I}_2][\text{AlSiO}_4]_6$ to the fully expanded framework structure were found. The phonon structure was approximated by modelling the volume thermal expansion with Debye and Einstein contributions to the internal energy. No direct relation between the respective Debye and Einstein temperatures, decomposition temperatures from thermal analyses and the phonon densities of states (PDOS) from force-field calculations was found. However, applying a modified form of the Lindemann criterion, the twelve compounds could be divided into three groups, indicating a different interplay between phonon systems and temperature-dependent average structures within these groups.

Atomic pair distribution functions (PDF) derived from synchrotron total scattering experiments allowed the refinement of anisotropic displacement parameters (ADP) for the oxygen and sodium atoms where three distinct forms of the Na ADPs for different compounds became apparent. *Ab-initio* molecular dynamics calculations produced significantly smaller displacement factors, implying the influence of structural differences to the ADPs from PDF calculations. The PDFs of compounds with non-spherical ADPs for sodium could be modelled with structures containing one or two partly occupied Na positions, **24i** and **8e**, respectively, giving a total of three models for the local structure of the twelve sodalites. For the three gallogermanate compounds, which each belong to a different structural group at ambient temperature, the models could be refined between 100 K and 300 K using PDFs from temperature-dependent total scattering experiments. $[\text{Na}_8\text{Br}_2][\text{GaGeO}_4]_6$ sodalite seems to make a transition to a different local Na position close to 300 K. A correlation between these local structures and the three-dimensional representation of the hypothetical bond valence sum (BVS) of sodium in the average structures at ambient temperature was found. The three groups of sodalites with a differently modelled local structure have an overlap with the ordering of the compounds into the three Lindemann groups, but they are not identical. A reason could be that

more halide sodalites undergo phase transitions between different local structures, which are not described yet.

Zusammenfassung

Sodalithe der Zusammensetzung $[\text{Na}_8\text{X}_2][\text{T}^1\text{T}^2\text{O}_4]_6$ mit $\text{X} = \text{Cl}^-, \text{Br}^-, \text{I}^-$ wurden für $\text{T}^1\text{-T}^2$ als Al-Si, Ga-Si, Al-Ge und Ga-Ge Gerüste synthetisiert und mit verschiedenen Methoden untersucht. Das Ziel war, die Wechselwirkungen der Atome, insbesondere der Ionen Na^+ und X^- in den Sodalithkäfigen, sowie die Zusammenhänge zwischen diesen Wechselwirkungen, der Stabilität und dem thermischen Verhalten der Verbindungen aufzuklären. Die mittlere Struktur wurde durch Rietveld-Verfeinerungen gegen Daten aus Röntgenbeugungsexperimenten von 18 K bis zur Zersetzung bestimmt. Dabei wurden keine anderen als die bekannten $P\bar{4}3n \leftrightarrow Pm\bar{3}n$ Phasenumwandlungen von $[\text{Na}_8\text{Br}_2][\text{AlSiO}_4]_6$ and $[\text{Na}_8\text{I}_2][\text{AlSiO}_4]_6$ zu ihrer voll expandierten Gerüststruktur beobachtet. Anhand der Modellierung der thermischen Expansion der mittleren Struktur der Proben konnten die phononischen Eigenschaften durch Debye und Einsteintemperaturen beschrieben werden. Zwischen diesen und der Phononenzustandsdichte aus Kraftfeld-Rechnungen sowie den Zersetzungstemperaturen aus thermogravimetrischen Analysen konnte kein direkter Zusammenhang gefunden werden. Durch Anwendung einer modifizierten Form des Lindemann-Kriteriums war es jedoch möglich, die zwölf Proben in drei Gruppen mit unterschiedlicher Wechselwirkung zwischen ihrem Phononensystem und der temperaturabhängigen mittleren Struktur einzuteilen, entgegen der Erwartung einer einzigen Gruppe für Verbindungen des gleichen Strukturtyps.

Die Strukturen wurden weiterhin durch Auswertung der atomaren Paarverteilungsfunktionen (PDF) aus „total scattering“-Experimenten untersucht, wobei Unterschiede in Gestalt von drei verschiedenen Formen des anisotropen Auslenkungsparameters (ADP) der Natriumatome auffielen. Wesentlich kleinere Auslenkungsparameter wurden über *ab-initio* Molekulardynamikrechnungen ermittelt, was auf einen Einfluss struktureller Abweichungen in den ADPs der PDF-Rechnungen hinweist. Für die zwei Gruppen nicht-sphärischer Na ADPs wurden Modelle mit ein oder zwei teilbesetzten Natriumlagen erstellt (**24i** bzw. **8e**) und konnten stabil verfeinert werden. Über temperaturabhängige „total scattering“-Experimente der gallogermanatischen Sodalithe (welche bei Umgebungsbedingungen jeweils verschiedenen Gruppen angehören) konnten diese drei Modelle lokaler Abweichungen auch zwischen 100 K und 300 K verfeinert werden. Dabei scheint $[\text{Na}_8\text{Br}_2][\text{GaGeO}_4]_6$ sehr nah an 300 K einen Phasenübergang zu einer anderen lokalen Na-Verteilung zu durchlaufen. Darstellungen der hypothetischen Bindungswertsumme von Natrium auf einem dreidimensionalen Raster

innerhalb der Strukturen bei Umgebungsbedingungen korrelieren mit den lokalen Abweichungen. Trotz einiger Überschneidungen zwischen den Verbindungen der drei Lindemann-Gruppen und den lokalen Abweichungen des Natriumatoms stimmen diese nicht überein. Es wird vermutet, dass dies darin begründet ist, dass noch weitere Halogenid-Sodalithe derartige Phasenübergänge der lokalen Struktur zeigen, welche noch nicht beschrieben wurden.

Contributions to publications

Some research presented in this thesis was earlier compiled in form of two manuscripts and submitted to *Zeitschrift für Kristallographie* for publication prior to its writing. At the time this thesis was handed in at the University of Bremen, the first article was already published ([1]: M. Wolpmann, L. Robben, T.M. Gesing, Halide-sodalites: thermal expansion, decomposition and the Lindemann criterion, *Z. Kristallogr. - Cryst. Mater.* 237 (2022) 39-50. Doi:10.1515/zkri-2022-0004). The second one (M. Wolpmann, M. Etter, A. Kirsch, F. Balzaretto, W. Dononelli, L. Robben, T.M. Gesing, Halide-sodalites: thermal behavior at low temperatures and local deviations from the average structure, submitted to *Z. Kristallogr. – Cryst. Mater.*) is currently under review. Parts of the manuscripts were rearranged or rewritten, and pictures replotted to aid the reading flow in the monographic form.

All parts of the articles which were written by the respective co-authors of the manuscripts and experiments which were carried out by them are stated in the following:

- The chapter “*Ab-initio* molecular dynamics calculations” in the experimental details was written by Wilke Dononelli. The respective DFT and AIMD calculations were carried out by Filippo Balzaretto and Wilke Dononelli.
- The chapter “Force-field calculations” in the experimental details was written by Lars Robben. The respective calculations were carried out by Lars Robben.
- The total scattering experiments at beamline P21.1 at PETRA III were carried out by Andrea Kirsch.
- The temperature-dependent total scattering experiments at beamline P02.1 at PETRA III were carried out by Martin Etter.

Declaration on the contribution of the candidate to a multi-author article/manuscript included in the submitted doctoral thesis

Article 1 (Doi:10.1515/zkri-2022-0004):

Contribution of the candidate in % of the total workload (up to 100 % for each of the following categories):

Experimental concept and design:	ca. 90 %
Experimental work and/or acquisition of (experimental) data:	ca. 95 %
Data analysis and interpretation:	ca. 90 %
Preparation of Figures and Tables:	ca. 100 %
Drafting of the manuscript:	ca. 90 %

Article 2 (Halide-sodalites: thermal behavior at low temperatures and local deviations from the average structure, under review):

Contribution of the candidate in % of the total workload (up to 100% for each of the following categories):

Experimental concept and design:	ca. 80 %
Experimental work and/or acquisition of (experimental) data:	ca. 60 %
Data analysis and interpretation:	ca. 80 %
Preparation of Figures and Tables:	ca. 95 %
Drafting of the manuscript:	ca. 95 %

Table of contents

Danksagung	iii
Acknowledgements	iii
Abstract	v
Zusammenfassung	vi
Contributions to publications	viii
Table of contents	x
List of abbreviations	xii
1. Introduction	1
1.1 Sodalites	1
1.2 The Debye-Einstein-anharmonicity model and thermal expansion coefficient	7
1.3 X-ray diffraction: Bragg scattering and total scattering	8
1.4 The bond valence model	9
2. Experimental details	10
2.1 Syntheses	10
2.2 Spectroscopy	11
2.2.1 Raman spectroscopy	11
2.2.2 Infrared (IR) spectroscopy	11
2.3 Thermal analysis	11
2.4 Powder X-ray diffraction (PXRD)	12
2.4.1 Ambient temperature PXRD	12
2.4.2 Temperature-dependent PXRD	12
2.4.3. Rietveld refinements	12
2.5 Total scattering experiments at DESY	13
2.6 3D-BVS	13
2.7 <i>Ab-initio</i> molecular dynamics calculations	14
2.8 Force-field calculations	14

3 Results and discussion.....	15
3.1 Ambient average structure	15
3.2 Spectroscopy	15
3.2.1 Raman spectroscopy.....	15
3.2.2. IR spectroscopy	19
3.3 Decomposition and water loss (TGA/DSC).....	20
3.4 Thermal behavior of the average sodalite structure	23
3.5 Thermal expansion	28
3.6 Force-field calculations	31
3.7 Discussion: The Lindemann criterion	33
3.8 Ambient temperature total scattering, <i>ab-initio</i> MD calculations and 3D-BVS	36
3.9 Temperature-dependent total scattering.....	45
3.10 Discussion: Deviations from the average structure.....	46
4. Conclusion and outlook.....	48
5. References	51
List of figures	xiii
List of tables	xvi
Appendix	xvii
Sodalite structures at ambient conditions.....	xvii

List of abbreviations

ADP	anisotropic displacement parameter
AIMD	<i>ab-initio</i> molecular dynamics
BVS	bond valence sum
DEA	Debye-Einstein-anharmonicity
DESY	<i>Deutsches Elektronen-Synchrotron</i>
DFT	density functional theory
DLS	<i>Distance Least Squares</i> (computer model)
DSC	differential scanning calorimetry
DTG	derivative thermogravimetry
FTIR	Fourier-transform infrared
HT	high-temperature (usually above 300 K)
IR	infrared
LT	low-temperature (usually below 300 K)
mpc	molecules per cage
PAW	projector-augmented wave
PDF	atomic pair distribution function
PDOS	phonon density of states
PTFE	polytetrafluoroethylene
PXRD	powder X-ray diffraction
TEC	thermal expansion coefficient
TGA	thermogravimetric analysis
TOF	time of flight
TSR	tetrahedra six-ring
XRD	X-ray diffraction

1. Introduction

1.1 Sodalites

Sodalites are the simplest porous zeolitic framework materials [2, 3] regarding their topological information content and complexity. They are named after the mineral sodalite $[\text{Na}_8\text{Cl}_2][\text{AlSiO}_4]_6$, which was first described in 1811 by Thomson [4]. The basic sodalite structure was solved by Jaeger [5] on ultramarines and confirmed for the chloride-sodalite mineral by Pauling [6]. The framework consists of alternating, corner sharing AlO_4^- and SiO_4^- tetrahedra forming the so-called *toc*-cages, classically named as β -cages or *sod*-cages. These β -cages are connected in the direction of the unit-cell axes by 4-ring windows and along the space diagonal by 6-ring windows. The net 6-fold negative framework-charge is compensated by six incorporated Na^+ cations and two additional Na^+ and Cl^- ions each are as well located inside the two cages (Figure 2, a and b) per unit cell. The cage-centered chloride ion is coordinated by sodium cations in an ideal tetrahedron (Figure 1, a). The sodium cations are in front of the 6-ring windows, where they are coordinated by three closer oxygen atoms (O1 in the following) and three more distant ones (O2 in the following) (Figure 1, b). A variety of sodalite compounds of different compositions is synthetically accessible [7-29]. Most of them crystallize in the space group $P\bar{4}3n$ (Nr. 218) [30, 31], as do all the sodalites which are examined here.

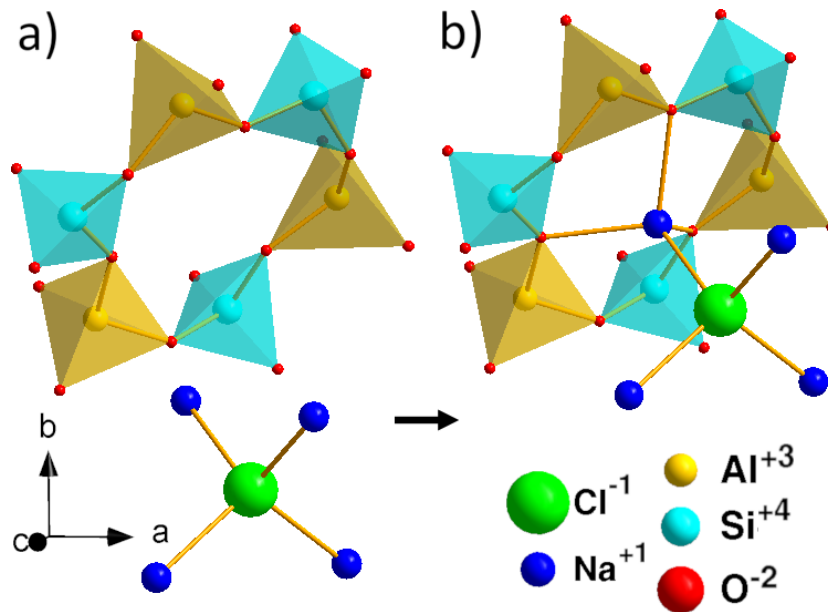


Figure 1: (a) Tetrahedra (T) six-ring (TSR) of AlO_4^- (yellow) and SiO_4^- tetrahedra (cyan) and tetrahedral coordination of the chloride anion (green) to sodium cations (dark blue). (b) Coordination of the sodium atom to one chloride and three nearer oxygen (red) atoms (Na-O1) of the TSR.

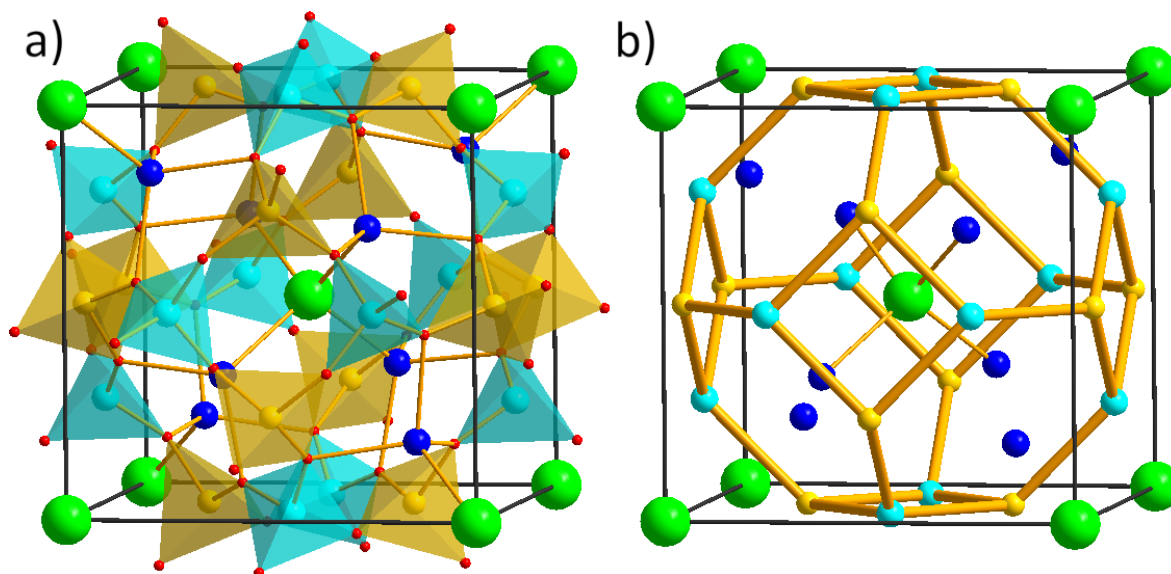


Figure 2: (a) Unit cell of $[\text{Na}_8\text{Cl}_2][\text{AlSiO}_4]_6$ and (b) a T-T atoms linked framework representation of a β -cage. See Figure 1 for the explanation of the colors.

The sodalite cage adapts to the size of different cage-fillings by a cooperative tilting mechanism of the rigid TO_4 -tetrahedra, each rotating about a direction parallel to the cell edge [25]. Upon heating, the sodalite expands through this tilting mechanism, and contracts through it upon cooling. The behavior of sodalites above ambient temperature has been investigated since 1968 [32] and was examined for multiple chemical compositions [9, 12, 13, 16, 21, 33, 34]. Taylor compared the expansion behavior of the sodalite mineral to different nosean and haüyn phases, which possess the same aluminosilicate framework [32] and discussed it later with respect to other framework silicates [35]. He found a fast and increasing expansion rate for all of them due to the tilting of the partially collapsed framework [32]. In contrast to the sodalite, the examined nosean and haüyn samples reach a point above 700 K where the expansion becomes linear, with the exact temperature depending on the ratio of potassium to sodium of the incorporated cations. In a later study of synthetic aluminosilicate sodalites, among them many phases containing different mixed cations, Henderson and Taylor [33] reported on such a discontinuity for iodide sodalite only. However, Hassan and Grundy [36] suggested a discontinuity also for bromide sodalite. Henderson and Taylor [34] compared the thermal behavior of the sodalites cell-edges by mean-expansion coefficients and polynomial fits and noted, that the quadratic fits did not completely describe the true shape of the expansion curves and that structure determinations at high temperatures are necessary. Based on structural evaluations using the *Distance Least Squares* (DLS) computer model [37], Dempsey and Taylor [38] concluded that the driving force of the untilting of the sodalite structure upon heating lies in the framework, while bonds between the cage anions and cations would restrain it, as they are subjected to exceptionally high expansion. They also estimated the Na-I force constant in

[Na₈I₂][AlSiO₄]₆ (AlSiI) sodalite to be one third of that of the Na–O bond. Experimental structural information became more available with technical advances. McMullan et al. [39] examined natural sodalite [Na₈Cl₂][AlSiO₄]₆ using neutron single-crystal diffraction at high temperatures and found significant contributions of anharmonicity to the displacement parameters of Na⁺ and Cl⁻ already at ambient temperatures, which increase with rising temperatures. Compared to a harmonic Gaussian distribution, the probability density of the chloride is elevated in the directions of the four 6-ring windows (along [111]) which are not blocked by Na⁺ in the same cage. The probability density of sodium is also elevated by a tetrahedral shape in direction of the nearest 6-ring window and approximately along three vectors [110], [101] and [011]. This was interpreted as indicating diffusion paths which enable jumping of both ions to vacant sites in neighboring cages and the rotational reorienting of the Na⁺ ions from (xxx) to the enantiomorphic configuration occupying the formerly vacant ($\bar{x}\bar{x}\bar{x}$) site. Anharmonic parameters for oxygen only became significant at 900 K and above. McMullan et al. concluded from the obtained displacement parameters, that the increasing amplitudes of coupled translational motion of the sodium ions and librational motion of the framework tetrahedra are the cause of thermal expansion. Hassan and Grundy [36] constructed a computer program in 1984 for the calculation and prediction of sodalite structures of different compositions on the assumption, that the Na atom reaches the center of the 6-ring at the expansion discontinuities and the Na–O bond length does not significantly change from ambient conditions to the temperature at which the Na coordinate is ¼ (approximately 1000 K). They concluded that the expansion is driven by the expansion of the weak Na-X bond, which forces the framework to follow. Hassan et al. [40] obtained high-temperature structures of sodalite refined from synchrotron data, where an increase of the Na–O bond by 9.3(2) pm from 235.7(1) pm at 301 K to 1255 K was observed. Sodalite compounds with framework atoms different than aluminum and silicon were also studied by X-ray diffraction and subsequent Rietveld-refinements. Gesing [16] compared the thermal expansion of three gallosilicate halide sodalites (X = Cl, Br, I) and observed two temperature ranges of approximately linear volume increase with an unclear behavior in between (770 K to 870 K). This was found to be caused by the disordering of tetrahedral distortion, which relaxed upon heating. A bend in the expansion curve of the [Na₈Cl₂][GaSiO₄]₆ (GaSiCl) sodalite at 500 K was explained as the mobilization-onset of the sodium atoms passing the 6-ring windows at higher temperatures.

Multiple low-temperature investigations of sodalites have been conducted for silica sodalites with different organic cage fillings as well as aluminate sodalites containing tetragonal molecules. Phase transitions to space groups of lower symmetry (e.g., $R\bar{3}, P2_1/m$ and not

clarified tetragonal and monoclinic space groups) were found below and above ambient temperature [26, 27, 41-45]. For sodalites with frameworks built from two tetragonally coordinated atoms, low-temperature studies have been mostly focussed on different hydro and hydroxy sodalites, where the orientation and dynamic motion of the molecules in the cages was of special interest [12, 46-52]. For $[\text{Na}_8(\text{OH})_2(\text{H}_2\text{O})_2][\text{AlSiO}_4]_6$, a phase transition at 152 K [50] from $P\bar{4}3n$ to the orthorhombic space group $P222$ (as given by [50] from [53], which was not available to the author) was reported, which probably occurs at 166 K [46] in the analogous alumogermanate sodalite. Compared to these sodalites, halide sodalites contain only one spherical ion in the cage center. They cannot lock into a single orientation which could lead to phase transitions due to the formation of probable long-range order. This may explain the lack of low-temperature studies on them. However, some noteworthy findings have been published: Schliesser et al. [54] studied the heat capacities of various sodalite samples including Al-Si chloride and iodide sodalite below 300 K. They found phase transition indicating peaks for both compounds between 190 K and 300 K. Robben et al. [29] investigated $[\text{Na}_8\text{I}_2][\text{AlSiO}_4]_6$ sodalite using neutron TOF experiments and found that the iodine is located on a tetrahedral space inverse to the tetrahedron formed by the Na atoms, with a homogeneous distribution in the center. Below 20 K the iodine breaks symmetry by preferring the orientation along one axis when its kinetic energy falls below that of the surrounding anharmonic potential. Between 200 K and 160 K a freezing process of the framework could be observed. Both these structural effects were accompanied by anomalies in the volumetric thermal expansion coefficient (TEC). Only in recent years, authors started to frequently use the TEC, which is very sensitive to changes in the expansion of the unit cell [8, 12] and used advanced physical models like the DEA model [55-68] to describe the thermal behavior of sodalites [29]. Most of the studies mentioned above only used polynomial or linear equations to describe and compare the expansion behavior of sodalites.

The degree of collapse through the tilting mechanism, which defines the expansion of the sodalite framework and greatly influences the size of the unit-cell [25], can be characterized by the average tilt angle φ [25, 69]. It is readily calculated from the structural parameters using equation (1):

$$\varphi = (\varphi_{\text{Si}} + \varphi_{\text{Al}})/2 = \left(\tan^{-1} \frac{\frac{1}{2}z}{x} + \tan^{-1} \frac{\frac{1}{2}z}{y} \right) / 2 \quad (1)$$

where φ_{Si} is the tilt angle of the SiO_4 tetrahedra, φ_{Al} is the tilt angle of the AlO_4 tetrahedra (see Figure 3, left) and x , y and z are the respective coordinates of the oxygen atom. For the fully

expanded framework φ becomes 0° . Structurally, the tilt mechanism manifests itself in the z -coordinate of the framework oxygen atom which shifts from ~ 0.4 in halide sodalites to exactly 0.5 for the fully expanded system, thus undergoing a phase transition to the space group $Pm\bar{3}n$, which possesses a higher degree of symmetry. The group-subgroup relationship between $P\bar{4}3n$, $Pm\bar{3}n$ and the highest possible symmetry for sodalites, $Im\bar{3}m$, the so-called aristotype, is shown in Figure 3 (right). The symmetry from $Im\bar{3}m$ to $Pm\bar{3}n$ is lowered by the ordering of chemically different T-atoms. Also shown is the spacegroup $I\bar{4}3m$, in which the second most sodalites are crystallizing. Compared to the aristotype, the site-symmetry of the oxygen atoms is lowered (e.g., $O(z) \neq 0.5$, meaning the framework is not fully expanded) but the tetrahedrally coordinated framework atoms T are not ordered or are built from the same element. Using the Landau theory, phase transitions can be described by the order parameter η , which becomes 0 at the critical temperature (T_c) of the phase transition [70, 71]. In the case of sodalites, the order parameter of the tri-critical $P\bar{4}3n$ to $Pm\bar{3}n$ phase transition is $\eta = z' = 0.5 - z$, with z being the $O(z)$ coordinate of the oxygen atom in the framework [72]. Using the equation

$$z' = A(T_c - T)^\beta \quad (2)$$

where A is a positive constant value and β is the critical exponent, the behavior of the order parameter can be described, and the critical temperature can be determined.

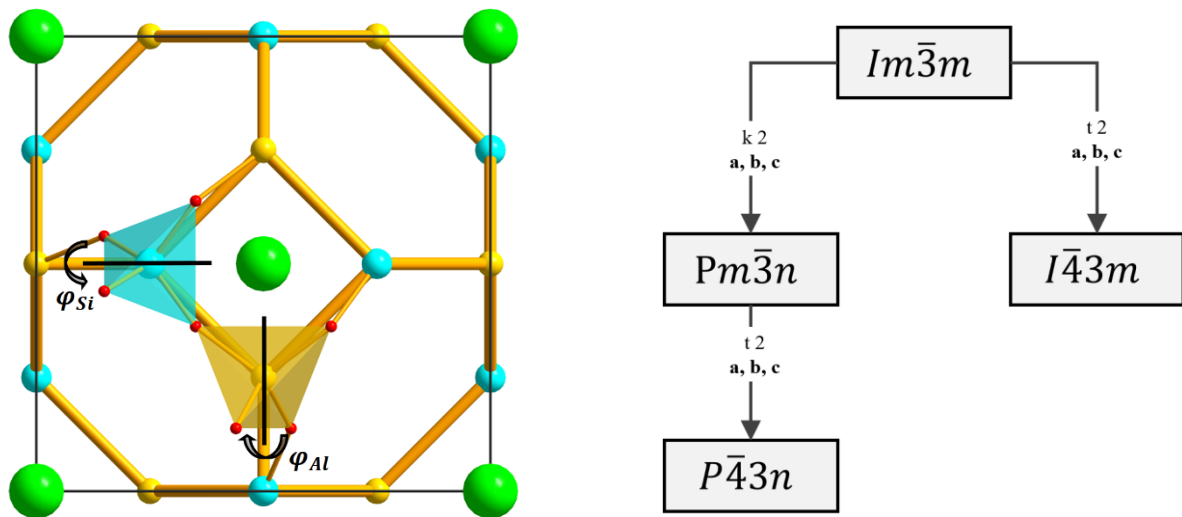


Figure 3: (left) Tilt angles of the SiO_4 and AlO_4 tetrahedra around their respective axes, shown for one tetrahedron each in an otherwise directly T-T linked framework (compare Figure 1 and Figure 2, Na atoms omitted, viewed in direction of the c axis). (right) Selected group-subgroup relationships in sodalites.

To summarize, all authors of previous reports agree on the tilting of tetrahedral units as the basic mechanism of the thermal expansion in sodalites, but they disagree on its origin, which is

either assumed in the expansion of the Na–X bond (Hassan [36, 40]), the expansion of the framework itself (Dempsey and Taylor [38]) or the coupled motion of sodium and the framework tetrahedra (McMullan [39]). The reviewed literature also shows that phase transitions below 300 K and deviations from the average structure in $P\bar{4}3n$ are possible to occur for some halide sodalites, but the behavior of most of them has not been investigated extensively yet at low temperatures. However, a different approach to clarify the interactions in sodalites could be the investigation of different macroscopic and microscopic properties in a series of compounds, where the atoms are systematically substituted, to subsequently search for relations between them. In this context, the term “macroscopic properties” refers to properties which can be observed macroscopically with bulk quantities or large single crystals of a material, like the decomposition temperature or thermal expansion. The term “microscopic properties” refers to properties on the atomic level, like the atomic structure or the distribution of phonons in a material. Microscopic properties must be linked to macroscopic properties. There are no studies available yet, which consider these questions or follow this approach.

In the present work, framework and template ions were systematically varied. Four different framework compositions $[\text{Na}_8\text{X}_2][\text{T}^1\text{T}^2\text{O}_4]_6$ are considered, where the Al and Si atoms centering the tetrahedra are replaced by Ga and Ge ($\text{T}^1 = \text{Al, Ga}$; $\text{T}^2 = \text{Si, Ge}$). Additionally, the chloride ions are replaced by bromide or iodide ($\text{X} = \text{Cl, Br, I}$) each, leading to a total of twelve different chemical compositions. For all these samples, multiple properties have been investigated by different experiments and calculations. Examined macroscopic properties were the decomposition temperature and the amount of cage-incorporated water, which were determined by simultaneous thermogravimetry and differential scanning calorimetry; the thermal expansion of the compounds as well as the average structure was determined from X-ray scattering experiments by Rietveld refinements. Examined microscopic properties were the local atomic structure, which was determined by PDF-Rietveld refinements using synchrotron total-scattering data; information about the phonon densities of state (PDOS) was obtained from force-field calculations and from fittings of the thermal expansion with the Debye-Einstein-anharmonicity model; *ab-initio* molecular dynamics (AIMD) calculations were carried out, giving information about the displacement of atoms in the sodalite structure. Some of these methods will be presented in the following introductory chapters. For better readability, the chemical composition of the sodalites will sometimes be given in an abbreviated form denoting only the atoms centering the tetrahedra of the framework and the incorporated halide ion (e.g., $[\text{Na}_8\text{Br}_2][\text{GaSiO}_4]_6 = \text{GaSiBr}$)

1.2 The Debye-Einstein-anharmonicity model and thermal expansion coefficient

Applying the Einstein or Debye model, the vibrations of a system as represented by the phonon density of states (PDOS) can be described with a single frequency ω_E or ω_D , respectively. The Einstein model assigns an average frequency for all modes, which applies over a broad temperature range but fails at low temperatures where acoustic modes are dominating. The Debye model describes the vibrations as a continuum up to the cut-off frequency ω_D and fits well also at low temperatures. When used for the representation of thermodynamic functions, ω_E and ω_D are treated as adjustable phenomenological parameters [70]. It is also possible to use multiple parameters to describe the vibrations of a system, as frequently done when fitting the thermal expansion of systems using the Debye-Einstein-anharmonicity (DEA) model.

The DEA model [55, 56, 62] makes use of the first order Grüneisen approximation for the zero-pressure equation of states, where a temperature-dependent metric parameter (M) is expressed as:

$$M(T) = M_0 + \frac{\gamma}{K_0} U(T) \quad (3)$$

with M_0 as the metric parameter at 0 K containing the zero-point energy, γ as the thermodynamic Grüneisen parameter, and K_0 as the isothermal bulk modulus. γ and K_0 are treated together as the thermoelastic parameter $k = \gamma/K_0$. To describe the internal vibrational energy $U(T)$, multiple Debye and Einstein terms can be used together with terms for the low-perturbed anharmonicity:

$$M(T) = M_0 + \sum_{i=1}^d k_{Di} U_{Di}(T) + \sum_{i=1}^e k_{Ei} U_{Ei}(T) + \sum_{i=1}^a k_{Ai} U_{Ai}(T) \quad (4)$$

The k_x are the respective thermoelastic parameters and the U_x are the internal Debye (U_{Di}), Einstein (U_{Ei}) and anharmonic (U_{Ai}) energies, containing the Debye ($\theta_D = hc\omega_D/k_B T$) and Einstein ($\theta_E = hc\omega_E/k_B T$) temperatures as fitting parameters. In this thesis, only Einstein and Debye terms were used for fittings, having the form:

$$U_{Ei}(T) = \left[\frac{3Nk_B\theta_{Ei}}{e^{\frac{\theta_{Ei}}{T}} - 1} \right] \quad (5)$$

$$U_{Di}(T) = \left[9Nk_B T \left(\frac{T}{\theta_{Di}} \right)^3 \int_0^{\frac{\theta_{Di}}{T}} \frac{x^3}{e^x - 1} dx \right] \quad (6)$$

where N is the number of atoms per unit cell and k_B is the Boltzmann constant.

The instantaneous volume thermal expansion coefficient (TEC, $\alpha_{I,vol}(T_m)$) is very sensitive for changes in the thermal expansion and thus is used to fit the DEA models against. It is calculated with the refined unit-cell volumes for each sample as given by James et al. [73]:

$$\alpha_{I,vol}(T_m) = \frac{1}{V_0} \frac{V_{n+1} - V_n}{T_{n+1} - T_n}; T_m = \frac{T_{n+1} + T_n}{2} \quad (7)$$

where T_n , T_{n+1} , V_n and V_{n+1} are the temperatures and cell volumes of the respective data sets n and $n + 1$. V_0 is the volume at 0 K as obtained by a DEA fit.

1.3 X-ray diffraction: Bragg scattering and total scattering

One of the most widely used analytical methods in solid state chemistry is powder X-ray diffraction. For a typical laboratory experiment, the (sharp) Bragg peaks are analyzed, which contain information from the long-range order of a system. The remaining parts of a recorded diffraction pattern are normally treated as the background, which can be modelled with one or multiple functions and is subtracted from the pattern. Through Rietveld refinement, the time- and space-averaged structure of a compound can be modelled, including the lattice, atomic positions, occupancy of positions and the thermal movement and structural displacement of atoms [74, 75].

However, this is not everything that can be retrieved from a powder pattern. The diffuse scattering intensity in between and underneath the Bragg peaks contains information about the local structure of compounds. By recording a diffraction pattern of the empty instrument without sample and using this as the background to be subtracted from the sample measurement, one can analyze the total scattering of a compound. Through mathematical conversions, which are a Fourier transformation of the normalized total measured diffraction data of a sample, the atomic pair distribution function (PDF, also represented by $G(r)$) is calculated. This function contains the information about the local structure from the diffuse scattering in a real space representation of the probability of finding pairs of atoms separated by a given distance [76, 77].

To obtain a PDF of sufficient resolution in real space, some aspects must be considered during the experiment: The used energy of the photons and the maximum investigated diffraction angles must be higher than in standard X-ray diffraction experiments to gather information up to a high Q-space. Also, very good counting statistics and a low background are needed. Therefore, many total scattering experiments are carried out at specialized beamlines at synchrotron or neutron facilities, although laboratory machines for the measurement of PDFs are becoming more available.

1.4 The bond valence model

The concept of bond valence [78, 79] is an empirical model of bonding in inorganic chemistry. It connects the length of a bond with its strength, which is called valence within this concept to differentiate it from Pauling's bonding strength [80]. The model's rules are physically explained by the flux theory, in which the atoms are represented by point charges at the positions of the nuclei which are linked by Faraday's lines. They form an electrostatic field called the electrostatic flux or the Madelung field [81]. The electrostatic flux, which links an anion and a cation, is called bond flux, and equals the bond valence. Its magnitude is determined by the charges it links, so that the sum of bond fluxes around an ion is equal to the ionic valence or charge, as given by equation (8):

$$V_i = \sum_j \Phi_{ij} \quad (8)$$

where V_i is the valence of atom i , and Φ_{ij} are the N_i fluxes to its ligands j . While this rule is exactly true for the bond fluxes, experimentally determined bond valences s_{ij} are subject to experimental uncertainty in determining the bond lengths, so that equation (9), the *valence sum rule*, follows:

$$V_i \approx \sum_j s_{ij} \quad (9)$$

In this case, V_i is also called the *bond valence sum* (BVS). The bond valences s_{ij} can be calculated from equation (10):

$$s_{ij} = e^{\left(\frac{R_0 - R_{ij}}{b}\right)} \quad (10)$$

where R_{ij} is the measured bond length. R_0 and b are empirical parameters, depending on the two bonded atoms. A collection of parameters is compiled by I. D. Brown and published online by the International Union of Crystallography (IUCr) [82], including the ones used in this thesis [83, 84].

2. Experimental details

2.1 Syntheses

All sodalites were synthesized hydrothermally under autogenous pressure in steel autoclaves containing 50 mL polytetrafluoroethylene (PTFE, Teflon) tubes. As starting materials, NaAlO₂ (Alfa Aesar, Lot: T14C030), Na₂SiO₃ (Alfa Aesar, Lot: M16B050), NaGaO₂ and Na₂GeO₃ were used. They were mixed to a gel with the respective halogenide salt (NaCl (AnalaR NORMAPUR, Lot: 14D150019), NaBr (MERCK, Lot: K37001860) or NaI (AnalaR NORMAPUR, Lot: 1L007838)) and a freshly prepared solution of NaOH (AnalaR NORMAPUR, Lot: 17L214125) in deionized water and transferred to the autoclaves. Reaction parameters like the amount of reactants, volume and NaOH-concentration of the solution, reaction time and temperature were varied to obtain products as crystalline and phase pure as possible. The synthesis conditions of the sodalites chosen for further analysis are shown in Table 1.

The reactants NaGaO₂ and Na₂GeO₃ were synthesized by thoroughly grinding mixtures of stoichiometric amounts of Na₂CO₃ and Ga₂O₃ (Alfa Aesar, Lot: J22Y059) or GeO₂ (Alfa Aesar, Lot: U28E055 or Aldrich, Lot: MKBJ6362V), respectively. These mixtures were placed in porcelain crucibles and heated to 1100 K in a furnace for 65 h. The products were checked upon phase purity by powder X-ray diffraction (PXRD) prior to further use. Structure information can be retrieved from the Inorganic Crystal Structure Database (CSD numbers see Table 1).

Table 1: Experimental parameters of the hydrothermal syntheses. (T¹ = Al or Ga, T² = Si or Ge, X = Cl, Br or I)

Sample	m (NaT ¹ O ₂) /g	m (Na ₂ T ² O ₃) /g	m (NaX) /g	V (NaOH) /mL	c (NaOH) /(mol/L)	T /K	t /h	CSD Number
AlSiCl	1.27	0.85	6	20	8	473	64	2128568
AlSiBr	1.27	0.85	6	20	8	473	64	2128569
AlSiI	1.27	0.85	6	20	8	473	64	2128572
GaSiCl	1.00	1.80	13	10	2	473	69	2128577
GaSiBr	1.00	1.00	13	5	2	423	64	2128574
GaSiI	1.00	1.00	13	10	2	473	65	2128576
AlGeCl	0.64	1.30	15	10	6	433	62	2128571
AlGeBr	0.64	1.30	15	10	6	433	62	2128566
AlGeI	0.64	1.30	15	10	6	433	62	2128567
GaGeCl	1.00	1.34	10	5	2	453	66	2128573
GaGeBr	1.39	1.85	15	5	2	453	66	2128570
GaGeI	1.39	1.85	15	5	0	423	48	2128575

2.2 Spectroscopy

2.2.1 Raman spectroscopy

Raman spectra were recorded from 35 cm^{-1} to 1600 cm^{-1} using a LabRAM Aramis (Horiba Ltd., Kyoto, Japan) equipped with an Olympus BX41 microscope, a x100 objective and a 1800 mm^{-1} grating. A laser with an excitation wavelength of 533 nm was used. The spectra were corrected manually by subtracting a linear background and normalized with respect to the area of the maximum peak of each spectrum. Selected peaks were fitted with the software *Fityk* [85] using pseudo-Voigt functions, where the shape parameter was constrained to be equal for all peaks in the fitting range and allowed to vary from 0 to 1. This was done for each spectrum in multiple parts which were chosen according to the grouping of the peaks, using another linear background for each part.

2.2.2 Infrared (IR) spectroscopy

IR spectra were recorded either on a Nicolet iS10 FTIR spectrometer (Thermo Scientific, Waltham, Massachusetts, USA) (GaSiBr and GaGeI sodalite) with the attenuated total reflection (ATR) technique, or an IFS 66v/S FTIR spectrometer (Bruker Optics GmbH, Ettlingen, Germany) (remaining compounds) using pressed KBr pellets which contained ca. 1 % of the respective sample.

2.3 Thermal analysis

Simultaneous thermogravimetric analysis (TGA) and differential scanning calorimetry (DSC) were carried out using a TGA/DSC 3+ system (Mettler Toledo GmbH, Gießen, Germany). All samples were measured in $70\text{ }\mu\text{L}$ corundum crucibles from 300 K well into the range where decomposition occurs with a heating rate of 10 K/min, except for the aluminosilicates, which were measured with a rate of 5 K/min. A flow of 20 mL/min N_2 was used as a protecting atmosphere. Some measurement programs contained a step of holding the temperature at 383 K for 15 min to ensure full evaporation of surface water before the onset of the loss of cage-contained water. The amount of water loss was determined by the difference in mass in the respective temperature range between two constant sections. It has an estimated error of 0.05 %, as the mass curve does not always end up in a horizontal line before and after the effect. From this, the number of water molecules, which would on average be present per cage, was calculated. The decomposition temperature was determined as the onset temperature of the DSC signal in the temperature range where rapid mass loss is starting using the STAR^e-software by Mettler Toledo.

2.4 Powder X-ray diffraction (PXRD)

2.4.1 Ambient temperature PXRD

Ambient condition powder X-ray diffraction data were collected on a Stadi MP diffractometer (STOE & Cie GmbH, Darmstadt, Germany) in a glass capillary (outer diameter = 0.3 mm) in Debye-Scherrer geometry, using MoK α_1 radiation ($\lambda = 70.9300(2)$ nm). The instrument was equipped with a Ge(111) monochromator and a Mythen2 R 1K strip detector (Dectris Ltd., Baden-Daettwil, Switzerland).

2.4.2 Temperature-dependent PXRD

High-temperature (HT) powder X-ray diffraction data were collected on a X'Pert Pro diffractometer (PANalytical, Almelo, Netherlands) with a HTK1200N high-temperature chamber (Anton Paar, Graz, Austria) in Bragg-Brentano geometry. The diffractometer was equipped with a secondary Ni-filter, a X'Celerator detector system and used CuK $\alpha_{1,2}$ radiation ($\lambda = 154.0596(1)$ pm, 154.4493(1) pm). Datasets were collected starting at 300 K in steps of 10 K in a 2θ range from 10° to 130°, measuring for 30 s per step with a step-width of 0.0167°. The dataset of the AlSiI sodalite was supplied by Robben et al. [29] and the datasets of the gallogermanate sodalites recorded by Poltz [86] were used.

Low-temperature (LT) powder X-ray diffraction was carried out under vacuum (pressure below 0.1 Pa) on a Stadi MP diffractometer (STOE & Cie GmbH, Darmstadt, Germany), equipped with a Phenix cryostat (Oxford Cryosystems, Oxford, UK), in reflection geometry. Monochromatic (Ge(111)) MoK α_1 radiation and a Mythen2 R 1K strip detector (Dectris Ltd., Baden-Daettwil, Switzerland) were used. Datasets were recorded from 293 K down to 18 K in steps of 10 K or less.

2.4.3. Rietveld refinements

Rietveld refinements were performed using the fundamental parameter approach with the software *TOPAS V6* (Bruker AXS, Karlsruhe, Germany). The fundamental parameters were obtained by fitting against a measured dataset of a LaB₆ standard material. Datasets obtained by temperature-dependent measurements were refined in sequential batch mode. For the evaluation together with HT results, the bond lengths and lattice parameters from the refinements of the LT data were shifted by a constant value to the HT data, because their quality (measured counts, resolution, background) is higher than that of the LT data. This procedure gives a seamless trend.

2.5 Total scattering experiments at DESY

Total scattering data at ambient conditions were collected at the “Swedish Materials Science” (SMS) beamline P21.1 at PETRA III (DESY, Hamburg, Germany). Photons with an energy of 101.67(3) keV ($\lambda = 12.20(4)$ pm) and a Perkin Elmer XRD1621 area detector at a distance of 370 mm were used. The samples were prepared in 1 mm polyimide (Kapton) capillaries and measured for 60 s each. Obtained 2D data was integrated using *DAWN 2* [87] after calibrating the instrument geometry with a measured Ni standard material. From the 1D diffraction data of the samples and an empty sample container background measurement the reduced pair distribution function $G(r)$ (PDF) was calculated using *PDFgetX3* [88]. The PDFs were modelled with *PDFgui* [89] up to a distance of at least 4.3 nm using a single, symmetry constrained unit cell (PDF-Rietveld) of the sodalite structure in space group $P\bar{4}3n$ with the results of in-house PXRD experiments as starting values. The displacement parameters of O and Na atoms were refined anisotropic, while the ones of the cations in the framework and of the halide ions were refined isotropic.

Total scattering data of $[\text{Na}_8\text{X}_2][\text{GaGeO}_4]_6$ ($\text{X} = \text{Cl}, \text{Br}, \text{I}$) between 300 K and 100 K in steps of 10 K were collected at the “Powder Diffraction and Total Scattering” beamline P02.1 at PETRA III (DESY, Hamburg, Germany). Photons with an energy of 59.78(3) keV ($\lambda = 20.74(4)$ pm) and a Perkin Elmer XRD1621 area detector at a distance of 270 mm were used, with the beam centered in a corner. A Cryostream (Oxford Cryosystems, Oxford, UK) liquid nitrogen blower was used for cooling. The samples were prepared in 0.3 mm quartz-glass capillaries and measured for 600 s at each temperature step. Obtained 2D data was integrated using *DAWN 2* [87] after calibrating the instrument geometry with a measured LaB_6 standard material and the $G(r)$ of the data were calculated with *PDFgetX3* [88] as described above. Modelling of the PDFs was carried out with *PDFgui* [89] as described in the respective chapters (3.8 Ambient temperature total scattering, *ab-initio* MD calculations and 3D-BVS and 3.9 Temperature-dependent total scattering).

2.6 3D-BVS

The hypothetical bond valence sum [79, 83, 84] of Na in the twelve sodalite structures was calculated for every position of a 3-dimensional grid within the center cage. For this, the atomic positions and cell parameters determined at 300 K for all the other atoms were used to calculate the distances to all atoms from each grid point in one unit cell. The grid had a spacing of the lattice parameter divided by 40 in every axial direction, resulting in 40^3 voxels for every structure. The presented data visualizations were created with *ParaView* [90].

2.7 *Ab-initio* molecular dynamics calculations

Electronic structure calculations were performed using density functional theory (DFT). The exchange-correlation interaction was treated by the generalized gradient approximation using the PBE functional [91]. The effect of the core electrons on the valence density was taken into account by means of the projector-augmented wave (PAW) method [92] with an energy cutoff of 415 eV and a kinetic energy cutoff of 645 eV.

Unit-cell parameters and atomic positions have been optimized using GPAW in the framework of the Atomistic Simulation Environment (ASE) [93, 94]. A $6 \times 6 \times 6$ k-point mesh and the k-point sampling scheme of Monkhorst and Pack [95] were used in all calculations. All atoms were allowed to freely relax, and no symmetry restrictions were given.

Ab-initio Molecular Dynamics simulations (AIMDs) were calculated using the *Vienna Ab initio Simulation Package* (VASP) [96]. A $3 \times 3 \times 3$ k-point mesh was used in all calculations. Each optimized bulk structure was heated up to 298.15 K for 1 ps of simulation time by means of an NVT ensemble. Here the temperature ramping was controlled by a Nosé-Hoover thermostat, with a time step of 0.5 fs for the Verlet algorithm and direct scaling performed every 10 steps. Once the room temperature had been reached, the systems were allowed to further stabilize for another 1 ps within the same NVT ensemble. Finally, with use of an NVE ensemble the dynamics were investigated for up to 10 ps at the thermodynamic equilibrium.

2.8 Force-field calculations

Force-field calculations were carried out using version 6 of *GULP* [97, 98]. A consistent set of potential parameters was obtained using the *ParamGULP* code [99] and fitting the potential parameters to the ambient structures, starting with the AlSiCl sodalite. Initial potential parameters were taken from Sierka and Sauer [100] for the framework interaction, from Binks [101] for the Na-Cl interaction and Jackson and Catlow [102] for the Na-O interaction. The potentials were first adapted to the template within the same framework (1: Cl, 2: Br, 3: I) and then the framework was switched (Al-Si, Al-Ge, Ga-Si, Ga-Ge), keeping the parameters from the step before. Finally, an optimization with a phonon calculation was carried out to obtain the phonon density of states.

3 Results and discussion

3.1 Ambient average structure

Characterization of the sodalite samples at ambient temperature was done by X-ray diffraction experiments and subsequent Rietveld refinements. The samples were found to be phase pure and highly crystalline. Results of the structure refinements in space group $P\bar{4}3n$ (Nr. 218) yielded average structures in agreement with the literature and are presented in the appendix (Figure A 1-A 12, Table A 1-A 24).

3.2 Spectroscopy

3.2.1 Raman spectroscopy

High-quality Raman spectra starting at a low Raman shift of 25 cm^{-1} of all samples were recorded and are shown in Figure 4. They show only the bands expected for phase-pure sodalites and are agreeing with the literature [16, 86, 103-105]. The main appearance of the spectra is similar, especially for compounds of the same framework composition. With calculated positions and vibration types of Raman bands published for AlSiCl and AlSiBr sodalite, the spectra of the aluminosilicates can be divided into four regions of vibrations, marked by dashed lines in Figure 4 [103, 104, 106]. The region above 900 cm^{-1} contains the bands mostly produced by asymmetric Si-O-Al stretching (ν_{as}), the next lower region down to 550 cm^{-1} contains the symmetric Si-O-Al stretching (ν_{s}). Bands between 200 cm^{-1} and 550 cm^{-1} are produced predominantly by inter- (δ Si-O-Al) and intra-tetrahedral (δ O-T-O) bending motions. The region below 200 cm^{-1} contains bands produced mainly by vibrations of the lattice and ions located in the sodalite cages. These four regions can be found in the same order for all framework compositions but are not always divided by distinct gaps in the spectra.

An easy assignment of bands in the different spectra based on the comparison of band positions, intensities and widths is only possible for bands of high relative intensity or nearly unchanging position. This is the case for the most intense band of every spectrum (δ T¹-O-T²) and the most intense band of the asymmetric stretching vibrations (ν_{as} T¹-O-T²). Their fitted positions and widths for all compounds are shown in Figure 5. The position of the ν_{as} T¹-O-T²-peak is blueshifted for larger incorporated halide ions and redshifted for frameworks of larger volume, resulting in four distinct groups. Where their position can be followed, other asymmetric stretching modes are shifting to the same direction. No trend can be seen for the width of the ν_{as} T¹-O-T² peak. The δ T¹-O-T²-peak is redshifted for larger halide ions but does not directly

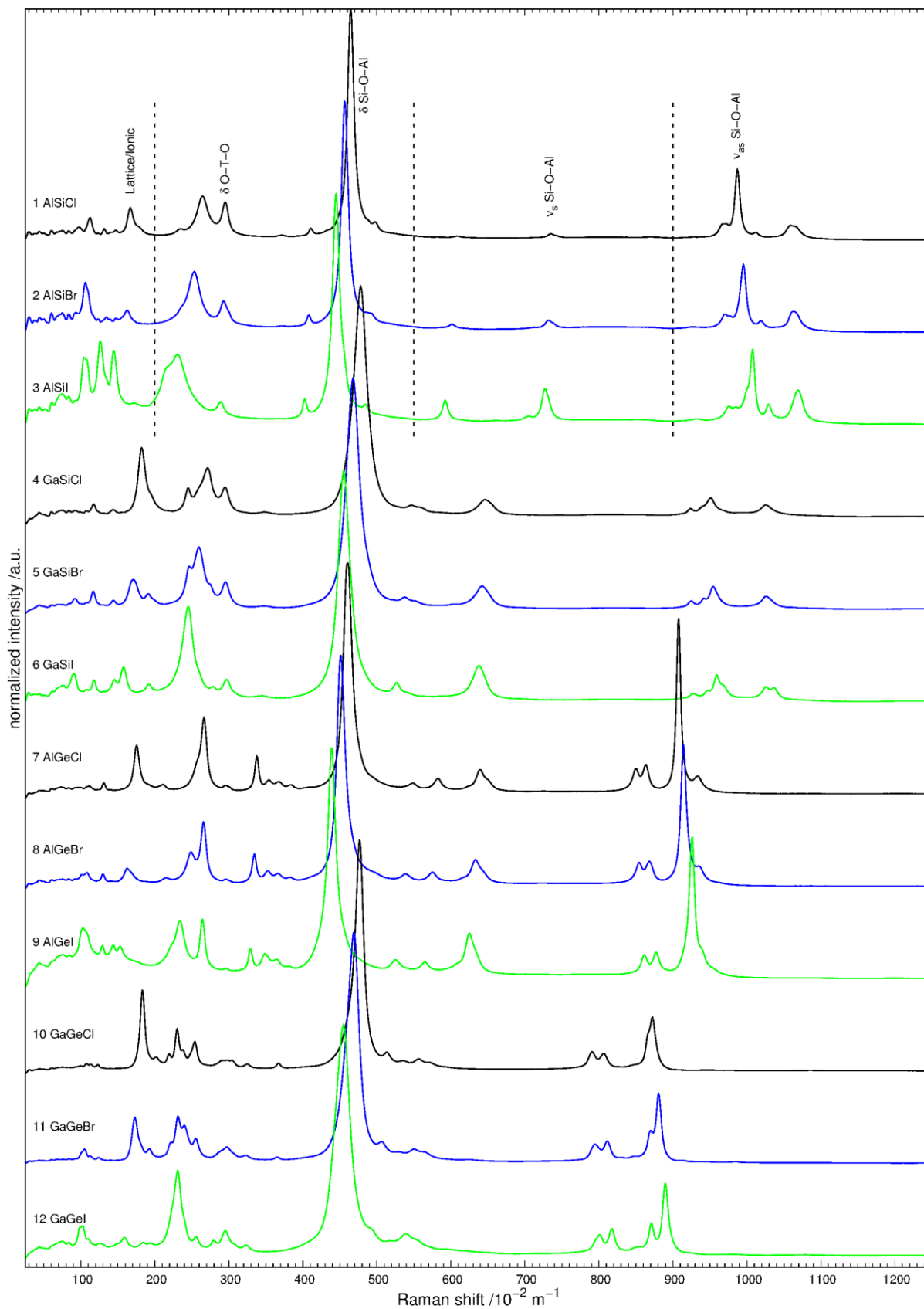


Figure 4: Raman spectra of all twelve sodalites, ordered in groups of increasing framework-volume and increasing halide-ion size (black: Cl⁻, blue: Br⁻, green: I⁻) from top to bottom. Intensity normalized to the maximum peak.

correlate with the framework volume. With respect to the framework type, the peaks are shifted to higher energies following $\text{Al-Ge} < \text{Al-Si} < \text{Ga-Ge} \approx \text{Ga-Si}$. For the Al-Si and Ga-Ge frameworks, the peaks are becoming wider with increasing halide ion size and for the Ga-Si and Al-Ge frameworks they are narrowing. With widths over 20 cm^{-1} , all Ga-Si compounds have significantly broader peaks than the other sodalites. This reflects the large difference in length between the two T–O bonds compared to the other frameworks.

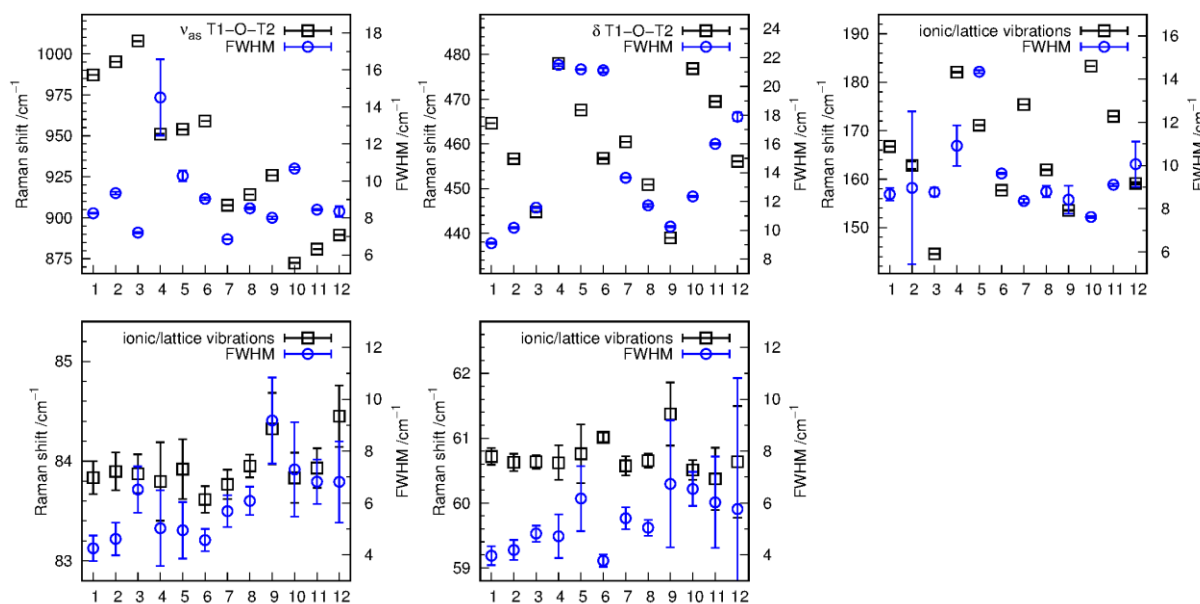


Figure 5: Positions and FWHMs of selected Raman peaks which can be identified for every investigated sodalite. All peaks are labeled in Figure 4 or marked by an arrow in Figure 6. The different sodalites are numbered from 1 to 12 in order of increasing halide ion size and framework volume (compare labels in Figure 4).

While all peaks above 300 cm^{-1} are shifting and gaining or losing intensity gradually when the enclathrated ion is exchanged, peaks in the region between 90 cm^{-1} and 300 cm^{-1} are behaving very different. The spectra of chlorine and bromine compounds of a single framework are looking relatively similar compared to the respective iodine compound, where single peaks are gaining and losing much intensity, often obscuring surrounding signals in the process. This can be seen most pronounced for the AlSiI sodalite, where a characteristic fork-shape around 125 cm^{-1} emerges. A magnification of the spectral region below 320 cm^{-1} is shown in Figure 6, where the spectra are ordered in groups according to the respective halide ion. The peaks marked by arrows above the AlSiCl spectrum can be identified in all spectra and their fitted properties are shown in Figure 5. The peak sitting at 166.7 cm^{-1} for the AlSiCl sodalite is induced by ionic vibrations and shows a behavior similar to the $\delta \text{T}^1\text{-O-T}^2$ peak discussed above with the blueshift of the position upon halide-ion exchange. The peaks of different frameworks

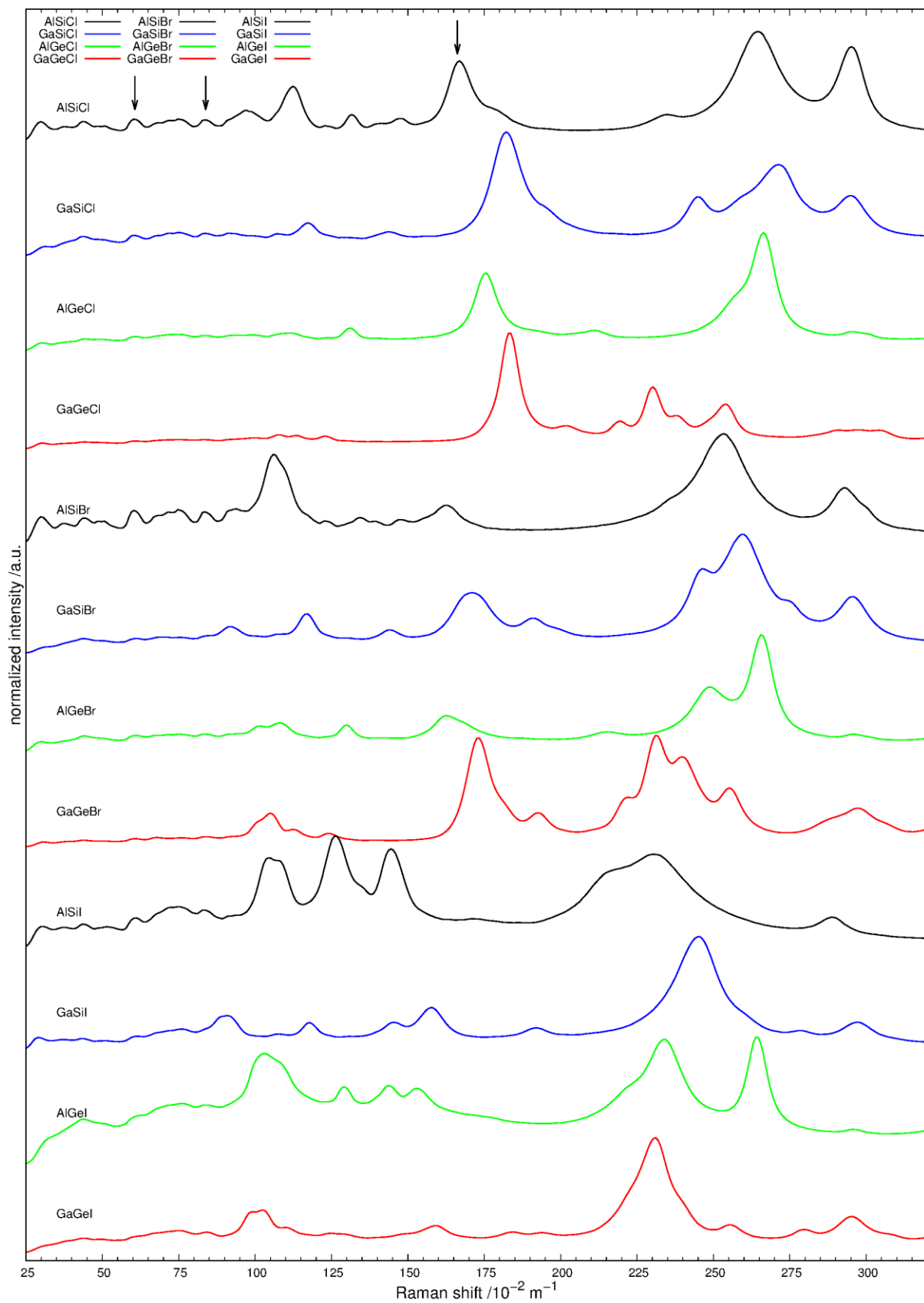


Figure 6: Raman spectra in the region between 25 cm^{-1} and 320 cm^{-1} , ordered in groups of increasing halide-ion size and increasing framework-volume (black: Al-Si, blue: Ga-Si, green: Al-Ge, red: Ga-Ge) from top to bottom. Intensity normalized to the maximum peak (δ Si-O-Al in Figure 4).

are spread over energy ranges following the order Al-Si < Al-Ge < Ga-Ge \approx Ga-Si to higher shifts.

The enlargement of the lower spectral region makes some characteristics of the peaks below 90 cm^{-1} obvious: First, they are most intense for the alumosilicate sodalites and least intense for the gallogermanates. This, together with an in some cases non-linear background below 60 cm^{-1} makes a stable fitting of all peaks impossible, but they can still be seen with the eye. Second, all peaks are staying at virtually the same position across the different chemical compositions. This is clearly shown by the fitted positions of the two peaks at 84 cm^{-1} and 61 cm^{-1} in Figure 5.

To summarize, fitted positions of the peaks related to vibrations of the framework depend on the chemical composition and geometry of the compounds. Most bands between 100 cm^{-1} and 300 cm^{-1} are shifting and gaining or losing intensity rapidly depending on the composition, making an identification and comparison without further knowledge difficult. This cannot be conducted properly consulting published calculations, where the focus either lies on a single compound (AlSiCl or AlSiBr sodalite) [103, 104, 106, 107], examinations of the qualitative appearance of multiple spectra [108, 109] or natural samples with mixed cage contents [110].

3.2.2. IR spectroscopy

The IR spectra (Figure 7) show the bands typical for the respective sodalite frameworks below 1200 cm^{-1} [16, 21, 111-113]. As for the Raman spectra, the vibration types of the framework can be found in different regions, with the asymmetric vibrations $\nu_{\text{as}} \text{T}^1\text{-O-T}^2$ approximately above 700 cm^{-1} , the symmetric modes $\nu_{\text{s}} \text{T}^1\text{-O-T}^2$ between 500 cm^{-1} and 700 cm^{-1} and the bending vibrations $\delta \text{T}^1\text{-O-T}^2$ below 500 cm^{-1} . The respective groups are shifted to lower wavenumbers with larger frameworks and longer T-O bonds. The bands belonging to the tetrahedral sodium (NaO_3X) and halide (Na_4X) environment would be observed in the far infrared region below 300 cm^{-1} and could not be recorded with the instrumental setups. Additionally, in some samples weak H_2O bending modes at around 1650 cm^{-1} as well as the broad O-H stretching mode signal between 3200 cm^{-1} and 3600 cm^{-1} can be seen, but no sharp signals of hydroxyl groups around 3640 cm^{-1} appear in the spectra [46, 114, 115]. The always probable inclusion of water and/or hydroxyl-groups in the cages will be discussed further in the following section.

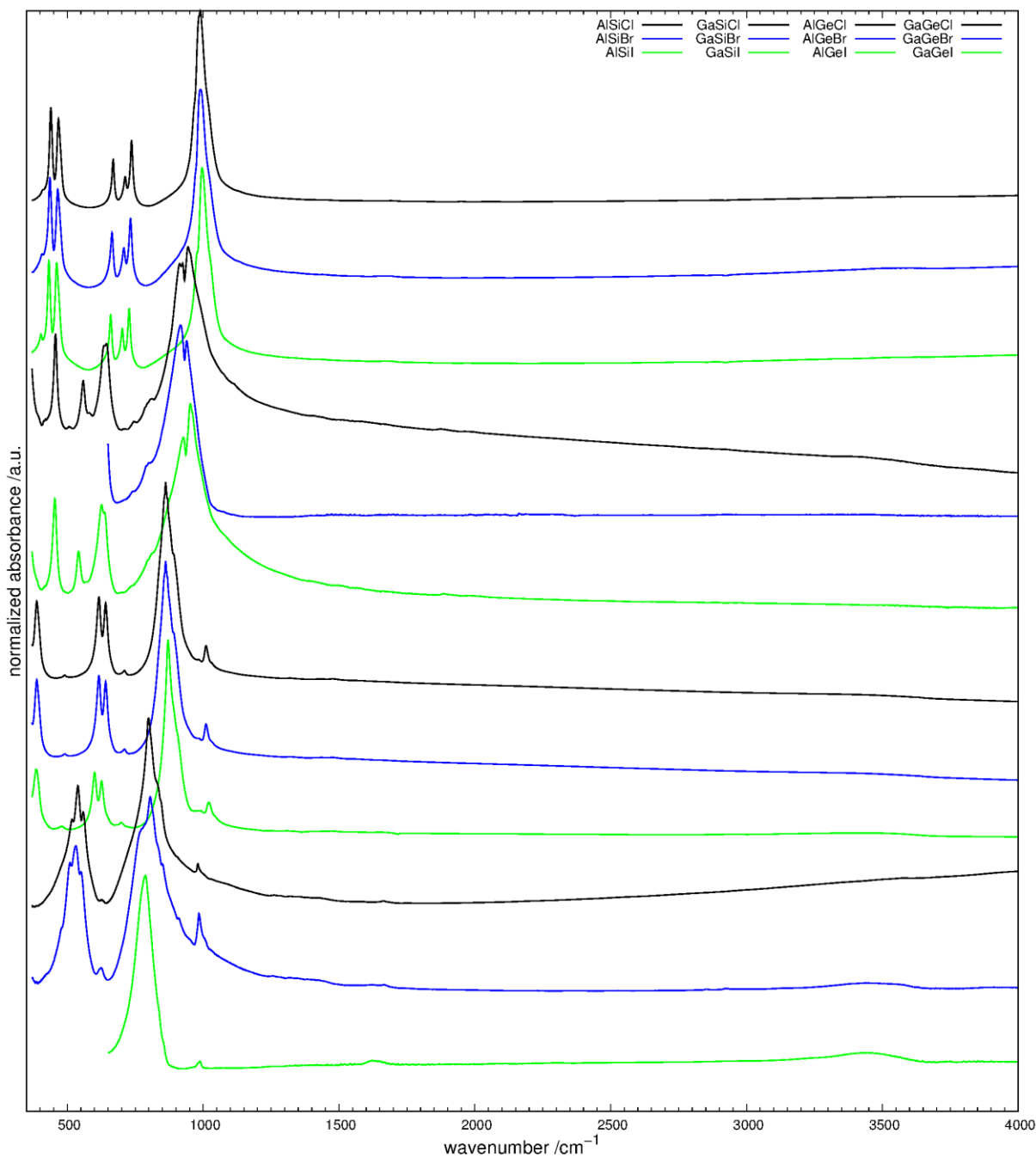


Figure 7: IR spectra of the investigated sodalites, ordered according to increasing volume of framework and incorporated halogenide-ion from top to bottom.

3.3 Decomposition and water loss (TGA/DSC)

To determine the decomposition temperatures and the water content, TGA/DSC measurements were performed. The general appearance of the TGA/DSC curves of the investigated sodalites (Figure 8) is principally the same and as expected for these compounds. The evaporation of surface-adsorbed water is in all cases finished at approx. 450 K, visible in the first mass loss in the TGA curve. Cage-incorporated water is lost in the temperature range between 500 K to

1000 K. In most cases, a two-step process in the TGA curve could be observed as described by Engelhardt et al. [114] for the water loss in pure hydro sodalites. Determined water contents are collected in Table 2. The highest water content was observed for the alumogermanate framework (0.41-0.44 molecules per cage (mpc)). The three gallogermanate sodalites show a broad range of different water content (0.19-0.42 mpc), the gallosilicate phases show medium water content (0.25-0.29 mpc) and alumosilicate sodalites the lowest, with the AlSiBr sodalite showing an almost doubled water content compared to the other two.

Decomposition of the sodalites is observed above 1050 K, with GaGeI sodalite as the only exception decomposing at 925(10) K. The associated mass loss is caused by framework destruction and evaporation of the metal halide. In all cases more or less pronounced signals or kinks are visible in this range of beginning mass loss, sometimes only noticeable in the first derivative (analogous to [116], e.g., AlGeCl). The onset of this effect was determined, and the results are listed as the estimated decomposition onset T_D in Table 2. If the maximum measurement temperature reached well into the process of decomposition, two minima in the DTG curve could be observed. This effect was also observed by Antao et al. [116]. In the temperature range of the decomposition, varying endo- and exothermic signals are visible in the DSC curves. These signals can be associated with the formation of the decomposition products. These were shown to be mostly carnegite-, nepheline- and beryllonite-type compounds, or a mixture of these [8, 117, 118]. A comparison of the onset temperatures of decomposition shows that for each framework type the chloride-containing species is the most temperature-stable one. In the alumosilicate, gallosilicate and alumogermanate systems, the structures incorporating bromide and iodide begin to decompose at almost equivalent temperatures. Only in the gallogermanate system, the chloride and bromide structures start to decompose at the same temperature and the iodide compound has a 200 K lower onset. Generally, the structures with larger framework atoms are less stable with respect to temperature. The observation correlates with the theoretical observation of the stability of sodalites [23].

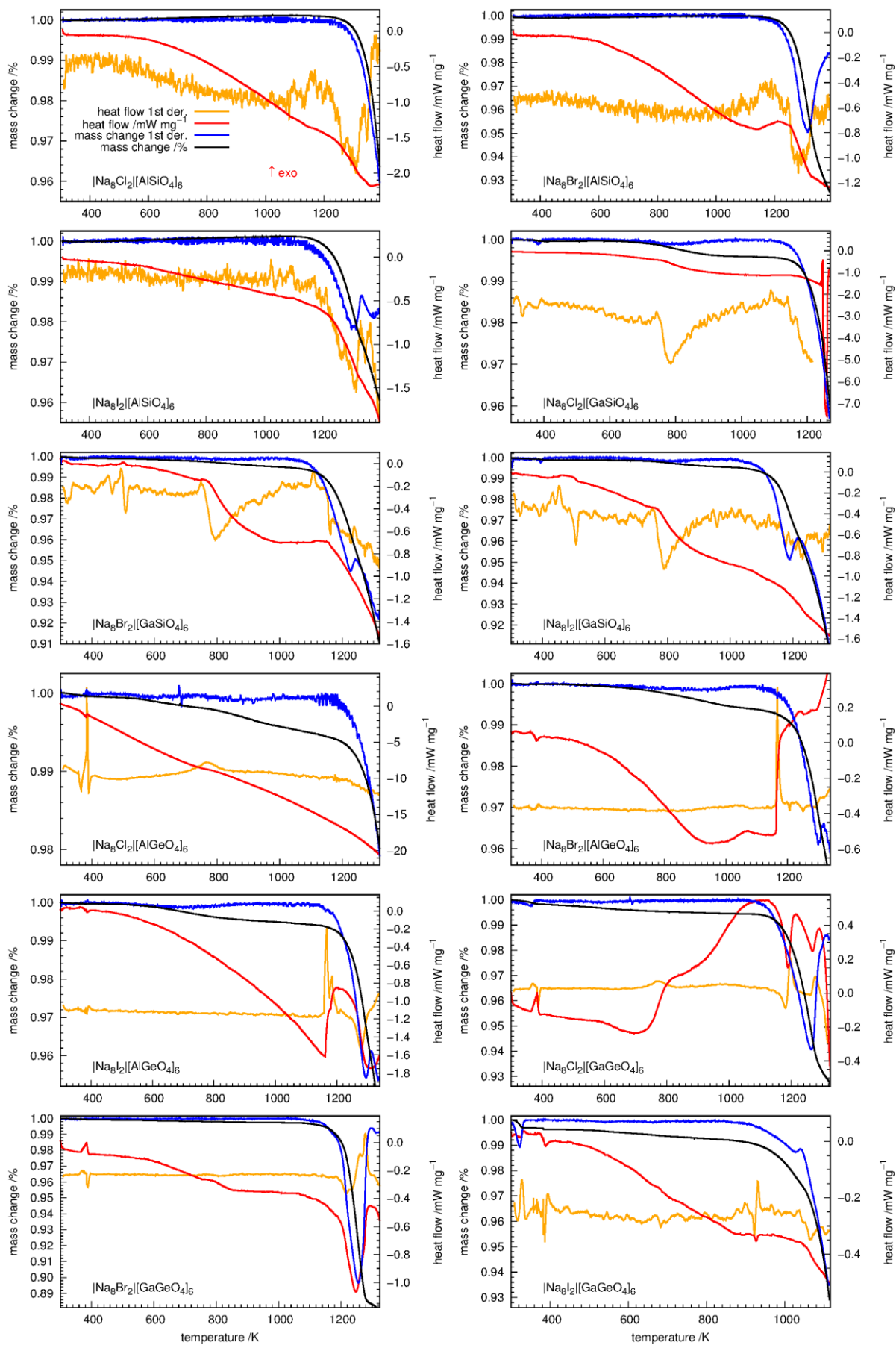


Figure 8: TGA (black) and DSC curves (red) as well as their first derivatives (blue: TGA, orange: DSC) for all twelve sodalites (composition given in each panel).

Table 2: Estimated decomposition onset T_D , water loss from cages (in % of total mass) and calculated average water molecules per cage (mpc).

Sample	T_D /K	water loss /wt-%	H ₂ O mpc
AlSiCl	1230(10)	0.23(5)	0.12(3)
AlSiBr	1170(10)	0.50(5)	0.29(3)
AlSiI	1175(10)	0.22(5)	0.14(3)
GaSiCl	1225(10)	0.36(5)	0.25(4)
GaSiBr	1160(10)	0.40(5)	0.29(4)
GaSiI	1075 (10)	0.33(5)	0.26(4)
AlGeCl	1210(10)	0.60(5)	0.41(4)
AlGeBr	1160(10)	0.60(5)	0.44(4)
AlGeI	1065(10)	0.55(5)	0.43(4)
GaGeCl	1125(10)	0.38(5)	0.32(5)
GaGeBr	1120(10)	0.22(5)	0.19(5)
GaGeI	925(10)	0.45(5)	0.42(5)

3.4 Thermal behavior of the average sodalite structure

Temperature-dependent powder X-ray diffraction data of all compounds were collected and analyzed by Rietveld structure refinements. The crystal structures of all twelve sodalites have been refined in space group $P\bar{4}3n$ over the complete examined temperature range. Selected bond lengths and the tilt angles have been calculated from the structural data. The values are analyzed and plotted against the temperature, up to those respective temperatures at which the e.s.d.'s become very large, often accompanied by significant trend changes. These changes arise when the structures are becoming unstable and maybe already start to decompose, resulting in data which cannot be refined properly. Deviations of the expected structural parameters influenced by the oxygen position for the GaGeCl and GaGeBr sodalite, visible especially below 300 K, are probably produced by the low scattering power of oxygen compared to Ga and Ge. These are the heaviest pair of atoms in the four examined frameworks. In general, refined parameters below 300 K show higher scattering and larger errors, as the data quality produced by the respective measurement setup is lower than that for the higher temperatures.

The cation-oxygen distances of the framework tetrahedra (Figure 9) could be distinguished for Si–O distances around 161 pm and the Ga–O distances around 182 pm. On the other hand, the Al–O and Ge–O distances are around 175 pm, quite close to each other due to the similar cation radii of 53 pm for Al and Ge [119, 120]. The strong scattering of the interatomic distances for the gallogermanate frameworks is due to the smaller scattering power of the oxygen atoms compared to the framework cations, resulting in a less precise determination of their positions. All bond lengths show a slight trend of shrinking with increasing temperature, which is an effect

of the averaging of oxygen positions [121, 122] and can be corrected for the librational motions of T–O tetrahedra if anisotropic displacement parameters from high-quality data (neutron diffraction e.g.) are available [39]. The data are in accordance with the concept of rigid tetrahedra, which show almost no temperature dependence of their bond lengths.

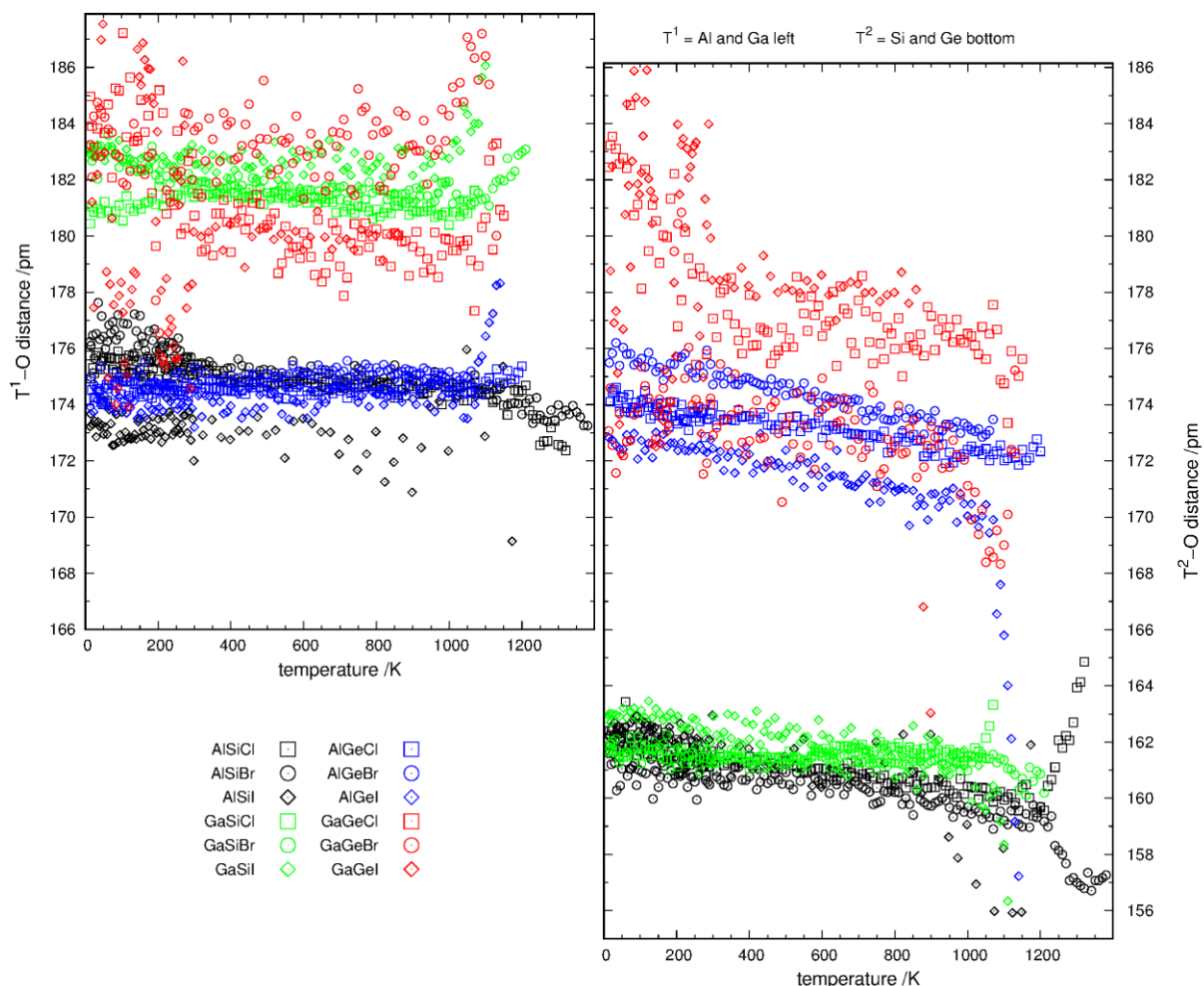


Figure 9: Temperature-dependent framework cation – framework oxygen distances (error bars are not plotted for clarity). The different frameworks are indicated by color and the incorporated halogenide ion by type of symbol.

The average tilt angle is decreasing with increasing temperature, showing the expansion of the frameworks (Figure 10, left). For the AlSiI and AlSiBr sodalite, the untilting is accelerated at ca. 900 K and 1200 K, respectively. At higher temperatures, the tilt angle remains at a constant value deviating slightly from zero due to the above-mentioned symmetry effect. This indicates the full expansion of the framework and is generally described as a $P\bar{4}3n \leftrightarrow Pm\bar{3}n$ phase transition [29, 72]. The Landau theory [71] has been applied to the results by fitting the parameters of equation (2) (see 1. Introduction) against the order parameter z' (Figure 11). According to the fitting, the results lead to transition temperatures of 1023(2) K and 1257(1) K for AlSiI and AlSiBr sodalite, respectively. The fitted value of the critical exponent β for

AlSiBr sodalite is significantly smaller than 0.25, which would be expected for a tri-critical phase transition and is observed here approximately for the AlSiI sodalite and by Rüscher et al. [72] for $[\text{Na}_8(\text{NO}_3)_2](\text{AlSiO}_4)_6$ sodalite. The transition of AlSiBr sodalite is happening after its determined decomposition onset at 1170(10) K, which may explain this deviation. For frameworks which are further away from full expansion with larger tilt angles ($> 25^\circ$) the decrease is almost linear. No signs for other phase transitions below 300 K could be observed.

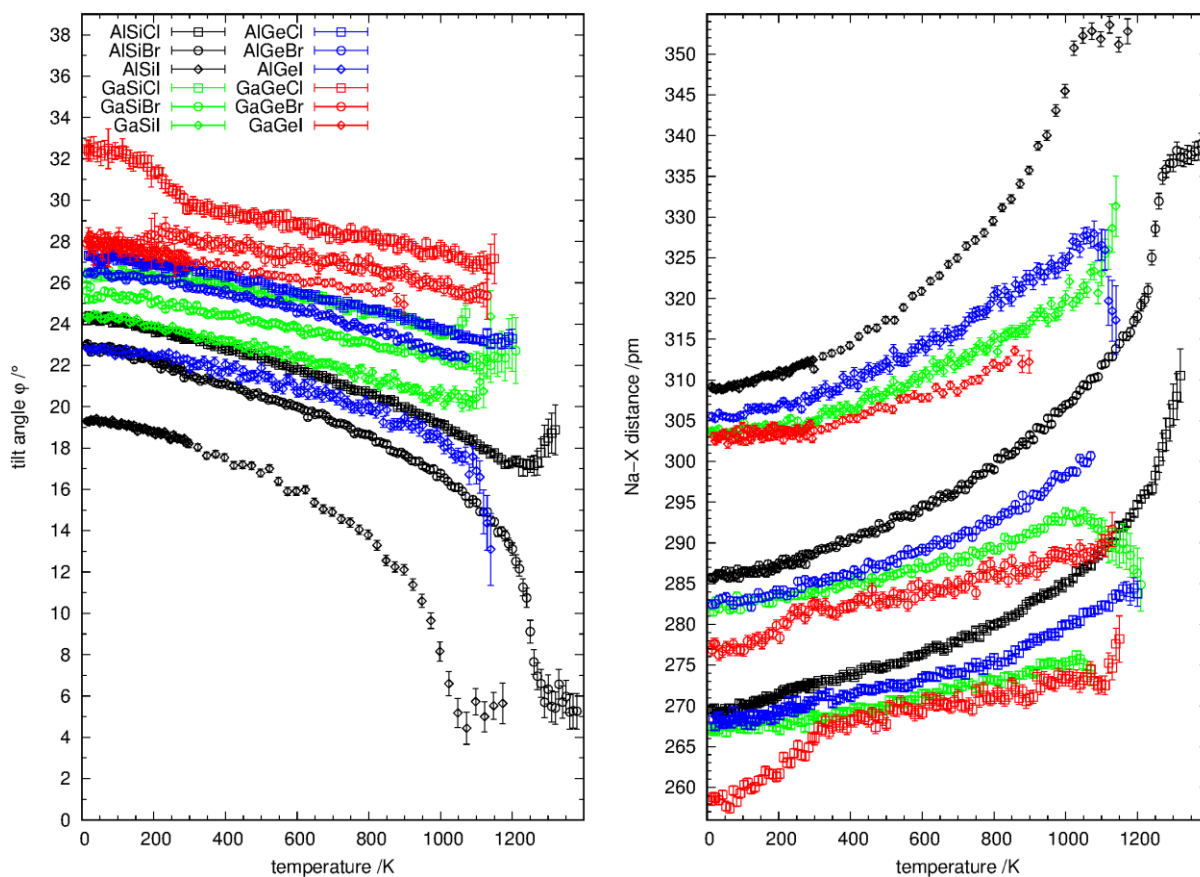


Figure 10: Temperature-dependent tilt angle (left) and Na-X distance (right) from PXRD refinements. The sodium-halide (Na-X) ion distances are ordered into three groups, belonging to the sodalites containing Cl⁻, Br⁻ and I⁻, respectively (Figure 10, right). Within these groups, the frameworks are ordered in the sequence Al-Si > Al-Ge > Ga-Si > Ga-Ge. Above the phase-transition temperature of AlSiBr and AlSiI sodalite, the Na-X distances show a drastically reduced expansion in the range up to decomposition, comparable to the change in the unit-cell volume (as described above). The smallest sodalites (Al-Si framework) show the largest volume of the Na-X tetrahedra and the largest framework (Ga-Ge) the smallest one. Ga-Si and Al-Ge seem to have swapped Na-X bond lengths, but in the first case, the bond lengths difference between Ga-O and Si-O is the biggest one. In the second case the difference between the Al-O and Ge-O distances is almost 0.

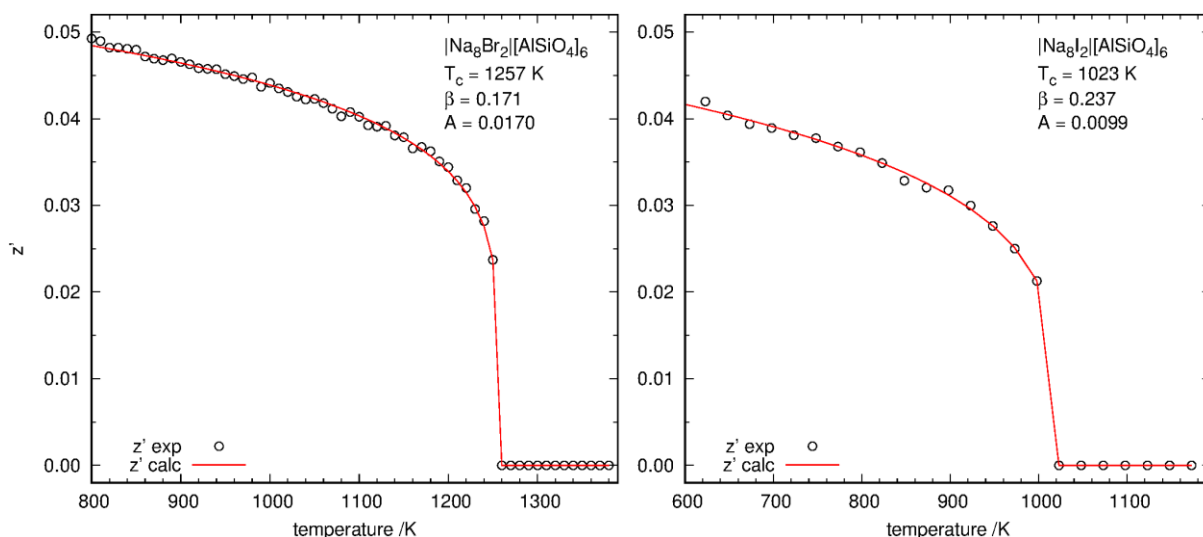


Figure 11: Fittings (red line) of the experimentally obtained order parameter z' (black circles) close to the temperature of phase transition using the Landau theory. The values of z' after the determined critical temperature were set to 0.

Whereas the Na–O1 distances are increasing with higher temperatures, the Na–O2 distances are decreasing (Figure 12). No order is present in the Na–O1 bonds, which are spread over a small range (ca 10 pm at 300 K), whereas the Na–O2 bonds are distributed over a much larger range (ca. 35 pm at 300 K) and show a clear and distinct grouping very similar to the one observed in the tilt angles (above). Regarding the Na–O2 distances, structures with the same framework are ordered according to the sequence: The larger the template ion, the shorter the Na–O2 bond. The gallosilicate and alumogermanate compounds are overlapping.

Generally, the alkali or alkaline-earth cations incorporated in the sodalite cages, which are sodium cations for the phases reported here, are the main charge mediators between the (negatively charged) framework and templating anion, which must balance framework and template charges at all temperatures by keeping the necessary distances. As the framework expands with increasing temperature, the 6-ring windows as well as the β -cage diameters become larger. The charge-balancing can be described in the scope of the bond valence sum concept [79, 83, 84]. The strongest sodium-framework coupling is in the Na–O1 bonds, which is the largest contribution to the bond valence sum (BVS) of the sodium. The contribution of the Na–O2 bond to the BVS is much smaller due to longer bonds, but still relevant, and is strongly influenced by the tilting and the T–O bond lengths. The more of its BVS is provided by the framework, the less must be contributed by the template. This explains the inverse relation between the volumes of the template-tetrahedron and of the unit-cell described above. Calculated BVSs of the sodalite structures at ambient conditions are given in Table 3 and plotted against the onset temperature of decomposition in Figure 13. Some of them differ

significantly from the expected value of +1 for sodium and -1 for the halide ions, which may be due to the uncommon nature of bonding inside the sodalite cage. On average, the BVS seems to have a lower total amount with a higher decomposition onset of the compound which generally correlates with a smaller radius of the halide ion (compare chapter 3.3 Decomposition and water loss (TGA/DSC)).

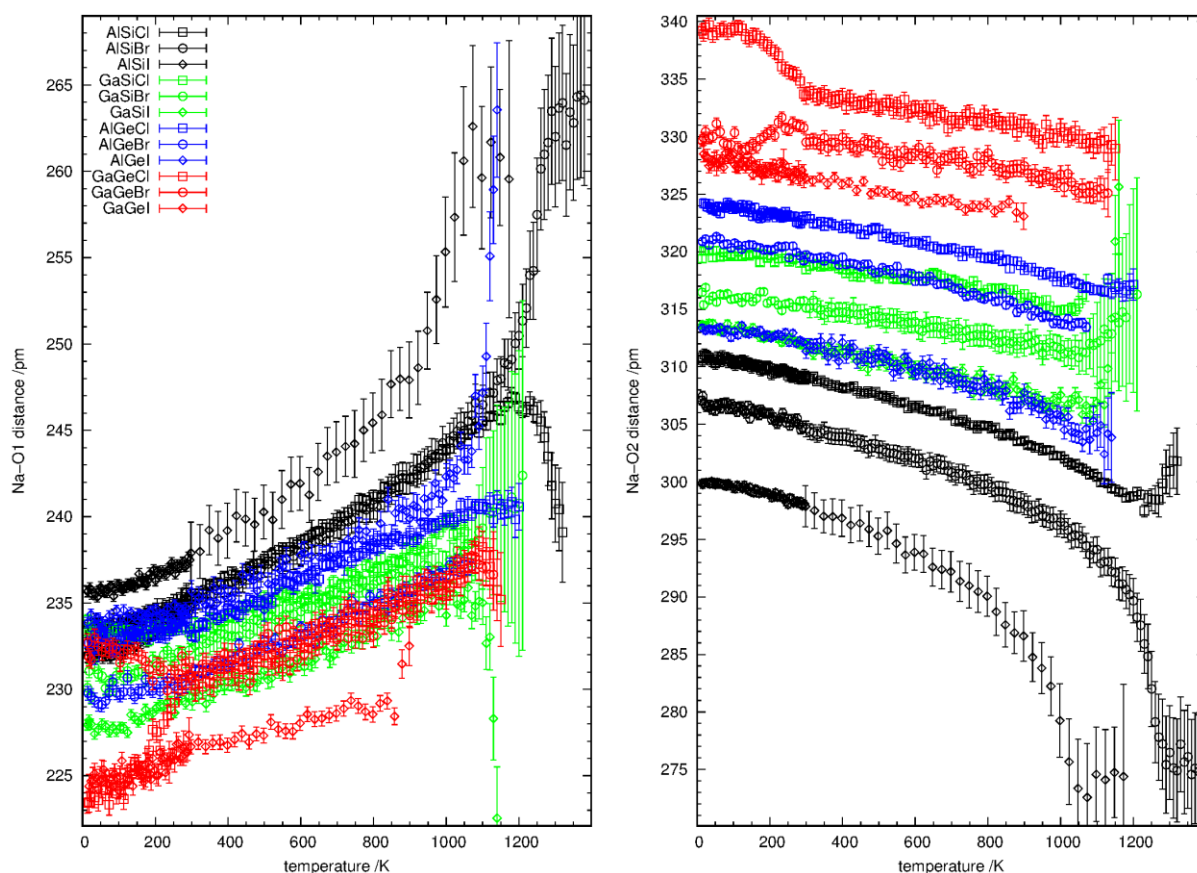


Figure 12: Temperature-dependent shorter Na-O1 (left) and longer Na-O2 distances (right). The different frameworks are indicated by color and the incorporated halide ion by type of symbol.

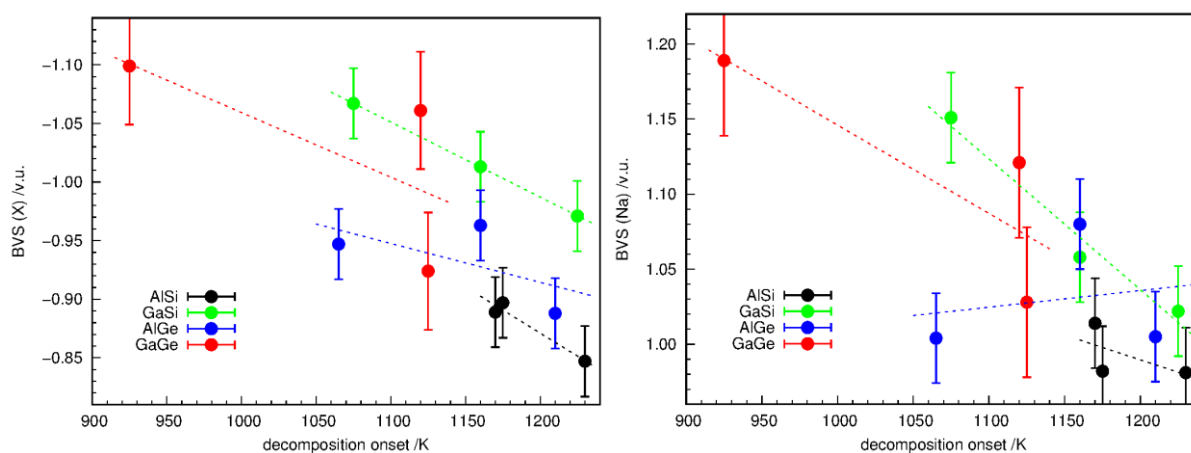


Figure 13: Bond valence sums of the halide ion X (left) and Na (right) against the decomposition temperature of the respective compound. The respective structures were obtained from X-ray diffraction experiments. Linear fits are included as guides to the eye.

Table 3: Selected bond lengths at ambient conditions and calculated bond valence sums.

Na–O /pm	Na–O2 /pm	Na–X /pm	BVS(X) /v.u.	BVS(Na) /v.u.
235.4(2)	309.2(2)	272.4(3)	-0.85(3)	0.98(3)
234.8(3)	304.6(3)	288.6(3)	-0.89(3)	1.01(3)
237.9(4)	297.9(6)	311.3(4)	-0.90(3)	0.98(3)
233.7(3)	318.9(3)	267.4(4)	-0.97(3)	1.02(3)
232.8(4)	315.1(4)	283.8(4)	-1.01(3)	1.06(3)
229.3(5)	311.8(5)	304.9(6)	-1.07(3)	1.15(3)
233.1(4)	323.1(4)	270.7(4)	-0.89(3)	1.00(3)
230.6(4)	319.7(4)	285.7(5)	-0.96(3)	1.08(3)
235.2(6)	311.4(6)	309.3(7)	-0.95(3)	1.00(3)
231.7(6)	333.1(12)	269.2(7)	-0.92(5)	1.03(5)
229.0(5)	330.9(11)	282.1(5)	-1.06(5)	1.12(5)
226.7(5)	326.4(5)	303.8(5)	-1.10(5)	1.19(5)

3.5 Thermal expansion

Refined lattice parameters were used for volume and TEC ($\alpha_{I,vol}$) calculation and the DEA modelling described in the following section. The determined unit-cell volumes and their TECs are given in Figure 14. The unit-cell volumes exhibit continuous expansion up to the decomposition temperatures, including the phase transition to the fully expanded structure in the cases of AlSiBr and AlSiI sodalite. In some cases, a change in the slope is visible, which causes distinct signals in the TEC, especially in the temperature range of water loss. However, for successful DEA modelling of all compounds, either a restriction of the fitted temperature ranges (temperature ranges used for the fitting are listed in Table 4) and/or additional Einstein contributions were necessary. Final parameters obtained from the modelling are collected in Table 5. The reduction of the TEC is most pronounced in the GaSiCl and AlGeCl sodalites, where it consists of two overlapping expansion/reduction effects. This clearly indicates that the change in TEC is caused by the loss of water inside the β -cages, as similar effects were observed in the TGA/DSC experiments. Nevertheless, the water content alone cannot explain why the effect is less pronounced in samples containing at least as much water as the AlGeCl sodalite, like AlGeBr or AlGeI, or why it is more pronounced in the GaSiCl sodalite compared to e.g., AlSiBr or GaSiBr. The extrapolated model volumes in temperature ranges excluded from the fitting (compare Table 4) are in all cases larger than the observed ones (for temperatures well below the decomposition temperature). The water loss is associated with a phase transformation due to a small reduction of N , the number of atoms in the structure. However, the model fit and

the experimental data proceed parallel, indicating just a change in M_0 with equivalent Debye and Einstein temperatures below and above the water loss temperature range. This means that the internal vibrational energies are not significantly influenced by small amounts of water incorporated in the β -cages.

A comparison of Einstein temperatures θ_{EI} (Table 5) of the different frameworks shows that the aluminosilicates exhibit the highest ones (2026 K to 6340 K) and the gallogermanates the lowest (434 K – 1307 K), while the other frameworks are in between (1128 K – 1800 K, except AlGeCl: 4540 K). With respect to the halide ion enclathrated within a certain framework, the Einstein temperature θ_{EI} is getting larger with increasing size of the halide ion. Exceptions are the GaSiBr and the AlGeCl sodalite. The first one shows a slightly smaller θ_{EI} than expected from the general trend, the latter one shows a much higher θ_{EI} than both other alumogermanates, but it was fitted with only two energy terms in total. No clear trend is found for θ_{E2} , which may be because it seems to be influenced by the effects of water loss to a higher degree. The Debye temperatures are also following no obvious trend. On the other hand, very high Einstein temperatures are very unlikely, the more as these high values are obtained for frameworks with the smallest tilt angles. That means that these frameworks are close to the phase transition described with a Landau term. It could not be ruled out that the fitting of at least a second Einstein temperature is influenced by the Landau type phase transition and therefore not describing the fundamental phonon behavior precisely which then might also influence the Debye temperature values.

Table 4: Temperature ranges of volume and TEC used for DEA-fitting.

Sample	range (cell volume) /K	range (TEC) /K
AlSiCl	18-870	18-870
AlSiBr	18-1070	18-1070
AlSiI	18-873	18-873
GaSiCl	18-560	18-560, 790-950
GaSiBr	18-500	18-500, 820-1010
GaSiI	18-560	18-560, 730-1000
AlGeCl	18-600	18-600, 1030-1170
AlGeBr	18-1060	18-1060
AlGeI	18-1000	18-1000
GaGeCl	18-600	18-600, 780-1030
GaGeBr	18-1100	18-1100
GaGeI	18-838	18-838

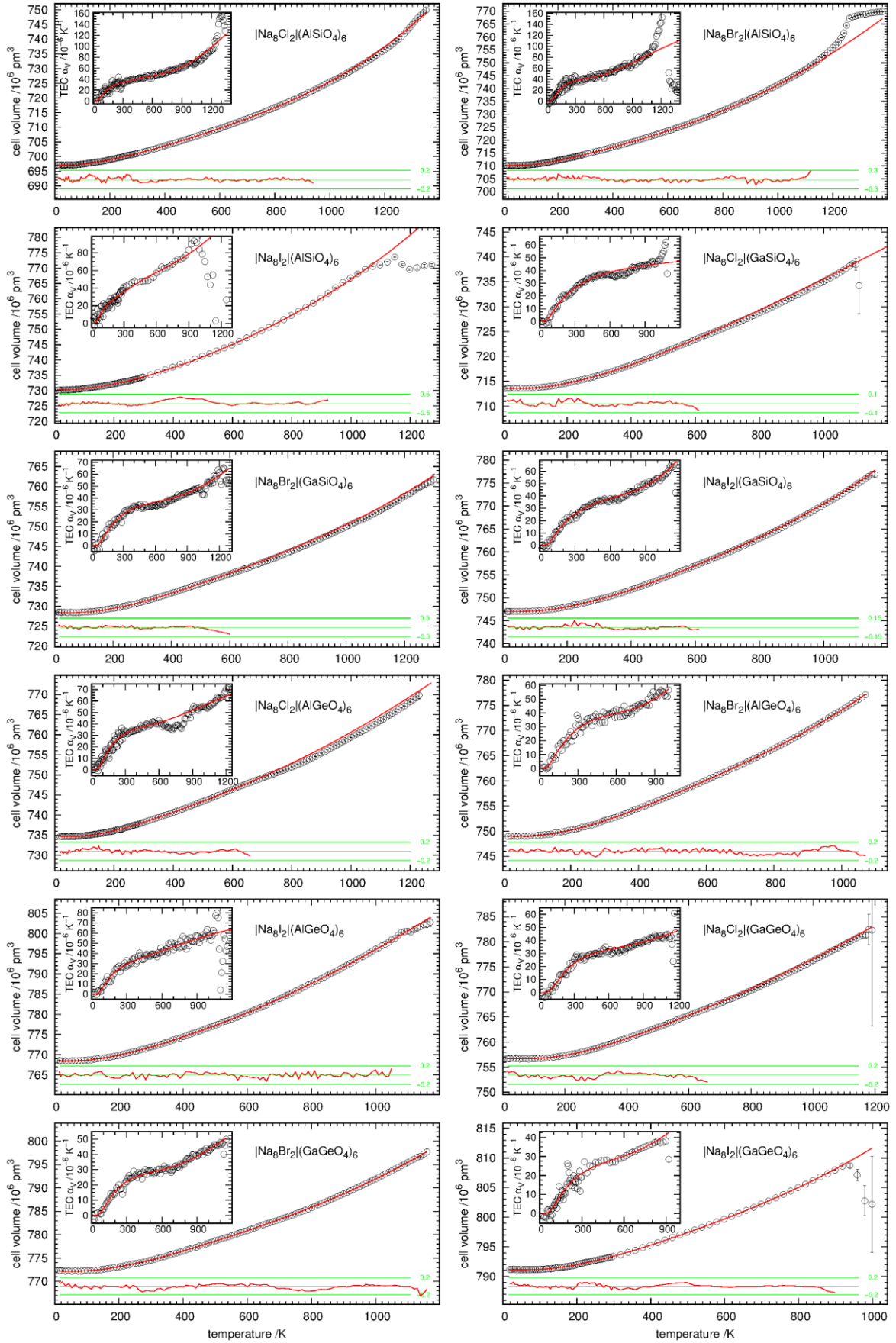


Figure 14: Cell volume (main panels) and TEC α_{vol} (insets) of all twelve sodalites with their DEA-models (red lines). The enlarged difference curve of the volume model (red line within green borders) ends 50 K after the last data point which was used to fit against.

Table 5: Parameters obtained in DEA-fittings.

Sample	$V_0 / 10^6$ pm ³	θ_{D1} /K	$k_{D1} / 10^{-12}$ GPa ⁻¹	θ_{D2} /K	$k_{D2} / 10^{-12}$ GPa ⁻¹	θ_{E1} /K	$k_{E1} / 10^{-12}$ GPa ⁻¹	θ_{E2} / K	$k_{E2} / 10^{-12}$ GPa ⁻¹
AlSiCl	697.08(5)	528(24)	14.5(7)			2026(94)	7.1(4)	7010(330)	164(8)
AlSiBr	710.13(5)	602(38)	18(2)			3270(210)	5.0(4)	4680(300)	49(4)
AlSiI	730.27(5)	473(41)	13(2)	2580(230)	21(2)	6340(560)	90(8)		
GaSiCl	713.56(5)	708(18)	11.7(3)			1386(35)	5.8(2)	4869(130)	3.4(2)
GaSiBr	728.40(5)	756(28)	12.7(5)			1166(43)	3.3(2)	6790(310)	64(4)
GaSiI	747.05(5)	833(17)	14.2(5)			1800(52)	4.7(2)	7830(230)	172(5)
AlGeCl	734.67(5)	720(28)	16.6(7)			4540(180)	25(1)		
AlGeBr	748.98(5)	700(32)	13.2(8)			1128(66)	4.6(3)	6990(420)	121(5)
AlGeI	768.47(5)	693(34)	15.6(8)			1793(87)	3.8(2)	3860(190)	17(2)
GaGeCl	756.66(5)	1055(39)	15.0(8)			434(21)	0.54(3)	6460(320)	30(4)
GaGeBr	772.20(5)	767(38)	11.1(6)			808(41)	2.1(2)	5660(290)	44(3)
GaGeI	791.13(5)	819(33)	12.2(5)			1307(52)	1.89(7)	5450(220)	50(3)

3.6 Force-field calculations

Lattice energy minimisation calculations gave the final lattice energy and compressibility of each compound which are presented in Table 6 and Figure 15. Phonon densities of states (PDOS) were also calculated and are shown in Figure 16. The lattice energy within a single framework-type is getting lower with larger incorporated halogenide ions and unit-cell volumes, respectively. When comparing different framework types, there is no direct relation to the volume. Instead, the energy gets higher with lower bond lengths differences between T¹-O and T²-O. Consequently, the framework types are ordered in the sequence Ga-Si < Al-Si < Ga-Ge < Al-Ge (Figure 15), as their bond lengths differences are approximately 20 pm (Ga-Si), 14 pm (Al-Si), 8 pm (Ga-Ge) and 0 pm (Al-Ge).

Table 6: Results from the force-field calculations with GULP for each compound.

Sample	lattice energy /eV	compressibility /GPa ⁻¹
AlSiCl	-1373.67	0.0140
AlSiBr	-1372.58	0.0122
AlSiI	-1370.93	0.0105
GaSiCl	-1366.06	0.0148
GaSiBr	-1365.33	0.0133
GaSiI	-1363.67	0.0115
AlGeCl	-1389.99	0.0152
AlGeBr	-1389.46	0.0138
AlGeI	-1387.82	0.0118
GaGeCl	-1382.10	0.0160
GaGeBr	-1381.47	0.0143
GaGeI	-1380.19	0.0127

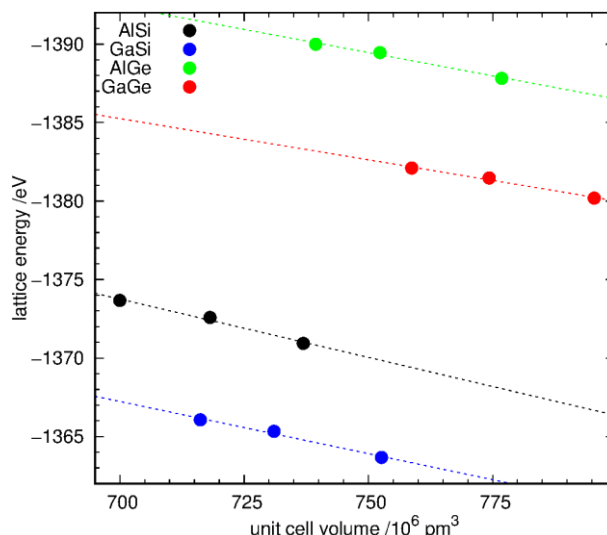


Figure 15: Lattice energy of the sodalites against the volume of their unit cells. Linear fits are given as guides to the eye.

The PDOS (Figure 16) of sodalites with the same framework atoms possess a similar shape. The most obvious difference is that with a larger incorporated halide ion, the frequency of the phonons with the lowest frequencies are shifted to even lower values. The frequencies with the highest number of phonons are located around 200 cm^{-1} for the different framework types and the second highest maximum above 800 cm^{-1} . In every spectrum a gap is found in front of the group with the second maximum, which is very narrow for the aluminosilicates and becomes wider the larger the framework is. The gallosilicate and alumogermanate sodalites show a second smaller gap around 550 cm^{-1} . As was explained in the introduction (1.2 The Debye-Einstein-anharmonicity model), the shape of the PDOS can be described using Einstein and Debye frequencies, ω_E or ω_D , respectively. The appearance of the sodalites PDOS justifies the application of multiple parameters, as they cannot be well approximated by a single Einstein or Debye frequency. While the vibrations of the aluminosilicates are almost a single continuum, larger gaps in the PDOS for other frameworks hint to the need of additional parameters. The PDOS of the gallosilicate and alumogermanate sodalites show two gaps between one larger and two smaller groups of frequencies which could be well described with one Debye and two Einstein frequencies, as was done in most cases when fitting the thermal expansion of the sodalites (see chapter 3.5 Thermal expansion). Furthermore, the similar appearance of the vibrations for the compounds with the same framework atoms would suggest that they can be described with a similar model, where the Debye and Einstein temperatures are only changing depending on mass and size of the incorporated halide anion. However, this was found not to be the case and the number of used Debye and Einstein temperatures to obtain an excellent fit of the thermal expansion does not match the regularities observed in the calculated PDOS.

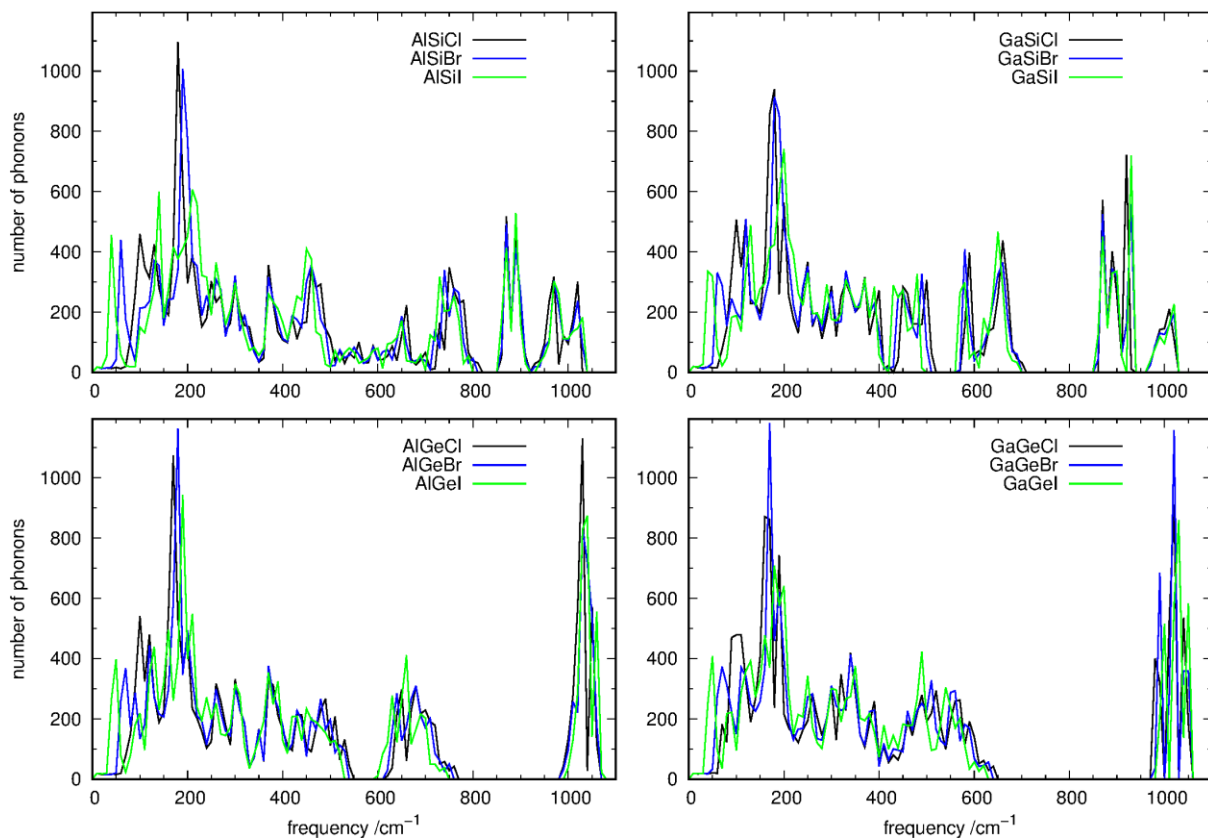


Figure 16: Phonon density of states (PDOS) of the alumosilicate (top left), gallosilicate (top right), alumogermanate (bottom left) and gallogermanate (bottom right) sodalites. The colors are according to the template ion chloride (black), bromide (blue) or iodide (green).

3.7 Discussion: The Lindemann criterion

The temperature-dependent behavior of the average structure of the sodalites has been investigated and no indications for unknown phase transitions were observed. No correlation between the Debye and Einstein temperatures from DEA modelling of the thermal expansion and the appearance of the calculated PDOS (*GULP*, $P\bar{4}3n$) was found. The PDOS and lattice energies of the structures show no unexpected behavior for the compounds but would hint to a simple relation between lattice vibrations and composition. The decomposition temperatures of the sodalites are expected to show some correlation with their structural parameters, but a clear correlation with observed bond lengths, other structural parameters or with the BVSs cannot be deduced from the collected data presented above. However, Lindemann proposed a criterion [123] to connect the melting temperature of a material, T_m , with the average root mean square displacement, u_{iso} , of the atoms: Melting occurs, if u exceeds n times (0.2 to 0.3) the lattice parameter.

$$\text{at } T_m: u_{iso} > n \cdot a \quad (11)$$

This simple criterion connects a structural parameter with a dynamic one. Shelimova and Plachkova [124] cite Sirota (N.N. Sirota and S.N. Chizhevskaya *Fizika i fiziko-khimicheskii analisis* 1957 30(1) 175; not available to the author) and provide the following relation between the Debye temperature θ_D^L (the superscript L denotes a Debye temperature determined by this Lindemann formula), Lindemann constant K_L , melting temperature T_M , and structural parameters (average atomic mass \bar{A} and average atomic distance $V^{2/3}$):

$$\theta_D^L = K_L \sqrt{\frac{T_M}{\bar{A} \cdot V^{2/3}}} = K_L Y \quad (12)$$

This formula is applied to the compounds here using the following modifications: Instead of T_M the onset temperature of the sodalite decomposition determined in the TG/DTA experiments, T_D , is used and instead of a single Debye temperature the geometrical average of the determined Debye and Einstein temperatures in the DEA fits, $\theta_{average}$, is used to obtain a reasonable average description of the phonon density of states. Then the formula

$$\theta_{average} = K_L \sqrt{\frac{T_D}{\bar{A} \cdot V^{2/3}}} = K_L Y \quad (13)$$

can be used to determine the Lindemann constants by the slopes ($\theta_{average}/Y$) (Table 7) and a plot of $\theta_{average}$ versus Y (Figure 17) should group the compounds on straight lines through the origin.

Table 7: The sodalites in increasing order of K_L . The AlGeCl sodalite could either be attributed to group 1 or 2, the first K_L average value for group 1 and group 2 is given with AlGeCl included in group 1, the second one with AlGeCl in group 2.

SOD	Y / ($10^{10} \text{ K}^{0.5} / \text{m}$)	$\theta_{average} / \text{K}$	$K_L / (\text{K}^{0.5} \text{ m})$	Group	Average $K_L / (\text{K}^{0.5} \text{ m})$
GaSiCl	437.2(3)	1684(43)	3.9(1)	1	3.94(8) / 4.01(4)
AlSiCl	497.2(3)	1957(91)	3.9(2)	1	
GaGeCl	356.9(3)	1435(64)	4.0(2)	1	
AlGeCl	425.6(3)	1808(71)	4.3(2)	1/2	4.6(2) / 4.61(8)
GaGeBr	342.8(3)	1519(77)	4.4(3)	2	
AlGeBr	391.6(3)	1767(96)	4.5(3)	2	
GaSiBr	397.0(3)	1816(72)	4.6(2)	2	
AlSiI	428.9(3)	1978(174)	4.6(5)	2	
AlSiBr	449.8(3)	2096(134)	4.7(3)	2	
AlGeI	344.5(3)	1686(83)	4.9(3)	2	
GaSiI	352.5(3)	2273(59)	6.5(2)	3	6.5(2)
GaGeI	272.9(3)	1800(72)	6.6(3)	3	

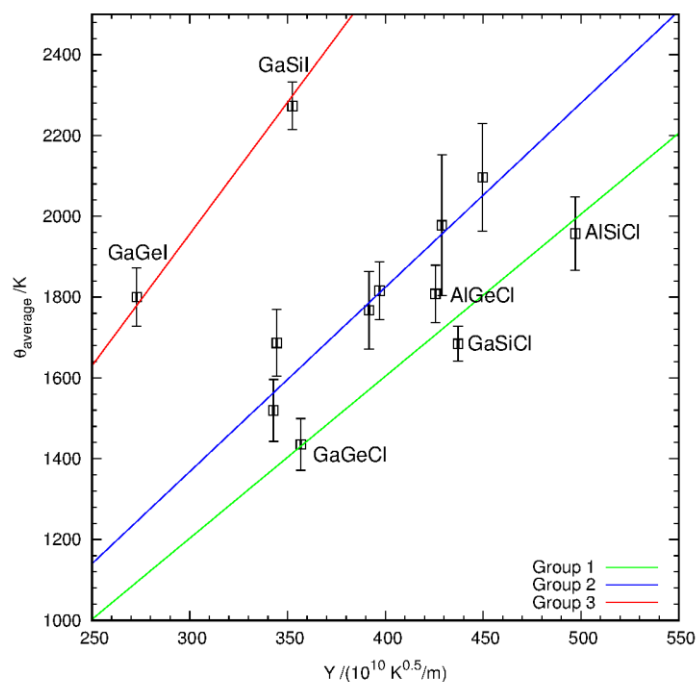


Figure 17: Plot of Y vs $\theta_{average}$. The linear equations for the three groups are given by the lines. AlGeCl is included in group 2.

An ordering of the compounds in three distinct groups becomes visible. The first group includes the sodalites containing Cl. AlGeCl seems to be a borderline case, but the standard deviation of the average K_L is smaller when it is attributed to group 2 instead of group 1. Group 3 includes GaGel and GaSiI, the first one being the largest of all sodalites considered here, the second one is very large and shows the biggest difference in T^1-O and T^2-O bond lengths. The AlGeI sodalite is slightly larger than the GaSiI sodalite but has almost identical T^1-O and T^2-O distances and can clearly be attributed to group 2, in which all other sodalites can be found. No correlations between selected bond lengths or other parameters, which are not included in the equation given above, and the Lindemann constants could be found. The sodalites with the same K_L show the same interplay between the phonon system and Y . This may give the possibility to determine the decomposition temperature of a given sodalite theoretically, if it is known to which group it belongs. For the first time, such a distinct correlation was found in these structures. However, all examined sodalites are isostructural with respect to their average structure determined from X-ray diffraction, and the underlying reason for this grouping of the compounds may originate from local deviations from the average structure. Thus, further experiments and computational methods were carried out to elucidate this correlation, which allow to analyze the local structure (total scattering) or are not restricted by the symmetry of space group $P\bar{4}3n$ as the force field used in *GULP*, which was fitted to the average structures (AIMD calculations in space group *P1*).

3.8 Ambient temperature total scattering, *ab-initio* MD calculations and 3D-BVS

The PDFs obtained from total scattering experiments collected at ambient conditions at beamline P21.1 (DESY, Hamburg) all show clear signals up to distances of multiple cell lengths (more than 4.0 nm) and all visible signals can be calculated in a refinement of a single unit-cell including symmetry (PDF-Rietveld refinement) as is done in (Bragg-)Rietveld refinements of XRD data. Small box refinements with models which are not constrained to symmetry (single unit cell in space group *P1*) or supercells of the unit cells did not give consistent or physically meaningful results. This indicates that data of even higher quality would be needed to gather precise information about the local structure, as was done using PDFs from neutron diffraction data of the AlSiI sodalite [29]. The PDF-Rietveld refinements could be improved further by using symmetrically constrained anisotropic displacement parameters (ADPs) for the Na and O atoms, which led to a better description of signal intensity and shape of the measured PDFs. The measured and calculated PDFs of these refinements are shown in Figure 18. The obtained average structures are in general agreement with those obtained from XRD refinements (see appendix). Selected bond lengths and bond valence sums of the structures are shown in Table 8. Significant deviations from expected values are present in the T–O bond lengths of the GaGeCl and GaGeBr sodalites, where they are by more than 1 pm longer or shorter than in the other listed structures. Similar results were obtained from the in-house XRD experiments and may be caused by the low scattering power of the oxygen atoms compared to the neighboring gallium and germanium and their equal number of electrons. In all alumosilicate structures, the refined Al–O bonds are shorter and the Si–O bonds longer than expected, but with their mean values fitting to expectations. This was not observed in the XRD experiments, but again seems to be an effect of the isoelectric tetrahedral ions.

Table 8: Lattice parameter (LP), selected bond lengths and BVS from PDF-Rietveld refinements.

Sample	LP	Na–X	Na–O1	Na–O2	T ¹ –O	T ² –O	BVS (X)	BVS (Na)
	/pm	/pm	/pm	/pm	/pm	/pm	/v.u.	/v.u.
AlSiCl	887.59(1)	274.0(1)	233.9(2)	308.5(2)	171.4(2)	165.1(2)	-0.81(2)	1.00(2)
AlSiBr	893.12(1)	288.4(1)	233.9(2)	304.2(2)	169.9(2)	166.7(1)	-0.90(2)	0.95(2)
AlSiI	901.21(1)	310.9(1)	233.5(2)	297.9(3)	171.7(2)	165.8(2)	-0.91(2)	0.91(2)
GaSiCl	893.88(1)	271.6(1)	229.8(1)	319.5(2)	182.4(1)	161.9(1)	-0.87(2)	1.07(2)
GaSiBr	900.31(1)	284.1(1)	232.1(1)	317.2(2)	182.2(1)	160.8(1)	-1.01(2)	0.97(2)
GaSiI	907.39(1)	305.5(1)	230.5(2)	310.8(2)	182.1(1)	161.7(1)	-1.05(2)	0.95(2)
AlGeCl	903.50(1)	273.4(1)	231.2(2)	322.5(2)	174.7(1)	174.3(1)	-0.83(2)	1.03(2)
AlGeBr	910.18(1)	287.5(1)	231.3(1)	319.6(2)	174.9(1)	174.3(1)	-0.92(2)	0.97(2)
AlGeI	918.55(1)	309.2(1)	230.6(2)	314.0(2)	175.2(2)	174.8(2)	-0.95(2)	0.93(2)
GaGeCl	911.55(1)	271.8(1)	229.3(2)	329.3(3)	178.4(2)	178.3(2)	-0.86(2)	1.07(2)
GaGeBr	916.79(1)	285.5(2)	227.7(2)	328.3(3)	184.0(2)	173.1(2)	-0.97(2)	1.04(2)
GaGeI	925.47(1)	306.4(2)	228.1(2)	322.9(3)	181.7(3)	175.1(2)	-1.02(2)	0.97(2)

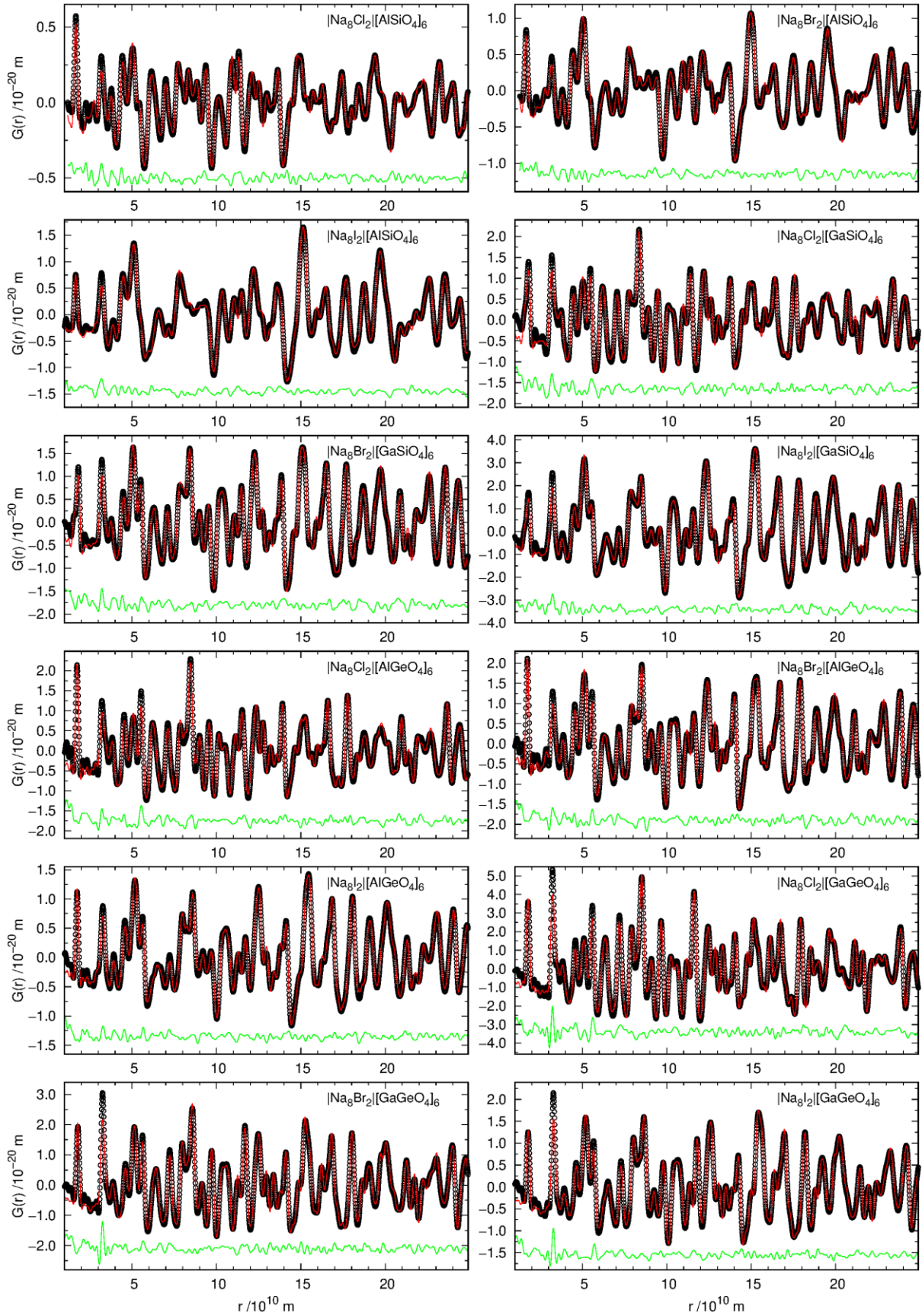


Figure 18: PDFs of all sodalites at ambient conditions as measured (black) and calculated (red) together with the difference curve (green).

Some of the calculated BVSs [79, 83, 84] (see Table 8) deviate from the theoretically expected absolute value of 1 valence unit (v.u.) by up to 0.19 v.u., which was also observed using in-house XRD (compare Table 3). The BVSs from PDF calculations reveal a distinct trend, where a larger incorporated halogenide within the same framework leads to a larger absolute value of the valence sum for the halogenide (X) and to a smaller absolute value for the sodium (Na). This can also be seen when the BVSs are plotted against the decomposition temperatures of the compounds (Figure 19). If both absolute values are added up, the gallosilicate and gallogermanate compounds come to a sum close to 2.00 v.u. (between 1.93 v.u. and 2.01 v.u.), while for the alumosilicate and alumogermanate compounds this results in a value below 1.90 v.u. in every case (between 1.81 v.u. and 1.88 v.u.). It is noteworthy that the slope of the linear fits for the BVSs of Na is of opposite sign compared to the BVSs of Na calculated from the average structures which were determined by X-ray experiments (3.4 Thermal behavior of the average sodalite structure, Figure 13).

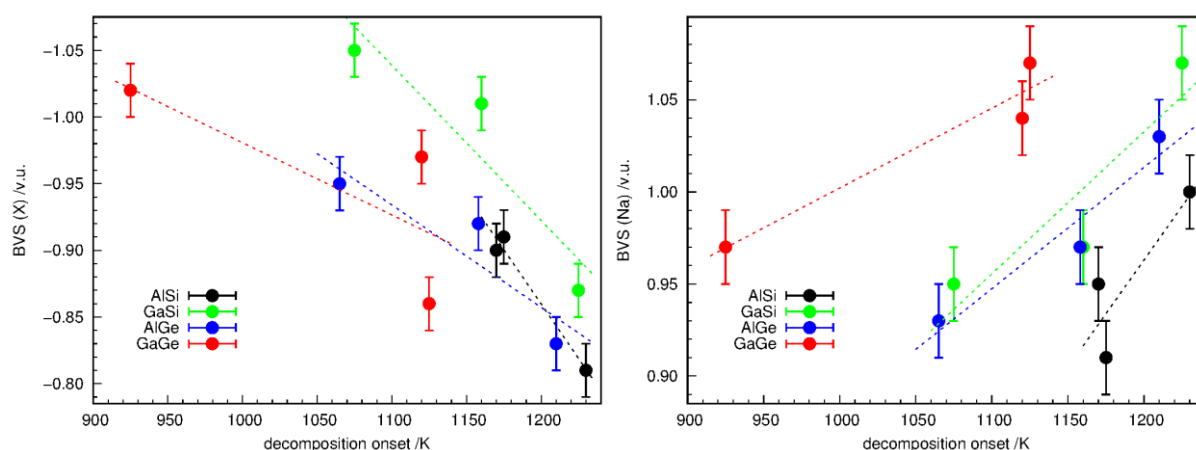


Figure 19: BVSs from structures determined by PDF-Rietveld refinement of the halide ion X (left) and Na (right) against the decomposition temperature of the respective compound. The respective structures were obtained from X-ray diffraction experiments. Linear fits are included as guides to the eye.

However, the refined ADPs of the structures (Figure 20) can provide deeper insight into the structure. The probability ellipsoids of all oxygen atoms possess a lentil-like shape, pointing outwards of the line between the two framework T atoms the respective oxygen is sitting in between. They are not pointing directly to the next Na atom in front of the ring, but approximately between this and one of the next neighboring framework oxygens. This movement of the oxygen atoms perpendicular to their bonds has also been observed in other zeolitic frameworks or quartz and explains the observed shortening of the bonds with higher temperatures when they are calculated from averaged atomic positions [39, 122, 125]. In most of the structures, the ADPs of the Na atoms are close to spherical showing no significant orientation in any direction. Nevertheless, there are two types of exceptions to this: First, in

every iodide-containing sodalite cage, the ellipsoid of sodium is elongated into the direction of the iodide and the center of the six-ring. Second, in the GaGeCl sodalite, the ellipsoid is flattened in this direction.

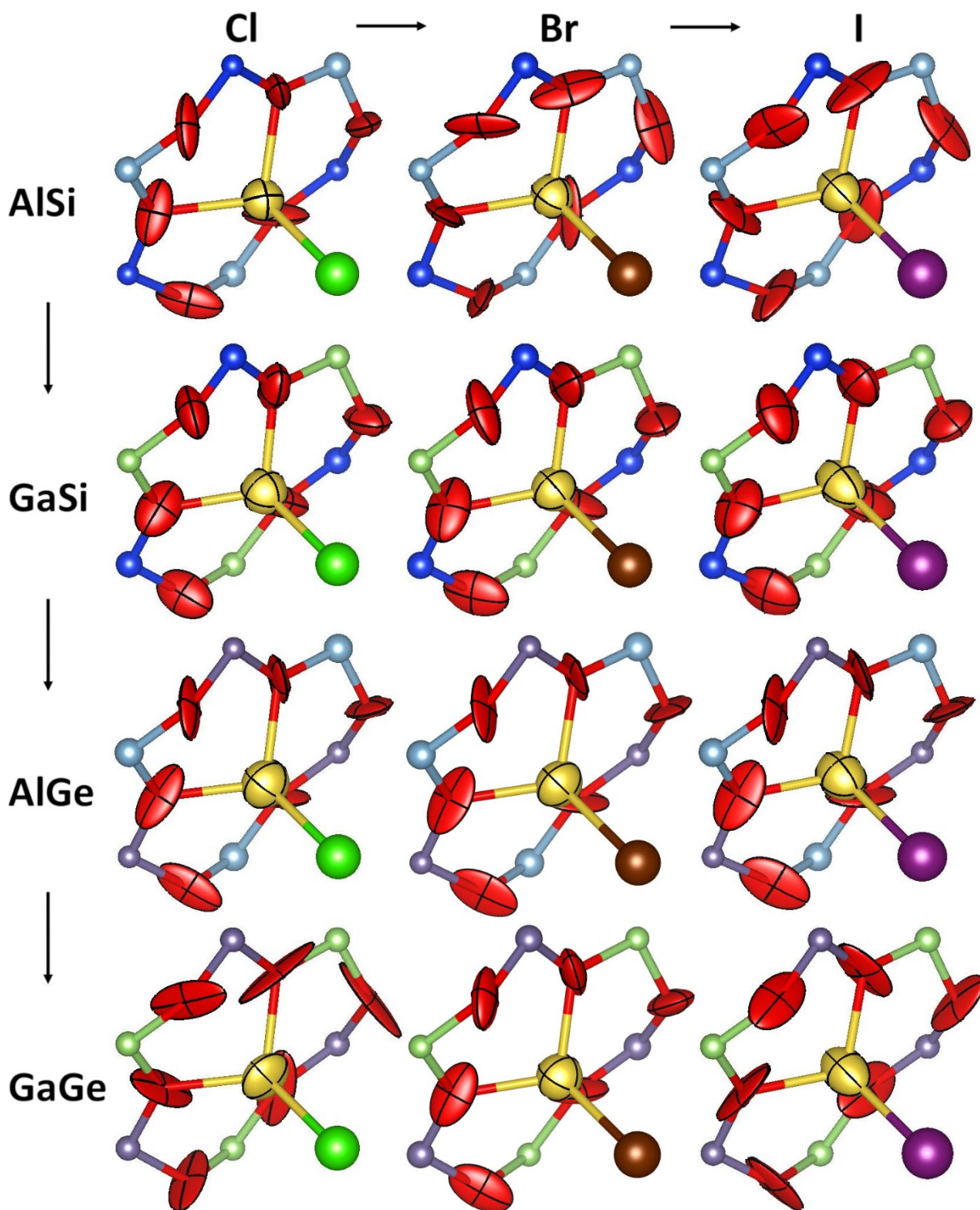


Figure 20: Displacement parameters of Na and O obtained from PDF calculations in the different sodalites as ellipsoids (99 % probability), ordered following framework (vertical) and template (horizontal). The atoms are colored according to their types: aluminum (light blue), silicon (blue), gallium (grey), germanium (light green), oxygen (red), sodium (yellow), chloride (green), bromide (brown), iodide (purple).

To confirm this observation with another method, AIMD calculations at 300 K without symmetry constraints were conducted for all twelve structures and thermal displacement parameters for sodium and the halide anions derived from the resulting atomic positions at different time steps. No atom followed a spherical distribution and especially the Na atoms were strongly deviating. A relation between the shape of the displacement and composition of the structure could not be found. Nevertheless, the equivalent isotropic displacement parameters show some noteworthy features (see Figure 21 and Table 9). Compared to the ones obtained from PDF calculations, they are all smaller by a factor of 25(9) on average. This may suggest that the thermal movement only plays a minor role, and the ADPs from PDF calculations contain significant structural deviations from the average structure. Additionally, in most frameworks the halide ion with the highest thermal displacement is bromide and not the lighter chloride, as it would be expected. This is also the case for the sodium atoms in the respective structures. The reason may be a lower structural displacement in the bromide sodalites compared to chloride and iodide, fitting to the spherical ADPs obtained from PDF calculations. The AlGeI sodalite is the exception in both cases, showing quite large displacement parameters for iodide and sodium.

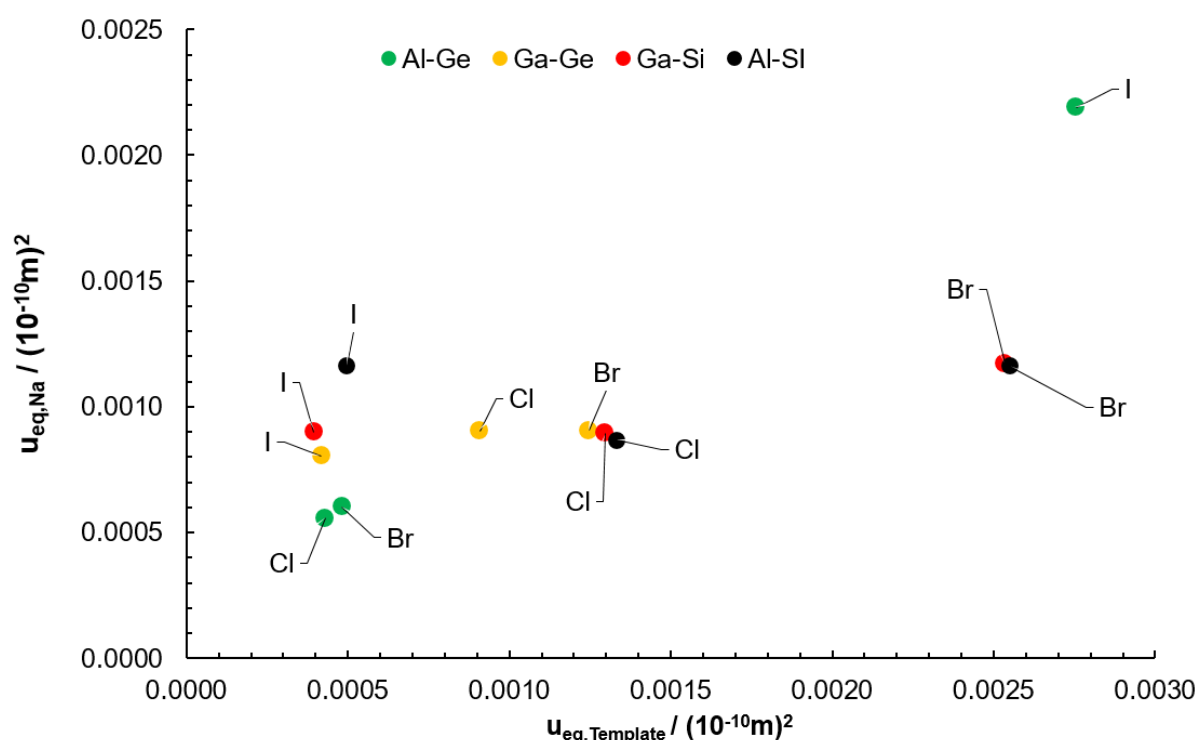


Figure 21: Equivalent displacement parameters of sodium and the respective halide ion in the sodalite structures from the atomic positions obtained in MD calculations.

Table 9: Equivalent displacement parameters of sodium determined in PDF calculations and from the atomic positions obtained in AIMD calculations.

Sodium		
Compound	$U_{\text{eq,PDF}}/(10^{-10} \text{ m})^2$	$U_{\text{eq,MD}}/(10^{-10} \text{ m})^2$
AlSi-Cl	0.01690	0.00087
AlSi-Br	0.01848	0.00116
AlSi-I	0.02066	0.00116
GaSi-Cl	0.02138	0.00090
GaSi-Br	0.02033	0.00117
GaSi-I	0.02495	0.00090
AlGe-Cl	0.02431	0.00056
AlGe-Br	0.02193	0.00060
AlGe-I	0.02595	0.00219
GaGe-Cl	0.02358	0.00090
GaGe-Br	0.02159	0.00091
GaGe-I	0.02596	0.00081

Driven by the observation of the different forms of the Na displacement ellipsoids in PDF calculations and the results in AIMD calculations, the respective structures were refined again, allowing deviation from the average structure in selected cases. The original $8e$ Na position was split into multiple partially occupied positions with a single isotropic displacement parameter to allow and account for the displacement. In the case of the iodide sodalites, the sodium was placed on two $8e$ positions with a fixed occupancy of 0.75 and 0.25 for the site closer to the framework and to the halogenide, respectively. For the GaGeCl sodalite, the sodium was placed on one $24i$ position with an occupancy of $\frac{1}{3}$. Refinements of these structures against the PDFs yielded stable atomic positions, suggesting that the structures of these 5 compounds indeed can be described as deviations from the average structure with one fully occupied $8e$ site. Consequently, one could distinguish three local structures defined by the position the Na atom occupies, which are all present in the three gallogermanate sodalites (see Figure 22). In the following, they will be called $P\bar{4}3n$ -avg. (the known average structure with the Na on a single $8e$ site, Figure 22 b), $P\bar{4}3n$ -2x $8e$ (the Na distributed on two partially occupied $8e$ sites, Figure 22 c) and $P\bar{4}3n$ - $24i$ (the Na on a partially occupied $24i$ site, Figure 22 a).

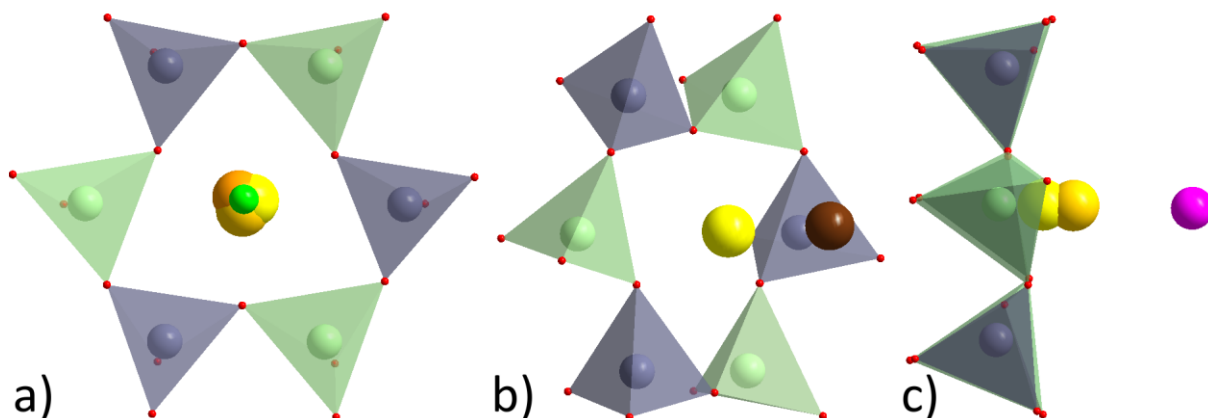


Figure 22: The structures of the gallogermanate sodalites at ambient temperature refined with a split Na position where possible. GaGeCl (a), GaGeBr (b) and GaGeI sodalite (c) (Na displayed in different shades of yellow/orange for clarity).

The bond valence sums of the average structures (see above) showed significant deviations from the expected values, but a three-dimensional representation of the BVS may be correlated to the found local deviations. Consequently, the hypothetical BVS for Na in the twelve sodalite structures at 300 K was calculated for every position of a 3-dimensional grid. Figure 23 shows the distribution of all voxels with a central BVS between 0.9 v.u. and 1.1 v.u. in the plane of one 6-ring of the framework. These positions were interpreted to be favorably occupied by a sodium atom. In general, structures containing the same halide ion show a similar shape for the favored positions. For the chloride compounds, they are distributed in a triangular shape which is oriented inverse to the one formed by the close oxygen atoms O1. For the bromide compounds, less positions are favored, and the shape becomes closer to a three-blade propeller, while for the iodide compounds these blades are narrower. The GaGeBr sodalite is an outlier, because the shape is closer to the triangular ones of the chloride structures, while the shape for the AlSiCl sodalite is a bit more propeller-like. Corresponding similarities for the favored positions can be seen in the viewing direction orthogonal to the 6-ring window, which is shown in Figure 24. The points with a BVS of ca. 1 are distributed quite evenly in front of the six-ring for the chloride structures. In the case of the bromide compounds, the shape is flatter, but close to the space diagonal some positions near to the 6-ring window and the halide ion become favorable. This is even more pronounced for the iodide compounds, where the tips of the “propeller blades” (compare Figure 23) are oriented slightly towards the iodide. In general, the appearances of the 3D-BVS are qualitatively agreeing with the observed ADPs and local structural deviations.

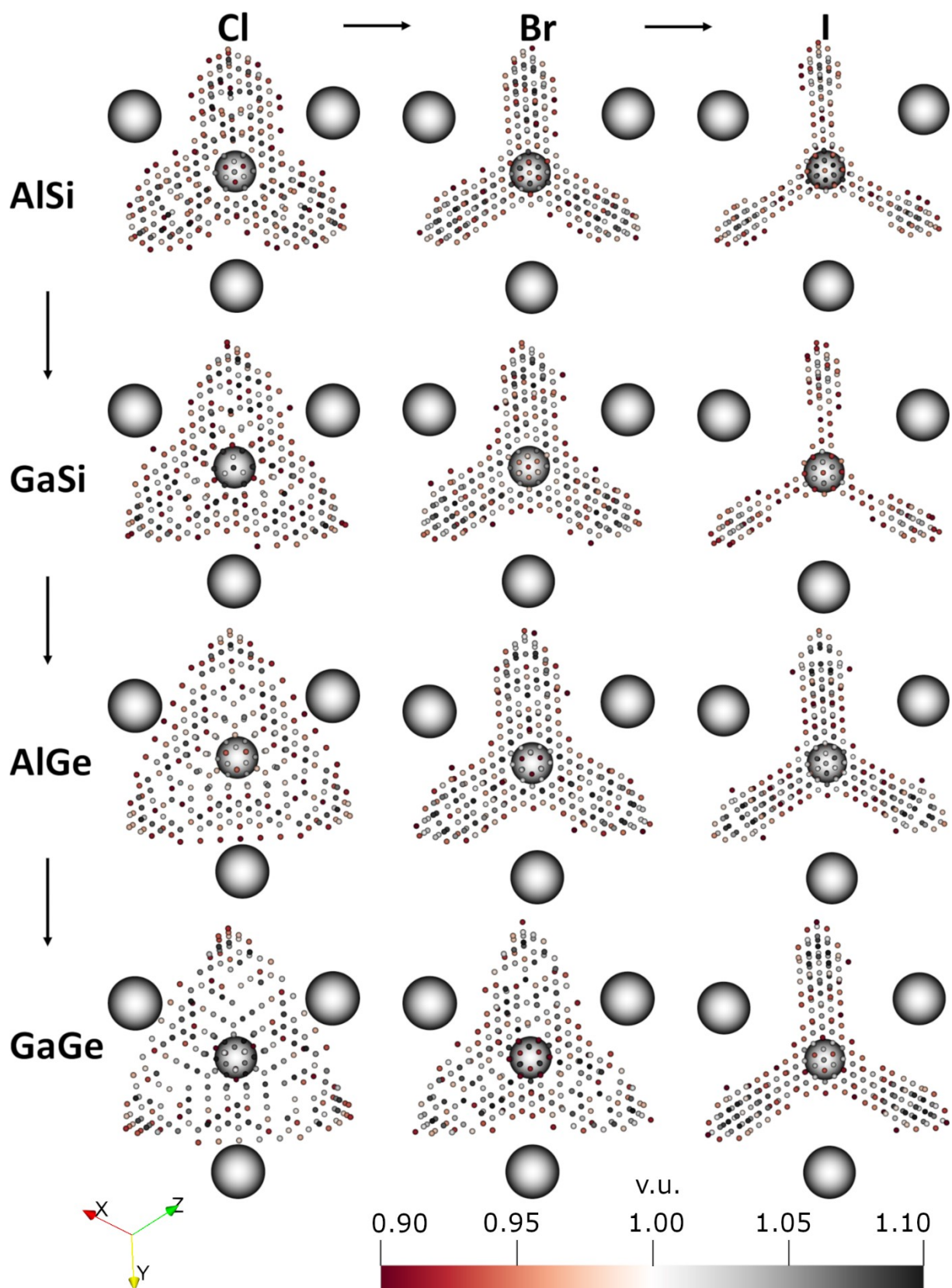


Figure 23: 3-dimensional BVS as seen from above the plane of the three O1 oxygen atoms. The central atom is the respective halide anion X. Only voxels with a BVS between 0.9 and 1.1 v.u. are shown.

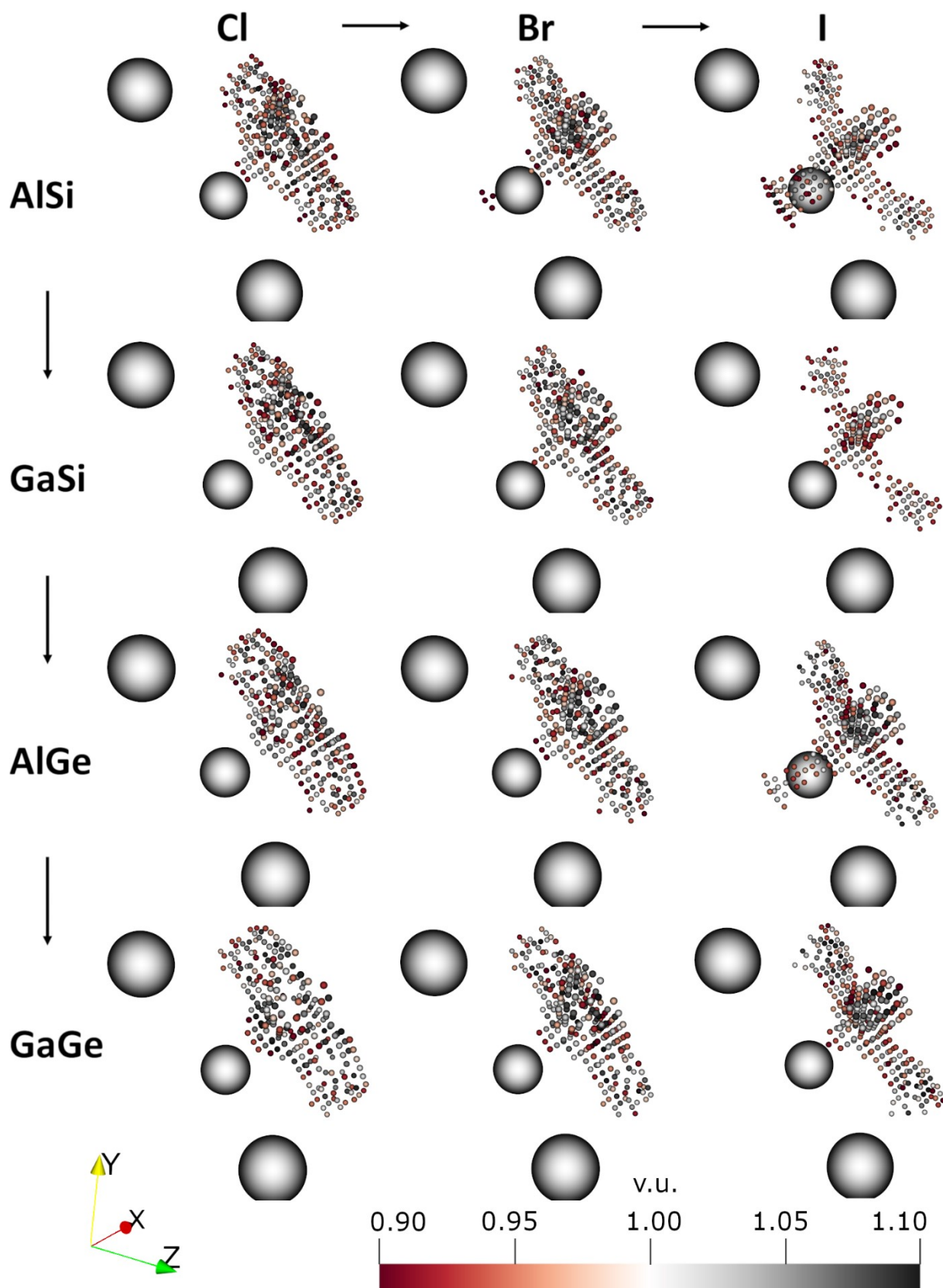


Figure 24: 3-dimensional BVS viewed orthogonal to the plane of the three O1 oxygen atoms. Only voxels with a BVS between 0.9 and 1.1 v.u. are shown.

3.9 Temperature-dependent total scattering

To examine and compare the temperature-dependent behavior of the above described three possible local structures of halide sodalites, total scattering experiments of the gallogermanate compounds between 100 K and 300 K were carried out at PETRA III (DESY, Beamline P02.1). Each dataset was refined using both models of the locally split Na position to further validate these structures (see Figure 25). In the case of the GaGeCl and the GaGeI sodalite the structures behave as could be expected after the examination of the ambient condition PDFs. For GaGeCl sodalite, the three coordinates of the $24i$ position are clearly separated and show no obvious tendency to merge to a single value (i.e., an $8e$ position) at either higher or lower temperatures. The higher data point scattering below 150 K is an effect of the capillary becoming loose during the measurement, thus wobbling and producing less intense scattering. For GaGeI sodalite, the two $8e$ sites are also clearly separated, one closer and one further away from the cage center compared to the average position determined using PXRD Rietveld refinements (compare chapter 3.4 Thermal behavior of the average sodalite structure). While the higher occupied $8e_1$ position is approaching the cage center with lower temperatures (and thus the respective Na–I bond becoming shorter), as would be expected, the less occupied $8e_2$ position is moving away. In a linear extrapolation, the two positions would meet only below 0 K. Applying the respective other split-position model ($P\bar{4}3n-24i$ for GaGeCl and $P\bar{4}3n-2x8e$ for GaGeI sodalite) as a test resulted in overlapping coordinates, closely resembling a fit using only one $8e$ site. This shows that only the model that can produce an electron distribution as seen for the anisotropic refined Na atoms gives additional information over the average model. For the GaGeBr sodalite, which is expected to be described correctly by the average structure, the $P\bar{4}3n-24i$ model surprisingly results in 3 separated Na coordinates. Nevertheless, above 200 K the refined position becomes less stable, resulting in higher scattering and swapping of the y and z coordinate. In general, a calculation using the 300 K PDF showed to produce different results, also nearly equivalent coordinates, depending on the applied starting values. Using the 100 K PDF, on the other hand, reliably led to the values shown in Figure 25 and the refinement of the GaGeBr dataset was consequently conducted from 100 K to 300 K. This behavior might be a hint for a phase transition from the average structure to the $P\bar{4}3n-2x8e$ structure happening close to 300 K. Additionally, the 3D-BVS of the GaGeBr sodalite as discussed above showed higher similarity to the GaGeCl sodalite than to the other bromide compounds, further indicating GaGeBr to be a borderline case close to ambient temperature.

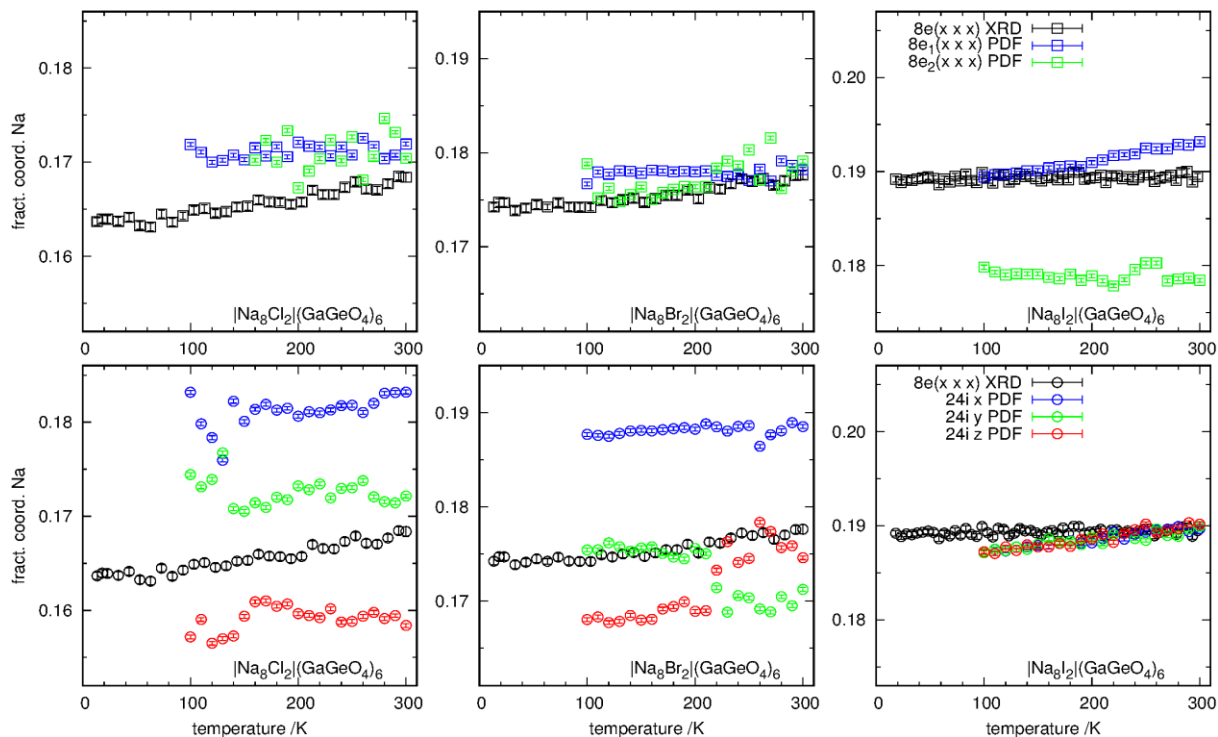


Figure 25: The Na position in the three gallogermanate sodalites. Colored symbols show the Na refined against the PDF using a split-position model (top row: $P\bar{4}3n-2x8e$, bottom row: $P\bar{4}3n-24i$), black symbols show the results of in-house PXR experiments ($P\bar{4}3n-avg.$).

3.10 Discussion: Deviations from the average structure

In the first chapters of this thesis, it was observed that macroscopic observables like decomposition temperature and thermal expansion behavior of simple halide sodalites cannot directly be linked to their chemical composition, geometry or the PDOS from force-field calculations where the field was fitted to the average structures. Nevertheless, the application of a modified Lindemann criterion orders them into three groups and the sodalites have been examined further by techniques which take the local structure into account or use a reduced symmetry compared to $P\bar{4}3n$ in the average structure.

AIMD calculations in space group $P1$ were not able to explain the different Lindemann constants of compounds, but they indicate only a minor contribution of the thermal displacement to the overall displacement parameters.

Total scattering experiments on the other hand showed diagonally elongated ADPs of Na for all iodide-containing structures and a flattened one for GaGeCl. This orders the sodalites into three groups, which are not completely identical to the “Lindemann groups”, but share some common features: First, at ambient temperature all bromide containing sodalites are part of the largest group, which seems to be described best by the average structure. Second, the gallogermanate sodalites have one member in each of the groups. The iodide-containing

structures were all found to be refinable with a model, where the Na is distributed on two partly occupied $8e$ sites, one further away and one closer to the iodide in the cage center. The Na in the GaGeCl sodalite could be refined on a $24i$ site with an occupancy of $\frac{1}{3}$. Low-temperature total scattering experiments of GaGeCl and GaGeI sodalite could be modelled with these structures. Surprisingly, for the GaGeBr sodalite, the $P\bar{4}3n-24i$ model also converges to three Na positions when applied. They are less stable with increasing temperature, therefore a phase transition close to 300 K could be possible. This would explain why this deviation of the Na was not observed in the total scattering experiment at ambient conditions. In fact, this raises the question if other halide-sodalites also undergo similar phase transitions. The 3D-BVS, which showed the favored Na positions in the GaGeBr structure to be like those in GaGeCl, would suggest GaSiCl and AlGeCl sodalite as candidates with similar positions. Phase transitions could be a reason why the compounds which were found to have a locally different distribution of the Na atoms are not strictly found in the respective Lindemann groups.

Furthermore, Robben et al. [29] examined the AlSiI sodalite with temperature dependent neutron total scattering experiments which allowed them to conduct Reverse Monte Carlo modelling. They did not report local deviations of the Na position but found a breaking of the symmetry at low temperatures, where the iodide leaves the center of the sodalite cage. One must keep in mind that the used experimental methods, the data evaluation and the choice of structural model have a high impact on the results of a study. For example, because the total scattering data shown in this thesis did not allow to fit models in space group $P1$ or use super cells, the halide ions could not leave their $2a$ sites at the cage center. As a result, effects from possible local deviations of the halide could be seen as local deviations of the Na, because the applied model only allowed these.

On a side note, McMullan et al. [39] observed an increasingly elongated ADP for Na^+ in natural AlSiCl at high temperatures close to decomposition, similar to the ADPs we observed in the iodide compounds. As the Na^+ ions are responsible for balancing the charge between framework and template, and thus their behavior should heavily influence the sodalites stability, the shape of the ADPs and the 3D-BVSs may be an indicator for why the iodide sodalites are generally less stable than their chloride and bromide counterparts.

4. Conclusion and outlook

In this thesis, various macroscopic and microscopic properties of the twelve halide sodalites $[\text{Na}_8\text{X}_2](\text{T}^1\text{T}^2\text{O}_4)_6$ ($\text{T}^1 = \text{Al, Ga}$; $\text{T}^2 = \text{Si, Ge}$; $\text{X} = \text{Cl, Br, I}$) were examined at ambient conditions, temperature-dependent and by computational methods. The temperature-dependent behavior of the average structures was refined between 18 K and the decomposition of the compounds. No unknown phase transitions could be found, not even in the low-temperature regime below ambient conditions, which was investigated less thoroughly in the past. The known $P\bar{4}3n$ to $Pm\bar{3}n$ phase transitions of AlSiBr and AlSiI sodalite were modelled using Landau theory and their transition temperatures found to be 1257(1) K and 1023(2) K, respectively. The phase transition of AlSiBr sodalite only begins after the onset of its decomposition. A microscopic property of solids, the phonon density of states, was calculated for the sodalites with a force-field, which was fitted to the determined average structures, and additionally approximated by fitting of the thermal expansion using the DEA-model. The Debye and Einstein temperatures from the DEA-fitting did not match the regularities observed in the calculated PDOS, leading to the conclusion that the true phonon structures cannot be calculated with a method which is inherently restricted to obey the symmetry ($P\bar{4}3n$) of the average structures like the used force-field. While no direct relation between the macroscopic properties chemical composition, decomposition temperature and the microscopic phonon structures from DEA modelling could be found, the sodalites could be ordered into three groups by a modified form of the Lindemann criterion. These compounds show a different interplay between their phonon system and their geometry and stability. Given that one knows the Lindemann constant of a sodalite and can approximate its phonon structure, either by using the DEA-model or maybe advanced computational methods without symmetry restrictions, it would be possible to determine its decomposition temperature theoretically.

Synchrotron total scattering data of the compounds were refined with the PDF-Rietveld approach, which allowed the refinement of anisotropic displacement parameters, but the models still obeyed the symmetry of $P\bar{4}3n$. Local deviations of some sodalites from the average structure are indicated by aspheric ADPs of Na for the iodide compounds and the GaGeCl sodalite. These structures could be refined with models distributing the Na ions on partially occupied positions, namely two $8e$ or one $24i$ position, depending on the shape of the ADPs. The models could also be refined temperature-dependent using total scattering data between 100 K and 300 K and are stable for the GaGeCl and GaGeI sodalite compounds. Hints for a possible phase transition from the average structure to a structure with two $8e$ positions for

GaGeBr sodalite close to 300 K were found. The compounds which could be fitted with a model different from the average structure were not completely identical to the ordering in the Lindemann groups, but in both cases at ambient temperatures all bromide sodalites were in one group and the gallogermanate sodalites had one member in each group. *Ab-initio* molecular dynamics calculations in space group $P1$ showed aspherical displacements for all sodalites, but their shape was not related to the ADPs from PDF-Rietveld refinements or any macroscopic properties. However, the calculated isotropic displacement parameters of sodium and the halide ions were on average smaller by a factor of 25(9) than the ones from PDF calculations. This indicates that the thermal displacement may play a minor role for these atoms and that large displacement parameters from refinements are indeed a result of microscopic structural displacements. Although BVSs calculated for Na^+ and I^- in the average structures deviated significantly from the expected values and showed a systematic behavior with respect to the chemistry of the compounds, three-dimensional visualizations of the hypothetical BVS of Na correlate with the local structures. They may suggest a phase transition below ambient temperature to a locally different structure for GaSiCl and AlGeCl sodalite.

The macroscopic properties of a compound are determined by its microscopic real structure [126]. Consequently, connections between the observed local deviations from the average structure, the Lindemann constants and the thermal stability of the halide sodalites were found in this study. The average structure is a useful description of solid materials but did not allow to make these connections. However, the DEA model proved to be a powerful tool, as it could be used to get insight into the phonon structure by modelling the thermal expansion using only the results from temperature-dependent refinements of the average structure.

Although it was possible to refine two models with Na positions which are different from the known average structure where aspheric ADPs were found, it is very likely that these models only approximate the real local structure in the respective sodalites. As they still had to obey the symmetry of $P\bar{4}3n$, they are probably also averaged to some degree. The available total scattering data did not allow to investigate deviations of the halide ions from the average local symmetry by placing them on a comparable partly occupied position or by refining anisotropic displacement parameters. Therefore, anharmonic behavior and symmetry breaking of the halide ions, as it was already reported for AlSiI sodalite at low temperatures, could have influenced the Na positions described in this study. To further elucidate the local structure in halide sodalites, temperature-dependent neutron total scattering experiments of high quality should be conducted in the future. These would enable to refine large supercell models with methods like

Reverse Monte Carlo modelling and might make it possible to differentiate between local deviations of the sodium and halide atoms from the average structure.

5. References

- [1] M. Wolpmann, L. Robben, T.M. Gelsing, Halide-sodalites: thermal expansion, decomposition and the Lindemann criterion, *Z. Kristallogr. - Cryst. Mater.* 237 (2022) 39-50. Doi:10.1515/zkri-2022-0004
- [2] M.T. Weller, Where zeolites and oxides merge: Semi-condensed tetrahedral frameworks, *J. Chem. Soc., Dalton Trans.* (23) (2000) 4227–4240. Doi:10.1039/b003800h
- [3] S.V. Krivovichev, Structural and topological complexity of zeolites: An information-theoretic analysis, *Microporous Mesoporous Mater.* 171 (2013) 223-229. Doi:10.1016/j.micromeso.2012.12.030
- [4] T. Thomson, A Chemical Analysis of Sodalite, a New Mineral from Greenland, *Med. Phys. J.* 26(152) (1811) 303-308.
- [5] F.M. Jaeger, On the constitution and the structure of ultramarine, *Trans. Faraday Soc.* 25 (1929) 320-345. Doi:10.1039/tf9292500320
- [6] L. Pauling, XXII. The Structure of Sodalite and Helvite, *Z. Kristallogr. - Cryst. Mater.* 74(1-6) (1930) 213–225. Doi:10.1524/zkri.1930.74.1.213
- [7] H. Petersen, L. Robben, T.M. Gelsing, On the nature of the phase transitions of aluminosilicate perrhenate sodalite, *Z. Kristallogr. - Cryst. Mater.* 235(6-7) (2020) 213-223. Doi:10.1515/zkri-2020-0027
- [8] L. Robben, M. Wolpmann, P. Bottke, H. Petersen, M. Šehović, T.M. Gelsing, Disordered but primitive gallosilicate hydro-sodalite: Structure and thermal behaviour of a framework with novel cation distribution, *Microporous Mesoporous Mater.* 256 (2018) 206–213. Doi:10.1016/j.micromeso.2017.08.019
- [9] H. Petersen, L. Robben, M. Šehović, T.M. Gelsing, Synthesis, temperature-dependent X-ray diffraction and Raman spectroscopic characterization of the sodalite to nosean phase-transformation of $[\text{Na}_{7.7(1)}(\text{MnO}_4)_{1.7(2)}(\text{H}_2\text{O})_{0.8(2)}][\text{AlSiO}_4]_6$, *Microporous Mesoporous Mater.* 242 (2017) 144–151. Doi:10.1016/j.micromeso.2017.01.019
- [10] I. Poltz, L. Robben, J.-C. Buhl, T.M. Gelsing, Synthesis, crystal structure and temperature-dependent properties of gallogermanate nitrite sodalite $[\text{Na}_8(\text{NO}_2)_2][\text{GaGeO}_4]_6$, *Microporous Mesoporous Mater.* 203 (2015) 100–105. Doi:10.1016/j.micromeso.2014.10.007
- [11] M. Šehović, L. Robben, T.M. Gelsing, Carbon dioxide uptake in nitrite-sodalite: reaction kinetics and template ordering of the carbonate-nosean formation, *Z. Kristallogr. - Cryst. Mater.* 230(4) (2015) 263-269. Doi:10.1515/zkri-2014-1815
- [12] L. Robben, T.M. Gelsing, Temperature-dependent framework–template interaction of $[\text{Na}_6(\text{H}_2\text{O})_8][\text{ZnPO}_4]_6$ sodalite, *J. Solid State Chem.* 207 (2013) 13–20. Doi:10.1016/j.jssc.2013.08.022
- [13] T.M. Gelsing, B.C. Schmidt, M.M. Murshed, Temperature dependent structural and spectroscopic studies of sodium gallosilicate nitrite sodalite, *Mater. Res. Bull.* 45(11) (2010) 1618–1624. Doi:10.1016/j.materresbull.2010.07.014

- [14] M.M. Murshed, A.J. Baer, T.M. Gesing, Isomorphous framework cation substitution in the aluminosilicate sodalites: synthesis, structural and spectroscopic studies of nitrite-containing phases, *Z. Kristallogr.* 223(9) (2008) 575-583. Doi:10.1524/zkri.2008.1018
- [15] M.M. Murshed, T.M. Gesing, Gallium substitution in the aluminosilicate framework: Synthesis and structural studies of hydro sodalites, *Z. Kristallogr.* 223(3/2008) (2008) 178-185. Doi:10.1524/zkri.2008.0015
- [16] T.M. Gesing, Structure and properties of tecto-gallosilicates II. Sodium chloride, bromide and iodide sodalites, *Z. Kristallogr.* 222(6) (2007) 289–296. Doi:10.1524/zkri.2007.222.6.289
- [17] M.M. Murshed, T.M. Gesing, Isomorphous gallium substitution in the aluminosilicate sodalite framework: Synthesis and structural studies of chloride and bromide containing phases, *Z. Kristallogr.* 222(7) (2007) 341–349. Doi:10.1524/zkri.2007.222.7.341
- [18] J.-C. Buhl, T.M. Gesing, T. Höfs, C.H. Rücher, Synthesis and crystal structure of gallosilicate- and aluminogermanate tetrahydroborate sodalites $\text{Na}_8[\text{GaSiO}_4]_6(\text{BH}_4)_2$ and $\text{Na}_8[\text{AlGeO}_4]_6(\text{BH}_4)_2$, *J. Solid State Chem.* 179(12) (2006) 3877–3882. Doi:10.1016/j.jssc.2006.08.031
- [19] J.-C. Buhl, T.M. Gesing, I. Kerkamm, C. Gurriss, Synthesis and crystal structure of cyanate sodalite $[\text{Na}_8(\text{OCN})_2][\text{Al}_6\text{Si}_6\text{O}_{24}]$, *Microporous Mesoporous Mater.* 65(2) (2003) 145–153. Doi:10.1016/j.micromeso.2003.07.004
- [20] T.M. Gesing, J.-C. Buhl, Crystal structure of sodium aluminosilicate cyanide, $\text{Na}_8[\text{AlSiO}_4]_6(\text{CN})_2$, *Z. Kristallogr. - New Cryst. Struct.* 218(3) (2003) 275. Doi:10.1524/ncrs.2003.218.3.275
- [21] T.M. Gesing, Structure and properties of tecto-gallosilicates. I. Hydrosodalites and their phase transitions, *Z. Kristallogr. - Cryst. Mater.* 215(9) (2000) 510-517. Doi:10.1524/zkri.2000.215.9.510
- [22] T.M. Gesing, J.-C. Buhl, Structure and spectroscopic properties of hydrogencarbonate containing aluminosilicate sodalite and cancrinite, *Z. Kristallogr. - Cryst. Mater.* 215(7) (2000) 413-418. Doi:10.1524/zkri.2000.215.7.413
- [23] T.M. Gesing, *Bildung, Strukturen, Eigenschaften und Phasenbeziehungen von Zinkarsenat-, Gallosilikat- und Aluminosilikat-Sodalithen, Cancriniten und verwandten Verbindungen*, Gottfried Wilhelm Leibnitz Universität Hannover, Hannover, 2000.
- [24] G.M. Johnson, P.J. Mead, M.T. Weller, Synthesis of a range of anion-containing gallium and germanium sodalites, *Microporous Mesoporous Mater.* 38(2-3) (2000) 445–460. Doi:10.1016/S1387-1811(00)00169-4
- [25] G.M. Johnson, P.J. Mead, M.T. Weller, Structural trends in the sodalite family, *Phys. Chem. Chem. Phys.* 1(15) (1999) 3709–3714. Doi:10.1039/a903373d
- [26] C.M. Braunbarth, P. Behrens, J. Felsche, Phase transitions and thermal behaviour of silica sodalites, *Solid State Ionics* 101 (1997) 1273-1277. Doi:10.1016/S0167-2738(97)00401-3
- [27] W. Depmeier, Phase transitions and modulated structures in aluminate sodalites, *J. Alloys Compd.* 188(19) (1992) 21-26. Doi:10.1016/0925-8388(92)90638-P

- [28] W. Depmeier, The Sodalite Family – A Simple but Versatile Framework Structure, *Rev. Mineral. Geochem.* 57(1) (2005) 203–240. Doi:10.2138/rmg.2005.57.7
- [29] L. Robben, I. Abrahams, M. Fischer, S. Hull, M.T. Dove, T.M. Gesing, Low-temperature anharmonicity and symmetry breaking in the sodalite $[\text{Na}_8\text{I}_2][\text{AlSiO}_4]_6$, *Z. Kristallogr. - Cryst. Mater.* 234(4) (2019) 219–228. Doi:10.1515/zkri-2018-2122
- [30] R.X. Fischer, W.H. Baur, Symmetry relationships of sodalite (SOD) – type crystal structures, *Z. Kristallogr.* 224(4) (2009) 185–197. Doi:10.1524/zkri.2009.1147
- [31] R.X. Fischer, W.H. Baur, Zeolite-Type Crystal Structures and their Chemistry. Framework Type Codes RON to STI, Springer-Verlag, Berlin, Heidelberg, 2009.
- [32] D. Taylor, The thermal expansion of the sodalite group of minerals, *Mineral. Mag. J. Mineral Soc.* 36(282) (1968) 761–769. Doi:10.1180/minmag.1968.036.282.02
- [33] C.M.B. Henderson, D. Taylor, The thermal expansion of synthetic aluminosilicate-sodalites, $\text{M}_8(\text{Al}_6\text{Si}_6\text{O}_{24})\text{X}_2$, *Phys. Chem. Miner.* 2(4) (1978) 337–347. Doi:10.1007/BF00307576
- [34] D. Taylor, C.M.B. Henderson, A computer model for the cubic sodalite structure, *Phys. Chem. Miner.* 2(4) (1978) 325–336. Doi:10.1007/BF00307575
- [35] D. Taylor, The Thermal Expansion Behaviour of the Framework Silicates, *Mineral. Mag.* 38(297) (1972) 593–604. Doi:10.1180/minmag.1972.038.297.08
- [36] I. Hassan, H.D. Grundy, The crystal structures of sodalite-group minerals, *Acta Crystallogr. Sect. B: Struct. Sci.* 40(1) (1984) 6–13. Doi:10.1107/S0108768184001683
- [37] W.M.V. Meier, H. Die Methode der Abstandsverfeinerung zur Bestimmung der Atomkoordinaten idealisierter Gerüststrukturen, *Z. Kristallogr.* 129(5-6) (1969) 411–423. Doi:doi:10.1524/zkri.1969.129.5-6.411
- [38] M.J. Dempsey, D. Taylor, Distance least squares modelling of the cubic sodalite structure and of the thermal expansion of $\text{Na}_8(\text{Al}_6\text{Si}_6\text{O}_{24})\text{I}_2$, *Phys. Chem. Miner.* 6(3) (1980) 197–208. Doi:10.1007/BF00309856
- [39] R.K. McMullan, S. Ghose, N. Haga, V. Schomaker, Sodalite, $\text{Na}_4\text{Si}_3\text{Al}_3\text{O}_{12}\text{Cl}$: Structure and ionic mobility at high temperatures by neutron diffraction, *Acta Crystallogr. Sect. B: Struct. Sci.* 52(4) (1996) 616–627. Doi:10.1107/S0108768196004132
- [40] I. Hassan, S.M. Antao, J.B. Parise, Sodalite: High-temperature structures obtained from synchrotron radiation and Rietveld refinements, *Am. Mineral.* 89(2-3) (2004) 359–364. Doi:10.2138/am-2004-2-315
- [41] R.S.P. King, S.E. Dann, M.R.J. Elsegood, P.F. Kelly, R.J. Mortimer, The Synthesis, Full Characterisation and Utilisation of Template-Free Silica Sodalite, a Novel Polymorph of Silica, *Chem. Eur. J.* 15(22) (2009) 5441–5443. Doi:10.1002/chem.200802551
- [42] D.M. Többsen, W. Depmeier, Superstructure of strontium chromate aluminate sodalite at low temperatures, *Z. Kristallogr. - Cryst. Mater.* 216(11) (2001) 586–590. Doi:10.1524/zkri.216.11.586.22483

- [43] D.M. Töbrens, W. Depmeier, The intermediate phase of strontium chromate aluminate sodalite, *Z. Kristallogr. - Cryst. Mater.* 216(12) (2001) 611-615. Doi:10.1524/zkri.216.12.611.22487
- [44] L. Leardini, A. Martucci, G. Cruciani, The unusual thermal expansion of pure silica sodalite probed by in situ time-resolved synchrotron powder diffraction, *Microporous Mesoporous Mater.* 151 (2012) 163-171. Doi:10.1016/j.micromeso.2011.10.042
- [45] W. Depmeier, Aluminate sodalites - A family with strained structures and ferroic phase transitions, *Phys. Chem. Miner.* 15(5) (1988) 419-426. Doi:10.1007/BF00311120
- [46] M. Wiebcke, P. Sieger, J. Felsche, G. Engelhardt, P. Behrens, J. Schefer, Sodium aluminogermanate hydroxosodalite hydrate $\text{Na}_{6+x}[\text{Al}_6\text{Ge}_6\text{O}_{24}](\text{OH})_x \cdot n\text{H}_2\text{O}$ ($x = 1.6$, $n = 3.0$): Synthesis, phase transitions and dynamical disorder of the hydrogen dihydroxide anion, H_3O_2^- , in the Cubic high-temperature form, *Z. Anorg. Allg. Chem.* 619(7) (1993) 1321-1329. Doi:10.1002/zaac.19936190728
- [47] S. Luger, J. Felsche, P. Fischer, Structure of hydroxysodalite $\text{Na}_8[\text{AlSiO}_4]_6(\text{OH})_2$, a powder neutron diffraction study at 8 K, *Acta Crystallogr. Sect. C: Cryst. Struct. Commun.* 43(1) (1987) 1-3. Doi:10.1107/S0108270187097233
- [48] J. Felsche, S. Luger, P. Fischer, Localization of water in hexasodium hexakis(aluminosilicate)-deuterium oxide (1/8), $\text{Na}_6[\text{AlSiO}_4]_6 \cdot 8\text{D}_2\text{O}$. A neutron powder diffraction Rietveld profile analysis at 10 K, *Acta Crystallogr. Sect. C: Cryst. Struct. Commun.* 43(5) (1987) 809-811. Doi:10.1107/S0108270187093983
- [49] W. Buehrer, J. Felsche, S. Luger, Hydrogen dynamics in hydro-sodalite $\text{Na}_8[\text{AlSiO}_4]_6(\text{OH})_2$ by inelastic and quasielastic neutron scattering, *J. Chem. Phys.* 87(4) (1987) 2316-2320. Doi:10.1063/1.453110
- [50] J. Felsche, S. Luger, Phases and thermal decomposition characteristics of hydro-sodalites $\text{Na}_{6+x}[\text{AlSiO}_4]_6(\text{OH})_x \cdot n\text{H}_2\text{O}$, *Thermochim. Acta* 118 (1987) 35-55. Doi:10.1016/0040-6031(87)80069-2
- [51] M. Wiebcke, G. Engelhardt, J. Felsche, P.B. Kempa, P. Sieger, J. Schefer, P. Fischer, Orientational disorder of the hydrogen dihydroxide anion, (O_2H_3^-) in sodium hydroxosodalite dihydrate ($\text{Na}_8[\text{Al}_6\text{Si}_6\text{O}_{24}](\text{OH})_2 \cdot 2\text{H}_2\text{O}$): single-crystal x-ray and powder neutron diffraction and MAS NMR and FT IR spectroscopy, *J. Phys. Chem.* 96(1) (1992) 392-397. Doi:10.1021/j100180a073
- [52] O. Elsenhans, W. Bührer, I. Anderson, J. Nicol, T. Udovic, F. Rieutord, J. Felsche, P. Sieger, G. Engelhardt, Dynamics of OH and H_2O groups in sodalites, *Physica B Condens. Matter* 180-181 (1992) 661-664. Doi:10.1016/0921-4526(92)90427-T
- [53] O.S. Bondareva, Y.A. Malinovskii, *Sov. Phys. Crystallogr.* 28 (1983) 273-276.
- [54] J. Schliesser, K. Lilova, E.M. Pierce, L. Wu, D.M. Missimer, B.F. Woodfield, A. Navrotsky, Low temperature heat capacity and thermodynamic functions of anion bearing sodalites $\text{Na}_8\text{Al}_6\text{Si}_6\text{O}_{24}\text{X}_2$ ($\text{X} = \text{SO}_4, \text{ReO}_4, \text{Cl}, \text{I}$), *J. Chem. Thermodyn.* 114 (2017) 14-24. Doi:10.1016/j.jct.2017.05.035

- [55] M. Mangir Murshed, P. Zhao, A. Huq, T.M. Gelsing, Thermal Expansion Behaviors of $\text{Li}_3\text{AsW}_7\text{O}_{25}$: A Case Study for Comparative Debye Temperature for a Large Polyatomic Unit Cell, *Z. Anorg. Allg. Chem.* 644(4) (2018) 253–259. Doi:10.1002/zaac.201700330
- [56] M.M. Murshed, C.B. Mendive, M. Curti, G. Nénert, P.E. Kalita, K. Lipinska, A.L. Cornelius, A. Huq, T.M. Gelsing, Anisotropic lattice thermal expansion of PbFeBO_4 : A study by X-ray and neutron diffraction, Raman spectroscopy and DFT calculations, *Mater. Res. Bull.* 59 (2014) 170–178. Doi:10.1016/j.materresbull.2014.07.005
- [57] A.K. Wong, R. Jones, J.G. Sparrow, Thermoelastic constant or thermoelastic parameter?, *J. Phys. Chem. Solids* 48(8) (1987) 749-753. Doi:10.1016/0022-3697(87)90071-0
- [58] L. Vočadlo, K.S. Knight, G.D. Price, I.G. Wood, Thermal expansion and crystal structure of FeSi between 4 and 1173 K determined by time-of-flight neutron powder diffraction, *Phys. Chem. Miner.* 29(2) (2002) 132-139. Doi:10.1007/s002690100202
- [59] A.R. Oganov, P.I. Dorogokupets, Intrinsic anharmonicity in equations of state and thermodynamics of solids, *J. Phys.: Condens. Matter* 16(8) (2004) 1351-1360. Doi:10.1088/0953-8984/16/8/018
- [60] A. Senyshyn, D.M. Trots, J.M. Engel, L. Vasylechko, H. Ehrenberg, T. Hansen, M. Berkowski, H. Fuess, Anomalous thermal expansion in rare-earth gallium perovskites: a comprehensive powder diffraction study, *J. Phys.: Condens. Matter* 21(14) (2009) 145405-145419. Doi:10.1088/0953-8984/21/14/145405
- [61] A. Senyshyn, H. Boysen, R. Niewa, J. Banys, M. Kinka, Y. Burak, V. Adamiv, F. Izumi, I. Chumak, H. Fuess, High-temperature properties of lithium tetraborate $\text{Li}_2\text{B}_4\text{O}_7$, *J. Phys. D: Appl. Phys.* 45(17) (2012) 175305-175320. Doi:10.1088/0022-3727/45/17/175305
- [62] T.M. Gelsing, C.B. Mendive, M. Curti, D. Hansmann, G. Nénert, P.E. Kalita, K.E. Lipinska, A. Huq, A.L. Cornelius, M.M. Murshed, Structural properties of mullite-type $\text{Pb}(\text{Al}_{1-x}\text{Mn}_x)\text{BO}_4$, *Z. Kristallogr.* 228(10) (2013) 532-543. Doi:10.1524/zkri.2013.1640
- [63] K. Hoffmann, M.M. Murshed, R.X. Fischer, H. Schneider, T.M. Gelsing, Synthesis and characterization of mullite-type $(\text{Al}_{1-x}\text{Ga}_x)_4\text{B}_2\text{O}_9$, *Z. Kristallogr. - Cryst. Mater.* 229(10) (2014) 699-708. Doi:doi:10.1515/zkri-2014-1785
- [64] K. Hoffmann, T.J.N. Hooper, M.M. Murshed, O. Dolotko, Z. Révay, A. Senyshyn, H. Schneider, J.V. Hanna, T.M. Gelsing, R.X. Fischer, Formation, stability and crystal structure of mullite-type $\text{Al}_{6-x}\text{B}_x\text{O}_9$, *J. Solid State Chem.* 243 (2016) 124-135. Doi:10.1016/j.jssc.2016.08.018
- [65] M.M. Murshed, P. Zhao, M. Fischer, A. Huq, E.V. Alekseev, T.M. Gelsing, Thermal expansion modeling of framework-type $\text{Na}[\text{AsW}_2\text{O}_9]$ and $\text{K}[\text{AsW}_2\text{O}_9]$, *Mater. Res. Bull.* 84 (2016) 273-282. Doi:10.1016/j.materresbull.2016.08.020
- [66] M.M. Murshed, M. Šehović, M. Fischer, A. Senyshyn, H. Schneider, T.M. Gelsing, Thermal behavior of mullite between 4 K and 1320 K, *J. Am. Ceram. Soc.* 100(11) (2017) 5259-5273. Doi:10.1111/jace.15028
- [67] A. Kirsch, M.M. Murshed, M.J. Kirkham, A. Huq, F.J. Litterst, T.M. Gelsing, Temperature-dependent Structural and Spectroscopic Studies of $(\text{Bi}_{1-x}\text{Fe}_x)\text{FeO}_3$, *J. Phys. Chem. C* 122(49) (2018) 28280-28291. Doi:10.1021/acs.jpcc.8b05740

- [68] M.M. Murshed, H. Petersen, M. Fischer, M. Curti, C.B. Mendive, V. Baran, A. Senyshyn, T.M. Gasing, Thermal properties of 2:1 bismuth borate: Temperature-dependent characterizations of lone electron pairs, *J. Am. Ceram. Soc.* 102 (2018) 2154–2164. Doi:10.1111/jace.16042
- [69] W. Depmeier, Tetragonal tetrahedra distortions in cubic sodalite frameworks, *Acta Crystallogr. Sect. B: Struct. Sci.* 40(3) (1984) 185–191. Doi:10.1107/S0108768184001956
- [70] M.T. Dove, *Structure and Dynamics: An Atomic View of Materials*, Oxford University Press, Oxford, 2002.
- [71] M.T. Dove, Theory of displacive phase transitions in minerals, *Am. Mineral.* 82(3-4) (1997) 213–244. Doi:10.2138/am-1997-3-401
- [72] C.H. Rüscher, T.M. Gasing, J.-C. Buhl, Anomalous thermal expansion behaviour of $\text{Na}_8[\text{AlSiO}_4]_6(\text{NO}_3)_2$ -sodalite: $P\bar{4}3n$ to $Pm\bar{3}n$ phase transition by untilting and contraction of TO_4 units, *Z. Kristallogr. - Cryst. Mater.* 218(5) (2003) 332–344. Doi:10.1524/zkri.218.5.332.20731
- [73] J.D. James, J.A. Spittle, S.G.R. Brown, R.W. Evans, A review of measurement techniques for the thermal expansion coefficient of metals and alloys at elevated temperatures, *Meas. Sci. Technol.* 12(3) (2001) R1-R15. Doi:10.1088/0957-0233/12/3/201
- [74] C. Giacovazzo, *Fundamentals of Crystallography*, Oxford University Press, Oxford, 2011.
- [75] R.E. Dinnebier, A. Leineweber, J.S.O. Evans, *Rietveld Refinement: Practical Powder Diffraction Pattern Analysis using TOPAS*, De Gruyter, Berlin, 2018.
- [76] P.F. Peterson, D. Olds, M.T. McDonnell, K. Page, Illustrated formalisms for total scattering data: a guide for new practitioners, *J. Appl. Crystallogr.* 54(1) (2021) 317-332. Doi:10.1107/S1600576720015630
- [77] T. Egami, S.J.L. Billinge, *Underneath the Bragg Peaks - Structural Analysis of Complex Materials*, Pergamon Press, Oxford, UK, 2012.
- [78] I.D. Brown, *The Chemical Bond in Inorganic Chemistry*, 2 ed., Oxford University Press, Oxford, UK, 2016.
- [79] I.D. Brown, Recent Developments in the Methods and Applications of the Bond Valence Model, *Chem. Rev.* 109(12) (2009) 6858-6919. Doi:10.1021/cr900053k
- [80] L. Pauling, THE PRINCIPLES DETERMINING THE STRUCTURE OF COMPLEX IONIC CRYSTALS, *J. Am. Chem. Soc.* 51(4) (1929) 1010-1026. Doi:10.1021/ja01379a006
- [81] C. Preiser, J. Lösel, I.D. Brown, M. Kunz, A. Skowron, Long-range Coulomb forces and localized bonds, *Acta Crystallogr. Sect. B: Struct. Sci.* 55(5) (1999) 698-711. Doi:10.1107/s0108768199003961
- [82] I.D. Brown, Bond valence parameters. <https://www.iucr.org/resources/data/datasets/bond-valence-parameters>. (Accessed 14.09.2022).

- [83] I.D. Brown, D. Altermatt, Bond-valence parameters obtained from a systematic analysis of the Inorganic Crystal Structure Database, *Acta Crystallogr. Sect. B: Struct. Sci.* 41(4) (1985) 244-247. Doi:10.1107/s0108768185002063
- [84] N.E. Brese, M. O'Keeffe, Bond-valence parameters for solids, *Acta Crystallogr. Sect. B: Struct. Sci.* 47(2) (1991) 192-197. Doi:10.1107/s0108768190011041
- [85] M. Wojdyr, Fityk: a general-purpose peak fitting program, *J. Appl. Crystallogr.* 43(5) (2010) 1126-1128. Doi:10.1107/s0021889810030499
- [86] I. Poltz, *Synthese und Struktur-Eigenschaftsbeziehungen gallogermanatischer Sodalithe $[\text{Na}_a\text{X}_b(\text{H}_2\text{O})_n][\text{GaGeO}_4]_6$ und verwandter Verbindungen*, Universität Bremen, Bremen, 2015.
- [87] J. Filik, A.W. Ashton, P.C.Y. Chang, P.A. Chater, S.J. Day, M. Drakopoulos, M.W. Gerring, M.L. Hart, O.V. Magdysyuk, S. Michalik, A. Smith, C.C. Tang, N.J. Terrill, M.T. Wharmby, H. Wilhelm, Processing two-dimensional X-ray diffraction and small-angle scattering data in DAWN 2, *J. Appl. Crystallogr.* 50(3) (2017) 959-966. Doi:10.1107/s1600576717004708
- [88] P. Juhás, T. Davis, C.L. Farrow, S.J.L. Billinge, PDFgetX3: a rapid and highly automatable program for processing powder diffraction data into total scattering pair distribution functions, *J. Appl. Crystallogr.* 46(2) (2013) 560–566. Doi:10.1107/S0021889813005190
- [89] C.L. Farrow, P. Juhas, J.W. Liu, D. Bryndin, E.S. Božin, J. Bloch, T. Proffen, S.J.L. Billinge, PDFfit2 and PDFgui: computer programs for studying nanostructure in crystals, *J. Phys.: Condens. Matter* 19(33) (2007) 335219. Doi:10.1088/0953-8984/19/33/335219
- [90] J. Ahrens, B. Geveci, C. Law, *Paraview: An end-user tool for large data visualization*, The visualization handbook, Elsevier, Oxford, UK, 2005, pp. 717-731.
- [91] J.P. Perdew, K. Burke, M. Ernzerhof, Generalized Gradient Approximation Made Simple, *Phys. Rev. Lett.* 77(18) (1996) 3865-3868. Doi:10.1103/physrevlett.77.3865
- [92] P.E. Blöchl, Projector augmented-wave method, *Phys. Rev. B* 50(24) (1994) 17953-17979. Doi:10.1103/physrevb.50.17953
- [93] J. Enkovaara, C. Rostgaard, J.J. Mortensen, J. Chen, M. Dułak, L. Ferrighi, J. Gavnholt, C. Glinsvad, V. Haikola, H.A. Hansen, H.H. Kristoffersen, M. Kuisma, A.H. Larsen, L. Lehtovaara, M. Ljungberg, O. Lopez-Acevedo, P.G. Moses, J. Ojanen, T. Olsen, V. Petzold, N.A. Romero, J. Stausholm-Møller, M. Strange, G.A. Tritsarlis, M. Vanin, M. Walter, B. Hammer, H. Häkkinen, G.K.H. Madsen, R.M. Nieminen, J.K. Nørskov, M. Puska, T.T. Rantala, J. Schiøtz, K.S. Thygesen, K.W. Jacobsen, Electronic structure calculations with GPAW: a real-space implementation of the projector augmented-wave method, *J. Phys.: Condens. Matter* 22(25) (2010) 253202-25226. Doi:10.1088/0953-8984/22/25/253202
- [94] A. Hjorth Larsen, J. Jørgen Mortensen, J. Blomqvist, I.E. Castelli, R. Christensen, M. Dułak, J. Friis, M.N. Groves, B. Hammer, C. Hargus, E.D. Hermes, P.C. Jennings, P. Bjerre Jensen, J. Kermode, J.R. Kitchin, E. Leonhard Kolsbjerg, J. Kubal, K. Kaasbjerg, S. Lysgaard, J. Bergmann Maronsson, T. Maxson, T. Olsen, L. Pastewka, A. Peterson, C. Rostgaard, J. Schiøtz, O. Schütt, M. Strange, K.S. Thygesen, T. Vegge, L. Vilhelmsen, M. Walter, Z. Zeng, K.W. Jacobsen, The atomic simulation environment—a Python library for working with atoms, *J. Phys.: Condens. Matter* 29(27) (2017) 273002-273032. Doi:10.1088/1361-648x/aa680e

- [95] H.J. Monkhorst, J.D. Pack, Special points for Brillouin-zone integrations, *Phys. Rev. B* 13(12) (1976) 5188-5192. Doi:10.1103/physrevb.13.5188
- [96] G. Kresse, J. Furthmüller, Efficient iterative schemes for *ab initio* total-energy calculations using a plane-wave basis set, *Phys. Rev. B* 54(16) (1996) 11169-11186. Doi:10.1103/physrevb.54.11169
- [97] J.D. Gale, GULP: Capabilities and prospects, *Z. Kristallogr. - Cryst. Mater.* 220(5-6) (2005) 552-554. Doi:10.1524/zkri.220.5.552.65070
- [98] J.D. Gale, A.L. Rohl, The General Utility Lattice Program (GULP), *Mol. Simul.* 29(5) (2003) 291-341. Doi:10.1080/0892702031000104887
- [99] J.D.L. Dutra, T.D. Bispo, S.M. de Freitas, M.V.d.S. Rezende, ParamGULP: An efficient Python code for obtaining interatomic potential parameters for General Utility Lattice Program, *Comput. Phys. Commun.* 265 (2021) 107996. Doi:10.1016/j.cpc.2021.107996
- [100] M. Sierka, A. Joachim Sauer, Structure and reactivity of silica and zeolite catalysts by a combined quantum mechanics—shell-model potential approach based on DFT, *Faraday Discuss.* 106 (1997) 41-62. Doi:10.1039/a701492i
- [101] D.J. Binks, R.W. Grimes, Incorporation of Monovalent Ions in ZnO and Their Influence on Varistor Degradation, *J. Am. Ceram. Soc.* 76(9) (1993) 2370-2372. Doi:10.1111/j.1151-2916.1993.tb07779.x
- [102] R.A. Jackson, R.G. Bell, C.R.A. Catlow, Computer Simulation Studies of Zeolite Structure and Stability, *Stud. Surf. Sci. Catal.* 52 (1989) 203-208. Doi:10.1016/S0167-2991(08)60525-X
- [103] J.A. Creighton, H.W. Deckman, J.M. Newsam, Computer simulation and interpretation of the infrared and Raman spectra of sodalite frameworks, *J. Phys. Chem.* 98(2) (1994) 448-459. Doi:10.1021/j100053a018
- [104] A.M. Mofrad, C. Peixoto, J. Blumeyer, J. Liu, H.K. Hunt, K.D. Hammond, Vibrational Spectroscopy of Sodalite: Theory and Experiments, *J. Phys. Chem. C* 122(43) (2018) 24765-24779. Doi:10.1021/acs.jpcc.8b07633
- [105] K. Lilova, E.M. Pierce, L. Wu, A.M. Jubb, T. Subramani, A. Navrotsky, Energetics of Salt-Bearing Sodalites, $\text{Na}_8\text{Al}_6\text{Si}_6\text{O}_{24}\text{X}_2$ (X = SO_4 , ReO_4 , Cl, I): A Treatment Option for Pertechnetate-Enriched Nuclear Waste Streams, *ACS Earth and Space Chemistry* 4(11) (2020) 2153-2161. Doi:10.1021/acsearthspacechem.0c00244
- [106] J. Ariai, S.R.P. Smith, The Raman spectrum and analysis of phonon modes in sodalite, *Journal of Physics C: Solid State Physics* 14(8) (1981) 1193–1202. Doi:10.1088/0022-3719/14/8/015
- [107] K. Hettmann, T. Wenzel, M. Marks, G. Markl, The sulfur speciation in S-bearing minerals: New constraints by a combination of electron microprobe analysis and DFT calculations with special reference to sodalite-group minerals, *Am. Mineral.* 97(10) (2012) 1653–1661. Doi:10.2138/am.2012.4031

- [108] A.M. Mofrad, P.S. Schellenberg, C. Peixoto, H.K. Hunt, K.D. Hammond, Calculated infrared and Raman signatures of Ag^+ , Cd^{2+} , Pb^{2+} , Hg^{2+} , Ca^{2+} , Mg^{2+} , and K^+ sodalites, *Microporous Mesoporous Mater.* 296 (2020) 109983. Doi:10.1016/j.micromeso.2019.109983
- [109] A.M. Mofrad, K.D. Hammond, A density functional theory study of the vibrational spectra of aluminate sodalite, $[\text{M}_8\text{X}_2][\text{Al}_{12}\text{O}_{24}]\text{-SOD}$ ($\text{M}=\text{Ca}$, Cd , Sr ; $\text{X}=\text{CrO}_4$, MoO_4 , S , SO_4 , Se , SeO_3 , Te , TeO_3), *Microporous Mesoporous Mater.* 309 (2020) 110466. Doi:10.1016/j.micromeso.2020.110466
- [110] N.V. Chukanov, M.F. Viggasina, N.V. Zubkova, I.V. Pekov, C. Schäfer, A.V. Kasatkin, V.O. Yapaskurt, D.Y. Pushcharovsky, Extra-Framework Content in Sodalite-Group Minerals: Complexity and New Aspects of Its Study Using Infrared and Raman Spectroscopy, *Minerals* 10(4) (2020) 363. Doi:10.3390/min10040363
- [111] C.M.B. Henderson, D. Taylor, Infrared spectra of anhydrous members of the sodalite family, *Spectrochim. Acta, Part A* 33(3-4) (1977) 283–290. Doi:10.1016/0584-8539(77)80032-9
- [112] C.M.B. Henderson, D. Taylor, Infrared spectra of aluminogermanate- and aluminate-sodalites and a re-examination of the relationship between T-O bond length, T-O-T angle and the position of the main i.r. absorption band for compounds with framework structures, *Spectrochim. Acta, Part A* 35(8) (1979) 929-935. Doi:10.1016/0584-8539(79)80016-1
- [113] G.M. Johnson, M.T. Weller, Synthesis and characterisation of gallium and germanium containing sodalites, *Stud. Surf. Sci. Catal.* 105 (1997) 269–275. Doi:10.1016/S0167-2991(97)80565-4
- [114] G. Engelhardt, J. Felsche, P. Sieger, The hydrosodalite system $\text{Na}_{6+x}[\text{SiAlO}_4]_6(\text{OH})_x \cdot n\text{H}_2\text{O}$: formation, phase composition, and de- and rehydration studied by ^1H , ^{23}Na , and ^{29}Si MAS-NMR spectroscopy in tandem with thermal analysis, X-ray diffraction, and IR spectroscopy, *J. Am. Chem. Soc.* 114(4) (1992) 1173-1182. Doi:10.1021/ja00030a008
- [115] M. Mangir Murshed, T.M. Gesing, Fast Dynamic Exchange between Na^+OH^- Ion Pairs and H_2O Molecules in Sodalites, *Z. Anorg. Allg. Chem.* 635(13-14) (2009) 2147–2149. Doi:10.1002/zaac.200900061
- [116] S.M. Antao, I. Hassan, THERMAL ANALYSES OF SODALITE, TUGTUPITE, DANALITE AND HELVITE, *Can. Mineral.* 40(1) (2002) 163-172. Doi:10.2113/gscanmin.40.1.163
- [117] D.J. Schipper, T.W. Lathouwers, C.Z. Doorn, Thermal Decomposition of Sodalites, *J. Am. Ceram. Soc.* 56(10) (1973) 523-525. Doi:10.1111/j.1151-2916.1973.tb12402.x
- [118] Z.D. Sharp, G.R. Helffrich, S.R. Bohlen, E.J. Essene, The stability of sodalite in the system $\text{NaAlSiO}_4\text{-NaCl}$, *Geochim. Cosmochim. Acta* 53(8) (1989) 1943-1954. Doi:10.1016/0016-7037(89)90315-3
- [119] R.D. Shannon, C.T. Prewitt, Effective ionic radii in oxides and fluorides, *Acta Crystallogr., Sect. B: Struct. Crystallogr. Cryst. Chem.* 25(5) (1969) 925-946. Doi:10.1107/S0567740869003220

- [120] R.D. Shannon, Revised effective ionic radii and systematic studies of interatomic distances in halides and chalcogenides, *Acta Crystallogr., Sect. A: Found. Adv.* 32(5) (1976) 751–767. Doi:10.1107/S0567739476001551
- [121] P. Fons, A.V. Kolobov, M. Krbal, J. Tominaga, K.S. Andrikopoulos, S.N. Yannopoulos, G.A. Voyiatzis, T. Uruga, Phase transition in crystalline GeTe: Pitfalls of averaging effects, *Phys. Rev. B* 82(15) (2010) 155209. Doi:10.1103/PhysRevB.82.155209
- [122] M.H. Müser, K. Binder, Molecular dynamics study of the α - β transition in quartz: elastic properties, finite size effects, and hysteresis in the local structure, *Phys. Chem. Miner.* 28(10) (2001) 746–755. Doi:10.1007/s002690100203
- [123] F.A. Lindemann, Über die Berechnung molekularer Eigenfrequenzen, *Phys. Z.* 11(14) (1910) 609 - 612.
- [124] L.E. Shelimova, S.K. Plachkova, Estimation of the Debye Temperature of IV-VI Semiconductor Compounds and Rhombohedral $(\text{GeTe})_{1-x}((\text{Ag}_2\text{Te})_{1-y}(\text{Sb}_2\text{Te}_3)_y)_x$ Solid Solutions ($y = 0.6$), *Phys. Status Solidi A* 104(2) (1987) 679-685. Doi:10.1002/pssa.2211040219
- [125] W.H. Baur, R.X. Fischer, The Floppiness of It All: Bond Lengths Change with Atomic Displacement Parameters and the Flexibility of Various Coordination Tetrahedra in Zeolitic Frameworks. An Empirical Structural Study of Bond Lengths and Angles, *Chem. Mater.* 31(7) (2019) 2401–2420. Doi:10.1021/acs.chemmater.8b04919
- [126] M.H. Müser, Average Structure vs. Real Structure: Molecular Dynamics Studies of Silica, in: M.L. Ristig, K.A. Gernoth (Eds.), *Particle Scattering, X-Ray Diffraction, and Microstructure of Solids and Liquids*, Springer Berlin Heidelberg, Berlin, Heidelberg, 2003, pp. 75-100.

List of figures

Figure 1: (a) Tetrahedra (T) six-ring (TSR) of AlO_4^- (yellow) and SiO_4 -tetrahedra (cyan) and tetrahedral coordination of the chloride anion (green) to sodium cations (dark blue). (b) Coordination of the sodium atom to one chloride and three nearer oxygen (red) atoms (Na-O1) of the TSR.....	1
Figure 2: (a) Unit cell of $[\text{Na}_8\text{Cl}_2][\text{AlSiO}_4]_6$ and (b) a T-T atoms linked framework representation of a β -cage. See Figure 1 for the explanation of the colors.....	2
Figure 3: (left) Tilt angles of the SiO_4 and AlO_4 tetrahedra around their respective axes, shown for one tetrahedron each in an otherwise directly T-T linked framework (compare Figure 1 and Figure 2, Na atoms omitted, viewed in direction of the c axis). (right) Selected group-subgroup relationships in sodalites.....	5
Figure 4: Raman spectra of all twelve sodalites, ordered in groups of increasing framework-volume and increasing halide-ion size (black: Cl^- , blue: Br^- , green: I^-) from top to bottom. Intensity normalized to the maximum peak.....	16
Figure 5: Positions and FWHMs of selected Raman peaks which can be identified for every investigated sodalite. All peaks are labeled in Figure 4 or marked by an arrow in Figure 6. The different sodalites are numbered from 1 to 12 in order of increasing halide ion size and framework volume (compare labels in Figure 4).....	17
Figure 6: Raman spectra in the region between 25 cm^{-1} and 320 cm^{-1} , ordered in groups of increasing halide-ion size and increasing framework-volume (black: Al-Si, blue: Ga-Si, green: Al-Ge, red: Ga-Ge) from top to bottom. Intensity normalized to the maximum peak (δ Si-O-Al in Figure 4).	18
Figure 7: IR spectra of the investigated sodalites, ordered according to increasing volume of framework and incorporated halogenide-ion from top to bottom.....	20
Figure 8: TGA (black) and DSC curves (red) as well as their first derivatives (blue: TGA, orange: DSC) for all twelve sodalites (composition given in each panel).	22
Figure 9: Temperature-dependent framework cation – framework oxygen distances (error bars are not plotted for clarity). The different frameworks are indicated by color and the incorporated halogenide ion by type of symbol.	24
Figure 10: Temperature-dependent tilt angle (left) and Na–X distance (right) from PXRD refinements.	25
Figure 11: Fittings (red line) of the experimentally obtained order parameter z' (black circles) close to the temperature of phase transition using the Landau theory. The values of z' after the determined critical temperature were set to 0.	26
Figure 12: Temperature-dependent shorter Na–O1 (left) and longer Na–O2 distances (right). The different frameworks are indicated by color and the incorporated halide ion by type of symbol.	27

Figure 13: Bond valence sums of the halide ion X (left) and Na (right) against the decomposition temperature of the respective compound. The respective structures were obtained from X-ray diffraction experiments. Linear fits are included as guides to the eye.	27
Figure 14: Cell volume (main panels) and TEC $\alpha_{I,vol}$ (insets) of all twelve sodalites with their DEA-models (red lines). The enlarged difference curve of the volume model (red line within green borders) ends 50 K after the last data point which was used to fit against.	30
Figure 15: Lattice energy of the sodalites against the volume of their unit cells. Linear fits are given as guides to the eye.....	32
Figure 16: Phonon density of states (PDOS) of the alumosilicate (top left), gallosilicate (top right), alumogermanate (bottom left) and gallogermanate (bottom right) sodalites. The colors are according to the template ion chloride (black), bromide (blue) or iodide (green).	33
Figure 17: Plot of Y vs $\theta_{average}$. The linear equations for the three groups are given by the lines. AlGeCl is included in group 2.	35
Figure 18: PDFs of all sodalites at ambient conditions as measured (black) and calculated (red) together with the difference curve (green).	37
Figure 19: BVSs from structures determined by PDF-Rietveld refinement of the halide ion X (left) and Na (right) against the decomposition temperature of the respective compound. The respective structures were obtained from X-ray diffraction experiments. Linear fits are included as guides to the eye.	38
Figure 20: Displacement parameters of Na and O obtained from PDF calculations in the different sodalites as ellipsoids (99 % probability), ordered following framework (vertical) and template (horizontal). The atoms are colored according to their types: aluminum (light blue), silicon (blue), gallium (grey), germanium (light green), oxygen (red), sodium (yellow), chloride (green), bromide (brown), iodide (purple).	39
Figure 21: Equivalent displacement parameters of sodium and the respective halide ion in the sodalite structures from the atomic positions obtained in MD calculations.	40
Figure 22: The structures of the gallogermanate sodalites at ambient temperature refined with a split Na position where possible. GaGeCl (a), GaGeBr (b) and GaGeI sodalite (c) (Na displayed in different shades of yellow/orange for clarity).....	42
Figure 23: 3-dimensional BVS as seen from above the plane of the three O1 oxygen atoms. The central atom is the respective halide anion X. Only voxels with a BVS between 0.9 and 1.1 v.u. are shown.....	43
Figure 24: 3-dimensional BVS viewed orthogonal to the plane of the three O1 oxygen atoms. Only voxels with a BVS between 0.9 and 1.1 v.u. are shown.....	44

Figure 25: The Na position in the three gallogermanate sodalites. Colored symbols show the Na refined against the PDF using a split-position model (top row: *P43n-2x8e*, bottom row: *P43n-24i*), black symbols show the results of in-house PXRD experiments (*P43n-avg.*)..... 46

List of tables

Table 1: Experimental parameters of the hydrothermal syntheses. ($T^1 = \text{Al}$ or Ga , $T^2 = \text{Si}$ or Ge , $X = \text{Cl}$, Br or I).....	10
Table 2: Estimated decomposition onset T_D , water loss from cages (in % of total mass) and calculated average water molecules per cage (mpc).	23
Table 3: Selected bond lengths at ambient conditions and calculated bond valence sums.....	28
Table 4: Temperature ranges of volume and TEC used for DEA-fitting.....	29
Table 5: Parameters obtained in DEA-fittings.	31
Table 6: Results from the force-field calculations with GULP for each compound.....	31
Table 7: The sodalites in increasing order of K_L . The AlGeCl sodalite could either be attributed to group 1 or 2, the first K_L average value for group 1 and group 2 is given with AlGeCl included in group 1, the second one with AlGeCl in group 2.	34
Table 8: Lattice parameter (LP), selected bond lengths and BVS from PDF-Rietveld refinements.	36
Table 9: Equivalent displacement parameters of sodium determined in PDF calculations and from the atomic positions obtained in AIMD calculations.	41

Appendix

Sodalite structures at ambient conditions

Experimental data, refined atomic parameters and Rietveld plots of the sodalites at ambient conditions (GaGeCl and GaGeBr) or 300 K (all other compounds) are presented in the following.

Occupancies (Occ.) in the structures were refined when resulting in overall lower errors and especially more meaningful values of B ($B(T^1) \approx B(T^2)$, positive values etc.) and T–O bond-lengths. They were refined with the following constraints if applicable:

$$\text{Occ.}(T^1) + \text{Occ.}(T^2) = 2$$

$$\text{Occ.}(\text{Na}) = 0.75 + \text{Occ.}(X)/4$$

Constrained values are marked by a * symbol.



Table A 1: Experimental X-ray powder data for $[\text{Na}_8\text{Cl}_2][\text{AlSiO}_4]_6$, based on the PXRD measurement with the HTK1200N at the Phillips X'Pert.

Space Group	$P\bar{4}3n$ (No. 218)
a /pm	888.377(8)
$V/10^6$ pm³	701.119(19)
Formula units in cell	$Z = 1$
Calculated density /g cm⁻³	2.29550(6)
Wavelength CuKα1 /pm	154.0596
Wavelength CuKα1 /pm	154.4493
$\theta/2\theta$ scan	$10 < 2\theta < 130$
No. of data points	7182
Weighted residual (profile) R_{WP} /%	9.974
Residual (profile) R_P /%	7.546
Residual (intensity) R_B /%	2.109

Table A 2: Atomic parameters of $[\text{Na}_8\text{Cl}_2][\text{AlSiO}_4]_6$ sodalite.

Atom	Wyck. Pos.	x	y	z	Occ.	B /10 ⁻⁴ pm ²
Cl	2a	0	0	0	1	1.994(57)
Al	6d	1/4	0	1/2	1	0.43(11)
Si	6c	1/2	1/4	0	1	0.59(11)
Na	8e	0.17705(16)	0.17705(16)	0.17705(16)	1	1.323(48)
O	24i	0.13839 (22)	0.15029(22)	0.43779(20)	1	0.614(52)

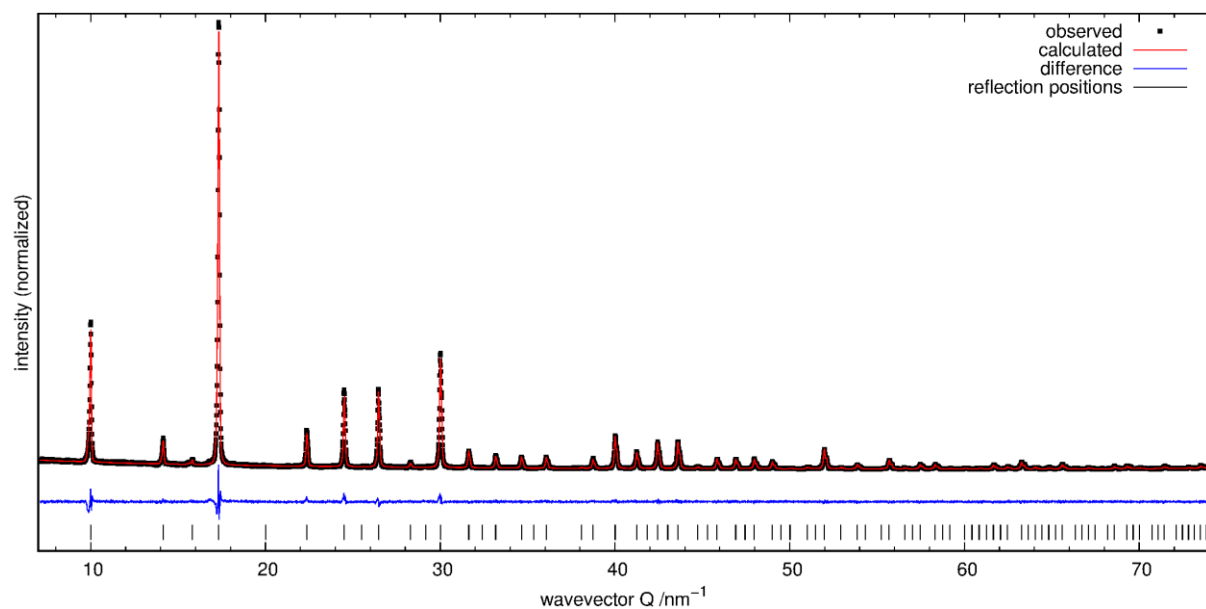


Figure A 1: Rietveld plot of AlSiCl sodalite at 300 K showing the observed data (black), calculated intensities (red), difference curve (blue) and reflection positions in $P\bar{4}3n$ (black ticks).

$[\text{Na}_8\text{Br}_2][\text{AlSiO}_4]_6$

Table A 3: Experimental X-ray powder data for $[\text{Na}_8\text{Br}_2][\text{AlSiO}_4]_6$, based on the PXRD measurement with the HTK1200N at the Phillips X'Pert.

Space Group	$P\bar{4}3n$ (No. 218)
a /pm	894.030(7)
$V/10^6$ pm³	714.589(17)
Formula units in cell	$Z = 1$
Calculated density /g cm⁻³	2.45881(6)
Wavelength CuKα1 /pm	154.0596
Wavelength CuKα1 /pm	154.4493
$\theta/2\theta$ scan	$10 < 2\theta < 130$
No. of data points	7182
Weighted residual (profile) R_{WP} /%	7.265
Residual (profile) R_P /%	5.633
Residual (intensity) R_B /%	1.233

Table A 4: Atomic parameters of $\text{Na}_8\text{Br}_2[\text{AlSiO}_4]_6$ sodalite.

Atom	Wyck. Pos.	x	y	z	Occ.	B /10 ⁻⁴ pm ²
Br	2a	0	0	0	1	2.718(46)
Al	6d	1/4	0	1/2	1	0.51(19)
Si	6c	1/2	1/4	0	1	0.50(17)
Na	8e	0.18640(17)	0.18640(17)	0.18640(17)	1	1.405(67)
O	24i	0.13970(28)	0.15137(29)	0.44245(23)	1	0.528(61)

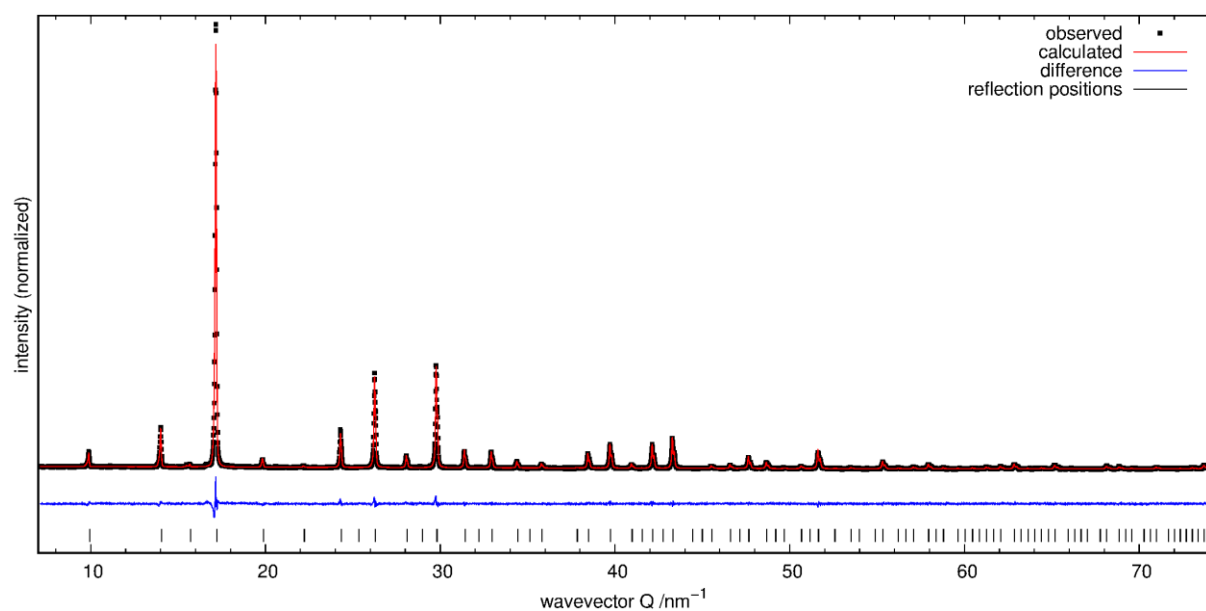


Figure A 2: Rietveld plot of AlSiBr sodalite at 300 K showing the observed data (black), calculated intensities (red), difference curve (blue) and reflection positions in $P\bar{4}3n$ (black ticks).



Table A 5: Experimental X-ray powder data for $[\text{Na}_8\text{I}_2][\text{AlSiO}_4]_6$, based on the PXRD measurement with the HTK1200N at the Phillips X'Pert.

Space Group	$P\bar{4}3n$ (No. 218)
a /pm	902.228(12)
V 10^6 pm³	734.43(3)
Formula units in cell	$Z = 1$
Calculated density /g cm⁻³	2.604(1)
Wavelength CuKα1 /pm	154.0596
Wavelength CuKα1 /pm	154.4493
$\theta/2\theta$ scan	$10 < 2\theta < 130$
No. of data points	7182
Weighted residual (profile) R_{WP} /%	7.518
Residual (profile) R_P /%	5.932
Residual (intensity) R_B /%	1.246

Table A 6: Atomic parameters of $[\text{Na}_8\text{I}_2][\text{AlSiO}_4]_6$ sodalite.

Atom	Wyck. Pos.	x	y	z	Occ.	B / 10^{-4} pm ²
I	2a	0	0	0	1	2.439(66)
Al	6d	$\frac{1}{4}$	0	$\frac{1}{2}$	1	0.000(57)*
Si	6c	$\frac{1}{2}$	$\frac{1}{4}$	0	1	0.000(57)*
Na	8e	0.19922(26)	0.19922(26)	0.19922(26)	1	1.05(12)
O	24i	0.14243(92)	0.14987(91)	0.45194(41)	1	0.138(99)

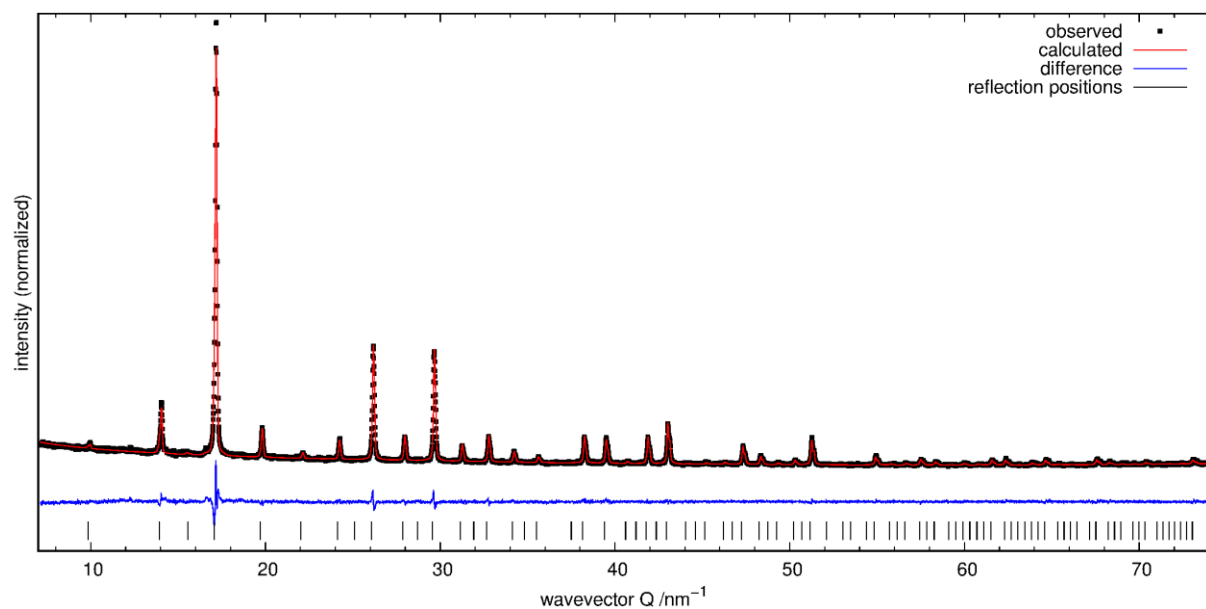


Figure A 3: Rietveld plot of AlSiI sodalite at 300 K showing the observed data (black), calculated intensities (red), difference curve (blue) and reflection positions in $P\bar{4}3n$ (black ticks).

$[\text{Na}_8\text{Cl}_2][\text{GaSiO}_4]_6$

Table A 7: Experimental X-ray powder data for $[\text{Na}_8\text{Cl}_2][\text{GaSiO}_4]_6$, based on the PXRD measurement with the HTK1200N at the Phillips X'Pert.

Space Group	$P\bar{4}3n$ (No. 218)
a /pm	894.701(4)
$V/10^6$ pm³	716.199(9)
Formula units in cell	$Z = 1$
Calculated density /g cm⁻³	2.81(3)
Wavelength CuKα1 /pm	154.0596
Wavelength CuKα1 /pm	154.4493
$\theta/2\theta$ scan	$10 < 2\theta < 130$
No. of data points	7182
Weighted residual (profile) R_{WP} /%	9.475
Residual (profile) R_P /%	7.245
Residual (intensity) R_B /%	1.442

Table A 8: Atomic parameters of $[\text{Na}_8\text{Cl}_2][\text{GaSiO}_4]_6$ sodalite.

Atom	Wyck. Pos.	x	y	z	Occ.	B /10 ⁻⁴ pm ²
Cl	2a	0	0	0	1	1.894(70)
Ga	6d	1/4	0	1/2	0.9467(23)*	0.326(28)
Si	6c	1/2	1/4	0	1.0533(23)*	0.513(48)
Na	8e	0.17258 (23)	0.17258 (23)	0.17258 (23)	1	1.548(72)
O	24i	0.13457 (27)	0.15125 (30)	0.43010 (30)	1	1.894(71)

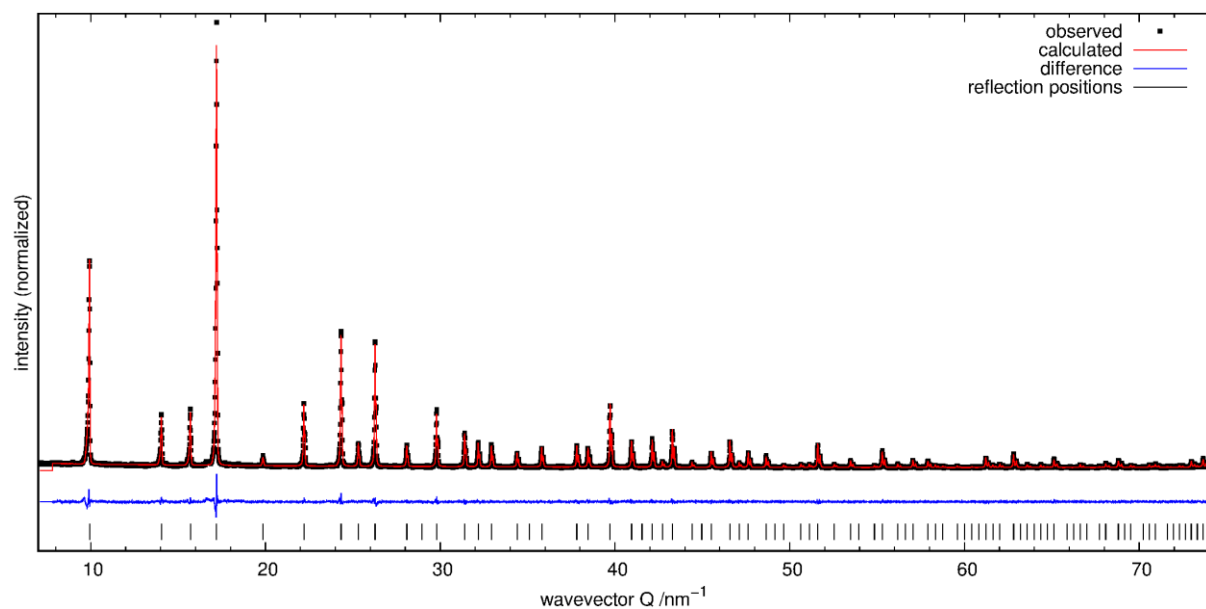


Figure A 4: Rietveld plot of GaSiCl sodalite at 300 K showing the observed data (black), calculated intensities (red), difference curve (blue) and reflection positions in $P\bar{4}3n$ (black ticks).

$[\text{Na}_8\text{Br}_2][\text{GaSiO}_4]_6$

Table A 9: Experimental X-ray powder data for $[\text{Na}_8\text{Br}_2][\text{GaSiO}_4]_6$, based on the PXRD measurement with the HTK1200N at the Phillips X'Pert.

Space Group	$P\bar{4}3n$ (No. 218)
a /pm	900.854(5)
$V/10^6$ pm³	731.076(11)
Formula units in cell	$Z = 1$
Calculated density /g cm⁻³	2.97108(5)
Wavelength CuKα1 /pm	154.0596
Wavelength CuKα1 /pm	154.4493
$\theta/2\theta$ scan	$10 < 2\theta < 130$
No. of data points	7182
Weighted residual (profile) R_{WP} /%	8.929
Residual (profile) R_P /%	6.867
Residual (intensity) R_B /%	1.081

Table A 10: Atomic parameters of $[\text{Na}_8\text{Br}_2][\text{GaSiO}_4]_6$ sodalite.

Atom	Wyck. Pos.	x	y	z	Occ.	B /10 ⁻⁴ pm ²
Br	2a	0	0	0	1	2.554(45)
Ga	6d	1/4	0	1/2	0.974*	0.690(27)
Si	6c	1/2	1/4	0	1.026*	0.756(47)
Na	8e	0.18189(24)	0.18189(24)	0.18189(24)	1	1.676(86)
O	24i	0.13483(25)	0.15240(27)	0.43430(32)	1	0.890(85)

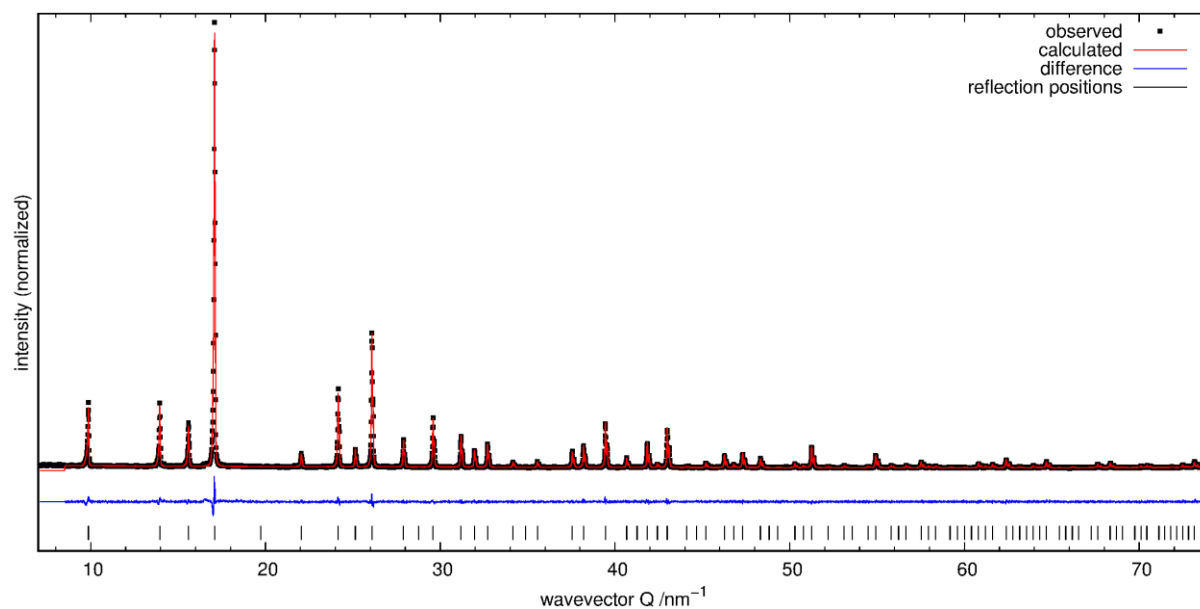


Figure A 5: Rietveld plot of GaSiBr sodalite at 300 K showing the observed data (black), calculated intensities (red), difference curve (blue) and reflection positions in $P\bar{4}3n$ (black ticks).



Table A 11: Experimental X-ray powder data for $[\text{Na}_8\text{I}_2][\text{GaSiO}_4]_6$, based on the PXRD measurement with the HTK1200N at the Phillips X'Pert.

Space Group	$P\bar{4}3n$ (No. 218)
a /pm	908.455(5)
$V/10^6$ pm³	749.739(11)
Formula units in cell	$Z = 1$
Calculated density /g cm⁻³	3.072(6)
Wavelength CuKα1 /pm	154.0596
Wavelength CuKα1 /pm	154.4493
$\theta/2\theta$ scan	$10 < 2\theta < 130$
No. of data points	7182
Weighted residual (profile) R_{WP} /%	11.087
Residual (profile) R_P /%	8.495
Residual (intensity) R_B /%	1.823

Table A 12: Atomic parameters of $[\text{Na}_8\text{I}_2][\text{GaSiO}_4]_6$ sodalite.

Atom	Wyck. Pos.	x	y	z	Occ.	B /10 ⁻⁴ pm ²
I	2a	0	0	0	0.9615(52)*	2.843(64)
Ga	6d	¼	0	½	0.9604(50)*	0.481(53)
Si	6c	½	¼	0	1.0396(50)*	0.759(99)
Na	8e	0.19376(36)	0.19376(36)	0.19376(36)	0.9904(14)*	1.69(14)
O	24i	0.13752(45)	0.15395(49)	0.43655(47)	1	0.58(13)

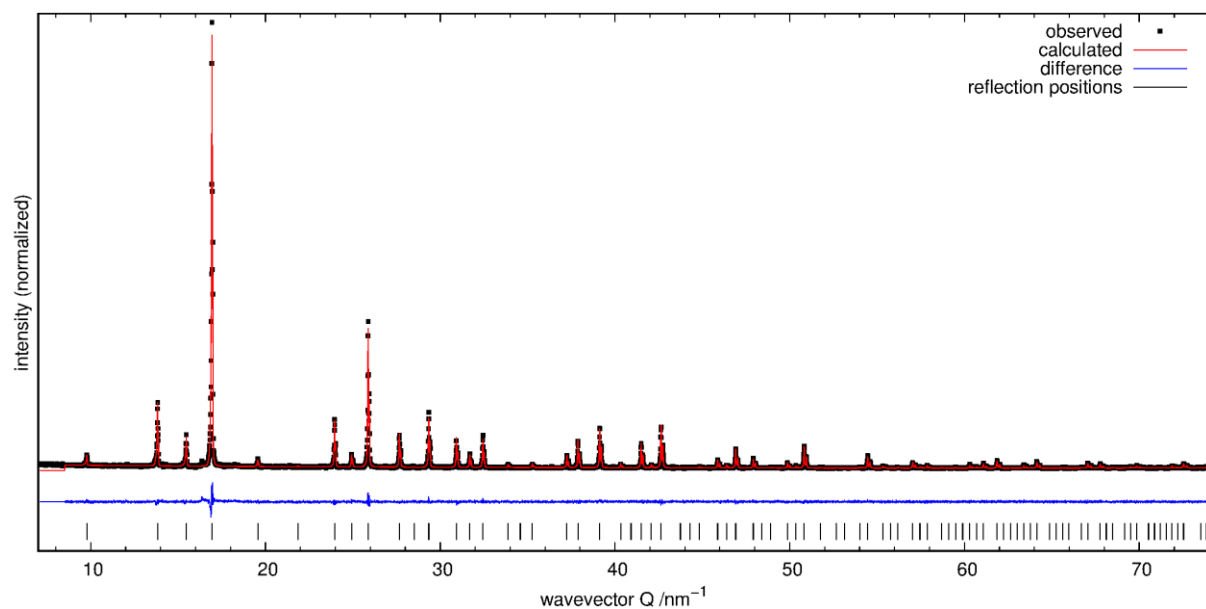


Figure A 6: Rietveld plot of GaSiI sodalite at 300 K showing the observed data (black), calculated intensities (red), difference curve (blue) and reflection positions in $P\bar{4}3n$ (black ticks).

[Na₈Cl₂][AlGeO₄]₆

Table A 13: Experimental X-ray powder data for [Na₈Cl₂][AlGeO₄]₆, based on the PXRD measurement with the HTK1200N at the Phillips X'Pert.

Space Group	<i>P</i>$\bar{4}$3<i>n</i> (No. 218)
<i>a</i> /pm	903.779(5)
<i>V</i> /10⁶ pm³	738.221(13)
Formula units in cell	<i>Z</i> = 1
Calculated density /g cm⁻³	2.773(2)
Wavelength CuKα1 /pm	154.0596
Wavelength CuKα1 /pm	154.4493
θ /2θ scan	10 < 2θ < 130
No. of data points	7182
Weighted residual (profile) <i>R</i>_{WP} /%	8.798
Residual (profile) <i>R</i>_P /%	6.788
Residual (intensity) <i>R</i>_B /%	0.967

Table A 14: Atomic parameters of [Na₈Cl₂][AlGeO₄]₆ sodalite.

Atom	Wyck. Pos.	x	y	z	Occ.	B /10 ⁻⁴ pm ²
Cl	2a	0	0	0	1	1.936(82)
Al	6d	¼	0	½	1.0133(30)*	0.547(59)
Ge	6c	½	¼	0	0.9867(30)*	0.589(30)
Na	8e	0.17292(24)	0.17292(24)	0.17292(24)	1	1.272(78)
O	24i	0.14305(32)	0.14356(30)	0.42744(31)	1	0.558(82)

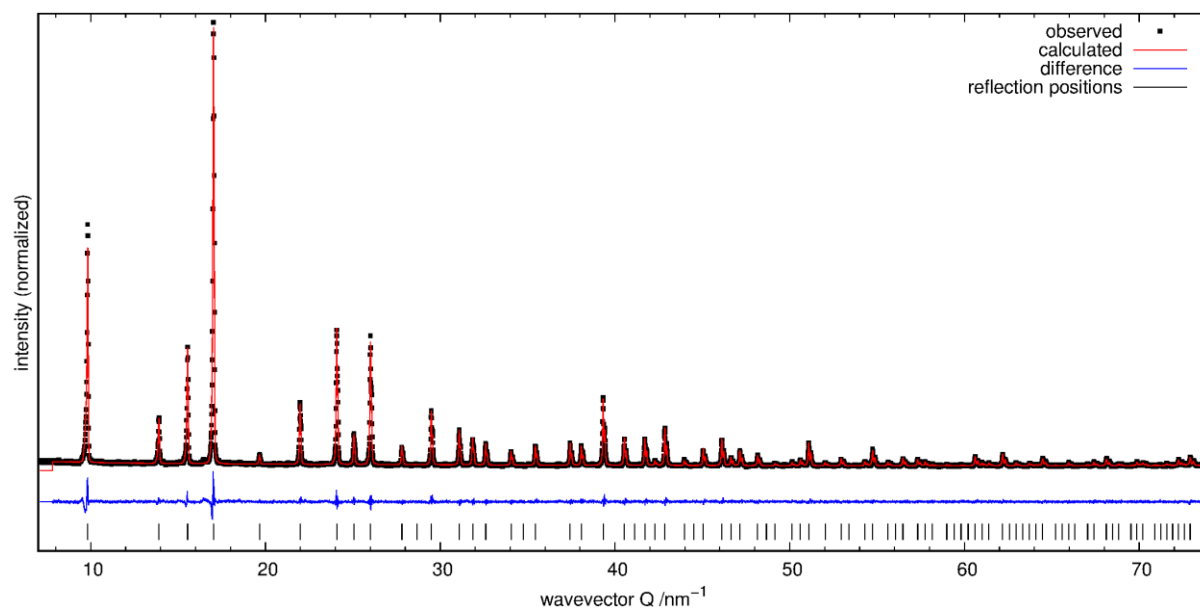


Figure A 7: Rietveld plot of AlGeCl sodalite at 300 K showing the observed data (black), calculated intensities (red), difference curve (blue) and reflection positions in *P* $\bar{4}$ 3*n* (black ticks).

$[\text{Na}_8\text{Br}_2][\text{AlGeO}_4]_6$

Table A 15: Experimental X-ray powder data for $[\text{Na}_8\text{Br}_2][\text{AlGeO}_4]_6$, based on the PXRD measurement with the HTK1200N at the Phillips X'Pert.

Space Group	$P\bar{4}3n$ (No. 218)
a /pm	909.511(8)
$V/10^6$ pm³	752.356(19)
Formula units in cell	$Z = 1$
Calculated density /g cm⁻³	2.897(2)
Wavelength CuKα1 /pm	154.0596
Wavelength CuKα1 /pm	154.4493
$\theta/2\theta$ scan	$10 < 2\theta < 130$
No. of data points	7182
Weighted residual (profile) R_{WP} /%	8.086
Residual (profile) R_P /%	6.337
Residual (intensity) R_B /%	2.221

Table A 16: Atomic parameters of $[\text{Na}_8\text{Br}_2][\text{AlGeO}_4]_6$ sodalite.

Atom	Wyck. Pos.	x	y	z	Occ.	B /10 ⁻⁴ pm ²
Br	2a	0	0	0	0.9225(36)*	1.637(58)
Al	6d	¼	0	½	1.0278(36)*	0.736(77)
Ge	6c	½	¼	0	0.9723(36)*	0.697(39)
Na	8e	0.18135(29)	0.18135(29)	0.18135(29)	0.98062(90)*	0.98062(90)
O	24i	0.14500(35)	0.14532(32)	0.42965(32)	1	0.718(89)

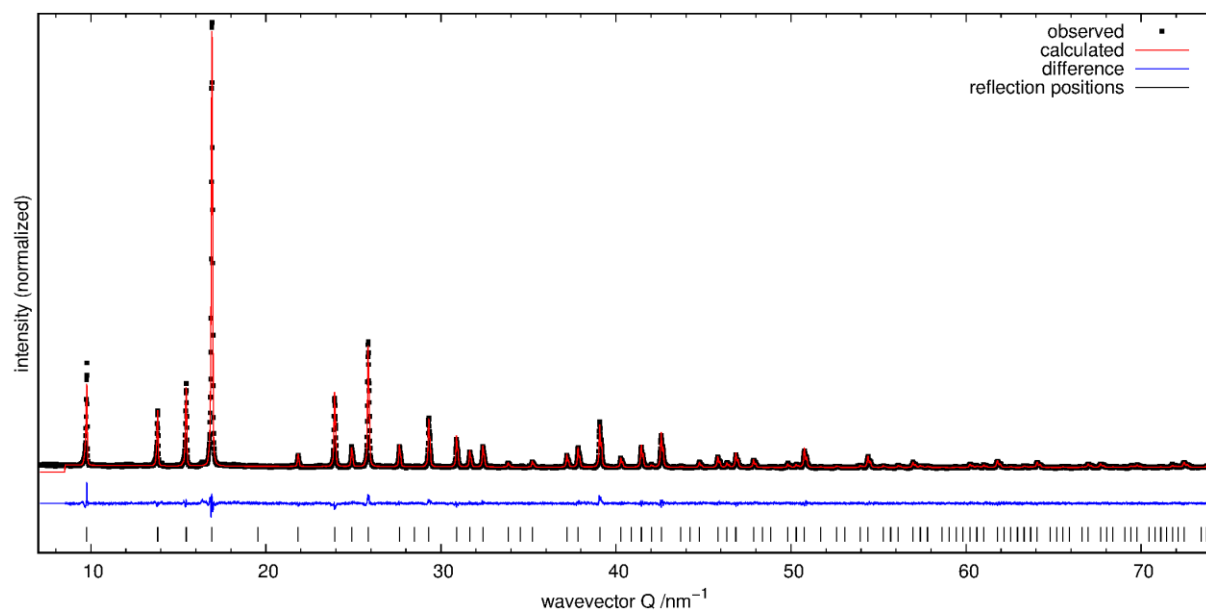


Figure A 8: Rietveld plot of AlGeBr sodalite at 300 K showing the observed data (black), calculated intensities (red), difference curve (blue) and reflection positions in $P\bar{4}3n$ (black ticks).

[Na₈I₂][AlGeO₄]₆

Table A 17: Experimental X-ray powder data for [Na₈I₂][AlGeO₄]₆, based on the PXRD measurement with the HTK1200N at the Phillips X'Pert.

Space Group	<i>P</i>$\bar{4}$<i>3n</i> (No. 218)
<i>a</i> /pm	917.328(14)
<i>V</i> /10⁶ pm³	771.92(4)
Formula units in cell	<i>Z</i> = 1
Calculated density /g cm⁻³	3.016(6)
Wavelength CuKα1 /pm	154.0596
Wavelength CuKα1 /pm	154.4493
θ /2θ scan	10 < 2 θ < 130
No. of data points	7182
Weighted residual (profile) <i>R</i>_{WP} /%	10.776
Residual (profile) <i>R</i>_P /%	8.367
Residual (intensity) <i>R</i>_B /%	1.346

Table A 18: Atomic parameters of [Na₈I₂][AlGeO₄]₆ sodalite.

Atom	Wyck. Pos.	x	y	z	Occ.	B /10 ⁻⁴ pm ²
I	2a	0	0	0	0.9897(83)*	2.94(10)
Al	6d	¼	0	½	1.0405(69)*	0.37(15)
Ge	6c	½	¼	0	0.9595(69)*	0.401(80)
Na	8e	0.19468(46)	0.19468(46)	0.19468(46)	0.9974(21)*	1.56(21)
O	24i	0.14521(69)	0.14578(60)	0.44142(64)	1	0.29(15)

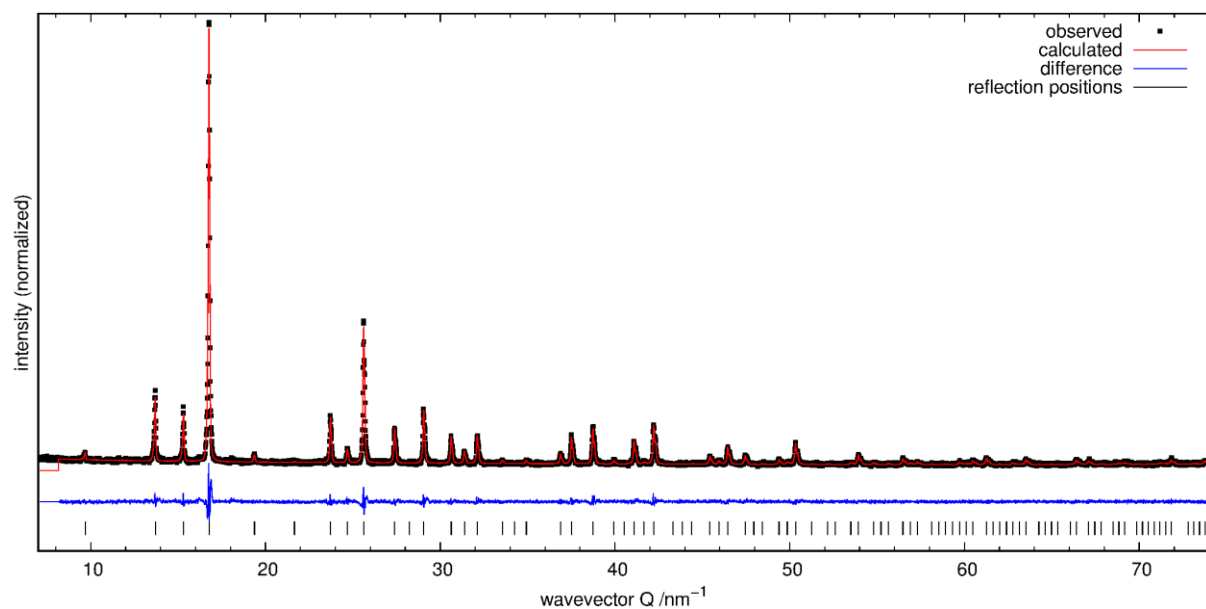


Figure A 9: Rietveld plot of AGeI sodalite at 300 K showing the observed data (black), calculated intensities (red), difference curve (blue) and reflection positions in *P* $\bar{4}$ *3n* (black ticks).



Table A 19: Experimental X-ray powder data for $[\text{Na}_8\text{Cl}_2][\text{GaGeO}_4]_6$, based on the PXRD measurement at the StadiMP in Debye-Scherrer geometry.

Space Group	$P\bar{4}3n$ (No. 218)
a /pm	911.788(8)
$V/10^6$ pm³	758.02(2)
Formula units in cell	$Z = 1$
Calculated density /g cm⁻³	3.27057(9)
Wavelength MoKα1 /pm	70.93
$\theta/2\theta$ scan	$5 < 2\theta < 75$
No. of data points	4668
Weighted residual (profile) R_{WP} /%	5.266
Residual (profile) R_P /%	4.133
Residual (intensity) R_B /%	1.025

Table A 20: Atomic parameters of $[\text{Na}_8\text{Cl}_2][\text{GaGeO}_4]_6$ sodalite.

Atom	Wyck. Pos.	x	y	z	Occ.	B /10 ⁻⁴ pm ²
Cl	2a	0	0	0	1	1.78(11)
Ga	6d	1/4	0	1/2	1	0.34(29)
Ge	6c	1/2	1/4	0	1	0.46 (29)
Na	8e	0.17044(40)	0.17044(40)	0.17044(40)	1	1.04(11)
O	24i	0.1366(17)	0.1451(17)	0.42099(50)	1	0.38 (14)

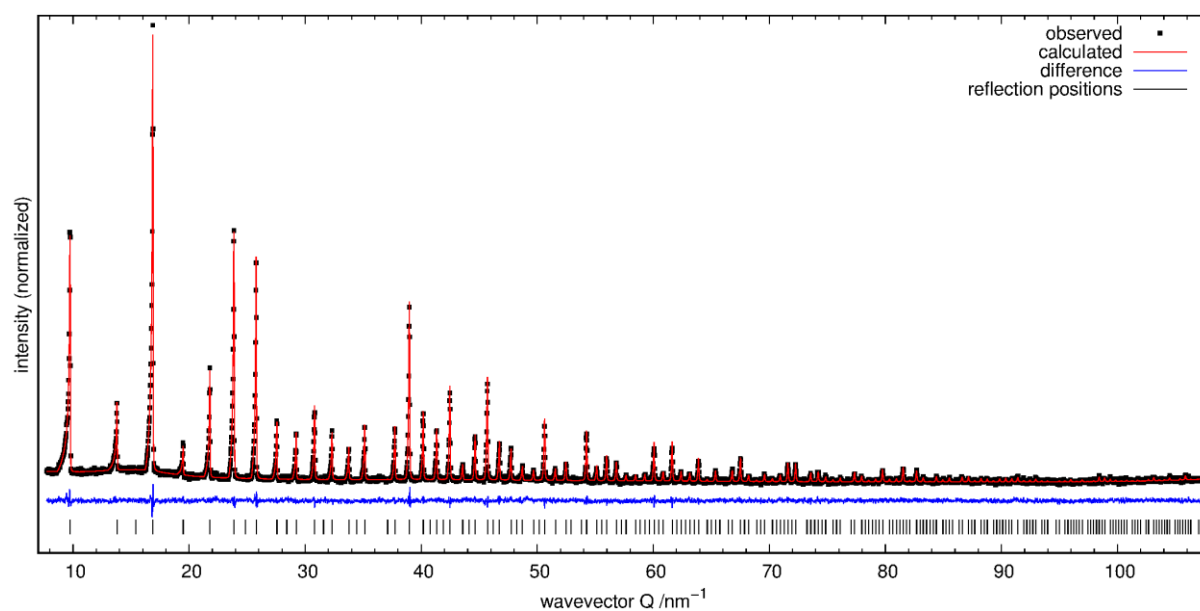


Figure A 10: Rietveld plot of GaGeCl sodalite at ambient temperature showing the observed data (black), calculated intensities (red), difference curve (blue) and reflection positions in $P\bar{4}3n$ (black ticks).

$[\text{Na}_8\text{Br}_2][\text{GaGeO}_4]_6$

Table A 21: Experimental X-ray powder data for $[\text{Na}_8\text{Br}_2][\text{GaGeO}_4]_6$, based on the PXRD measurement at the StadiMP in Debye-Scherrer geometry.

Space Group	$P\bar{4}3n$ (No. 218)
a /pm	917.865(6)
$V/10^6$ pm³	773.279(14)
Formula units in cell	$Z = 1$
Calculated density /g cm⁻³	3.386(12)
Wavelength MoKα1 /pm	70.93
$\theta/2\theta$ scan	$4 < 2\theta < 80$
No. of data points	5068
Weighted residual (profile) R_{WP} /%	2.983
Residual (profile) R_P /%	2.299
Residual (intensity) R_B /%	0.650

Table A 22: Atomic parameters of $[\text{Na}_8\text{Br}_2][\text{GaGeO}_4]_6$ sodalite.

Atom	Wyck. Pos.	x	y	z	Occ.	B /10 ⁻⁴ pm ²
Br	2a	0	0	0	0.9722(36)*	1.791(45)
Ga	6d	1/4	0	1/2	0.983(13)*	0.25(19)
Ge	6c	1/2	1/4	0	1.017(20)*	0.44(19)
Na	8e	0.17744(30)	0.17744(30)	0.17744(30)	0.9931(9)*	1.156(90)
O	24i	0.1381(17)	0.1474(17)	0.42197(35)	1	0.25(12)

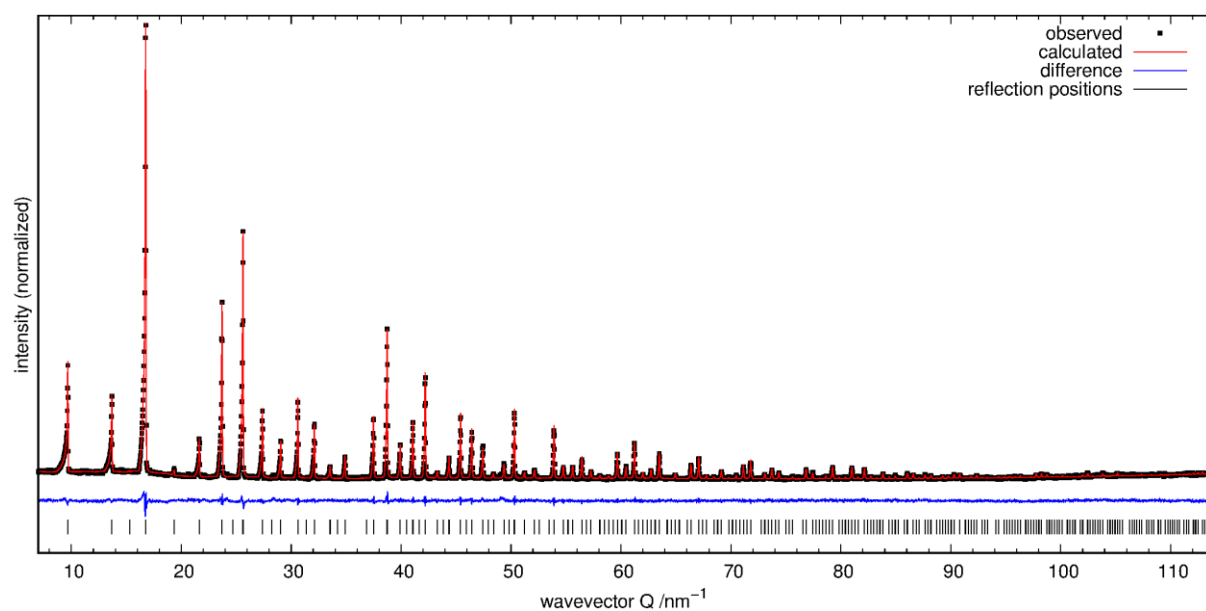


Figure A 11: Rietveld plot of GaGeBr sodalite at ambient temperature showing the observed data (black), calculated intensities (red), difference curve (blue) and reflection positions in $P\bar{4}3n$ (black ticks).

[Na₈I₂][GaGeO₄]₆

Table A 23: Experimental X-ray powder data for [Na₈I₂][GaGeO₄]₆, based on the PXRD measurement with the HTK1200N at the Phillips X'Pert.

Space Group	<i>P</i>$\bar{4}$3<i>n</i> (No. 218)
<i>a</i> /pm	925.757(5)
<i>V</i> /10⁶ pm³	793.397(14)
Formula units in cell	<i>Z</i> = 1
Calculated density /g cm⁻³	3.508(12)
Wavelength CuKα1 /pm	154.0596
Wavelength CuKα1 /pm	154.4493
θ /2θ scan	10 < 2 θ < 130
No. of data points	7182
Weighted residual (profile) <i>R</i>_{WP} /%	7.374
Residual (profile) <i>R</i>_P /%	5.746
Residual (intensity) <i>R</i>_B /%	3.158

Table A 24: Atomic parameters of [Na₈I₂][GaGeO₄]₆ sodalite.

Atom	Wyck. Pos.	x	y	z	Occ.	B /10 ⁻⁴ pm ²
I	2a	0	0	0	1	2.783(43)
Ga	6d	¼	0	½	0.968(14)*	0.84(19)
Ge	6c	½	¼	0	1.032(14)*	0.88(18)
Na	8e	0.18946(29)	0.18946(29)	0.18946(29)	1	1.25(12)
O	24i	0.1442(17)	0.1455(17)	0.42606(38)	1	0.025(92)

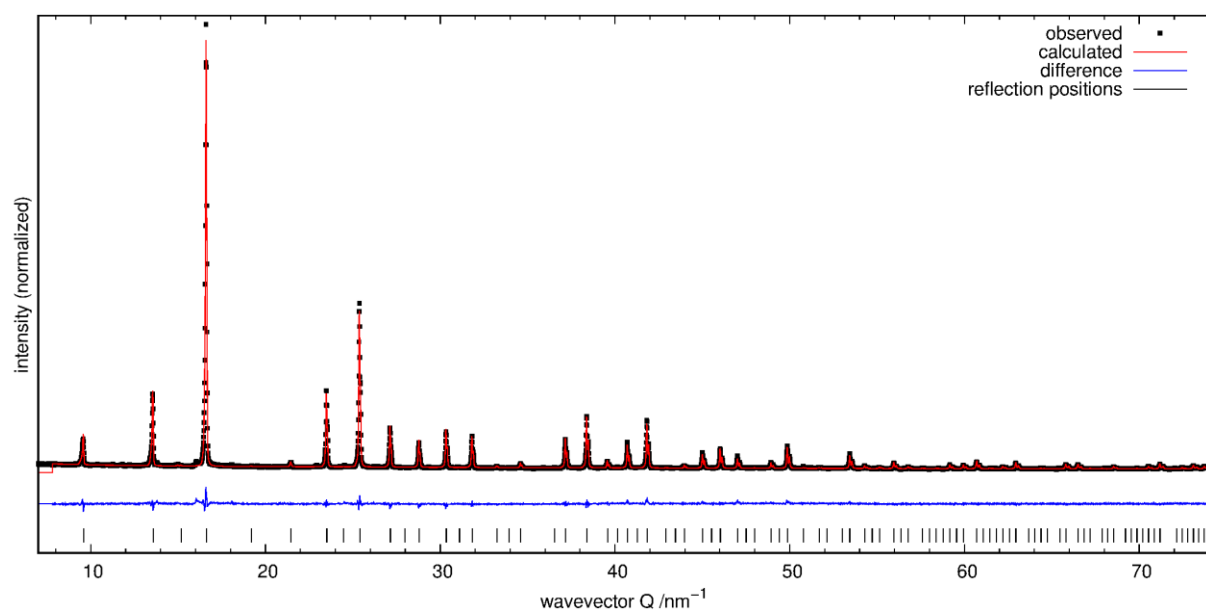


Figure A 12: Rietveld plot of GaGeI sodalite at 300 K showing the observed data (black), calculated intensities (red), difference curve (blue) and reflection positions in *P* $\bar{4}$ 3*n* (black ticks).